A Biomimetic Model Membrane System on Oxidic Surfaces Designed for the Investigation of *Cytochrome c Oxidase* and other Membrane Proteins by Fluorescence and Waveguide Spectroscopy

Dissertation

zur Erlangung des Grades

Doktor der Naturwissenschaften

im
Fachbereich Chemie, Pharmazie und Geowissenschaften
der Johannes-Gutenberg Universität Mainz

vorgelegt von
Asmorom Afewerki Kibrom
geboren in Asmara/Eritrea

Mainz, Juli 2010

Dekan: Prof. Dr. D.Sc. h.c. Wolfgang Hofmeister

1. Berichterstatter:

2. Berichterstatter:

Tag der mündlichen Prüfung:

Die vorliegende Arbeit wurde am Max-Planck-Institut für Polymerforschung in Mainz und am Austrian Institute of Technology (AIT) in Wien in der Zeit von Mai 2006 bis August 2009 angefertigt.

Abstract

The transmembrane potential difference $\Delta\phi_m$ is closely associated to the catalytic activity of *cytochrome c oxidase* (CcO). CcO is the terminal enzyme (complex IV) in the electron transport chain of the mitochondria. The enzyme catalyzes the reduction of O_2 to $2\,H_2O$, thereby electrons are transferred from *cytochrome c* to CcO. Electron transfer within the CcO is coupled to proton translocation. Consequently, a difference in proton concentration over the inner mitochondrial membrane and a membrane potential difference $\Delta\phi_m$ are generated.

The transmembrane potential $\Delta\phi_m$ can be measured by fluorescence spectroscopy using a potential sensitive dye. Before quantitative results can be deduced from such investigations, calibration measurements using defined electrical potentials applied to the lipid membrane have to be conducted.

Here, calibration measurement of $\Delta\phi_m$ in a model membrane with CcO are presented. $\Delta\phi_m$ is induced by defined external potentials applied to the lipid membrane. Therefore, a model membrane system called the protein-tethered bilayer lipid membrane (ptBLM) was developed on the transparent, semi-conducting substrate indium tin-oxide (ITO). ITO enables simultaneous implementation of electrochemical and fluorescence or optical waveguide techniques.

A thin hydrogel layer was used as a soft 'cushion' for the ptBLM on ITO, providing the nickel chelating nitrilo-triacetic acid (NTA) groups, to which CcO from *Paracoccus denitrificans* was bound in a well defined orientation via a his-tag attached to its subunit I. The ptBLM was then formed by *in-situ* dialysis using bio-beads. Electrochemical impedance spectroscopy showed good electrical sealing properties ($\approx 1\,\mathrm{M\Omega \cdot cm^2}$). Surface plasmon resonance optical waveguide spectroscopy (SPR/OWS) indicated an increased anisotropy of the system after formation of the lipid bilayer. Cyclic voltammetry in the presence of reduced *cytochrome c* demonstrated that CcO was incorporated into the gel-supported ptBLM in a functionally active form. The membrane potential induced in a gel-supported ptBLM by an external voltage waveform was measured by ratiometric fluorescence spectroscopy. Reference measurements using a tethered BLM provided a conversion factor in terms of the ratiometric parameter $\mathrm{R_n}$ (0.05/100 mV). Potential changes induced in the ptBLM by external voltage were measured down to ≈80 mV. These data provide a basis for future investigations of the self-generated $\Delta\phi_m$ of CcO in a ptBLM.

Contents

Chapter 1

Introduction

The lipid bilayer membrane plays a prominent role in many biologically relevant processes. Examples are signal transduction, transport of ions and molecules, biosynthesis, cell adhesion and recognition. Natural membranes are usually of great complexity and the investigation of single species of membrane proteins is hard to realize using common analytical techniques. Artificial lipid membrane systems have to be designed to mimic the conditions of a biological membrane and the protein of interest has to be re-constituted into the membrane. Proteolipsomes were often used to incorporate membrane proteins[70, 133]. Even though transport processes through membrane proteins could be investigated, this method had two major drawbacks, accumulation of transported species in the inner compartment and the lack of control over the membrane potential. Black lipid membranes (BLM) do overcome this problem, but exhibit a low mechanical stability.

If the lipid membrane is tethered to a solid support, i. e. a planar electrode surface, the bilayer can be stabilized and membrane proteins can be incorporated into the membrane in a functional manner. These so-called tethered BLMs (tBLM)[65, 91, 114, 138] allow the application of various surface analytical tools including electrochemical techniques. Ion transport across lipid membranes facilitated by membrane proteins could thus be investigated. Channel peptides, such as mellitin and gramicidin, and ion carriers, such as valinomycin, were successfully incorporated[7, 23, 46, 92, 116]. They were shown to transport ions with similar ion transfer rates as in classical bilayer or BLMs[92]. Larger and more complex enzymes such as *cytochrome c oxidase* (CcO) were also incorporated. However, relatively small catalytic currents were measured by cyclic voltammetry (CV)[24, 52, 91]. Similar results were obtained for CcO immobilized in a complex with *cytochrome c* (cyt c)[45]. Moreover, the lower leaflet of the lipid bilayer is not fluid due to the tether moities covalently attached to the surface. This prevents incorporation of large membrane proteins.

In an attempt to preserve the catalytic activity of such proteins immobilized on surfaces, a bio-mimetic membrane system was developed in our group in which the proteins are immobilized on a planar electrode using the histidine-tag (his-tag) technology. A lipid bilayer is then reconstituted around the bound proteins by *in situ* dialysis to form the protein-tethered bilayer lipid membrane (ptBLM)[38]. The most obvious advantage of this system is the strict control over the orientation of the protein.

Recently, it was shown that the CcO from Rhodobacter sphaeroides, embedded in such a system with the his-tag attached to subunit (SU) II, can be effectively activated by direct electron transfer (ET). This was demonstrated by electrochemical methods in combination with surface-enhanced resonance Raman spectroscopy (SERRS) and surface-enhanced IR absorption spectroscopy (SEIRAS)[33, 58]. On the other hand, when the CcO from Paracoccus denitrificans is immobilized with the his-tag attached to SU I, the cyt c binding site is directed away from the electrode to the outer side of the tBLM architecture. The protein can then be activated by cyt c to actively transport protons across the lipid bilayer structure[35].

Model systems that have been developed for the investigation of membrane proteins are described in the following.

1.1 Membrane Model Systems for the Investigation of Membrane Proteins

The first membrane model systems introduced in the early 1960s were lipid bilayer membranes, either produced in the form of a sphere such as liposomes and giant unilamellar vesicles (GUV)[20, 71, 108], or as a two dimensional planar system separating two aqueous reservoirs such as the BLM.[9, 44, 86]. Several ion transport channels and receptors have been characterized for their electrochemical and kinetic properties using these model systems.

For membrane studies towards the investigation of membrane proteins and the associated application as a sensing system, liposomes have a limited relevance, as the inner compartment is very small and inaccessible to chemical manipulation. Electrical measurements can only be realized in a patch clamp configuration. This limitations can be overcome by the formation of supported planar lipid bilayers (sBLM)[11, 69, 110, 111]. These membrane systems are formed directly on the metal or semi-conductor electrode surface. However, the main drawback of such supported model membrane systems reported in the early years was the strong interaction of incorporated proteins with the solid support leading to immediate denaturation.

This limitation can be overcome by a tethering moity attaching the membrane to a solid support. These types of membranes are of special interest due to their high mechanical stability and therefore will be described in the next section. Another advantage is the possibility to use various surface analytical tools for the characterization and study of these systems that are not applicable with vesicles and BLMs, such as microscopic techniques, AFM, ellipsometry, FRAP, SPR, EIS and QCM-D[115].

1.1.1 Tethered BLM on metal electrodes

The use of a clearly defined, short tethering unit, which is on one side covalently bound to the support like a gold substrate and on the other to the lipid building the inner leaflet of the bilayer, is one of the possibilities of building tethered bilayer lipid membranes (tBLM). The backbone of such a tethering molecule can be build using alkyl chains[39], phospholipids [68, 89, 117] or cholesterol derivatives[50] bound via the tether unit to the anchor group that is sulphur bearing end groups[121, 128] for the case of a gold support (Fig. 1.1). For silicon oxide surfaces silanes have been used [4]. The anchor lipids can self-assemble on the surface and directly form the first lipid monolayer. The outer leaflet can be deposited by either vesicle fusion or solvent exchange methods. The spacer acts as an elastic buffer, separating the bilayer from the support and providing a small ionic reservoir[90, 117, 126, 134].

The first tBLM architecture was reported by Vogel and co-workers[68], who synthesized so-called thiolipids consisting of two disulphide-linked hydrophilic spacer groups of 1-3 ethoxy groups which are coupled to a phospholipid. They employed Langmuir Blodgett film transfer and self-assembly for the monolayer preparation and completion to a bilayer was achieved by detergent dilution. The properties of the tBLM depend strongly on the tethering part, as the interaction of the lipids with the solid is very important and has to be tuned carefully[109]. For example, the diffusion properties of the two leaflets of the bilayer are important for the incorporation of small proteins, whereas the high electrical sealing properties are major factors in order to separate

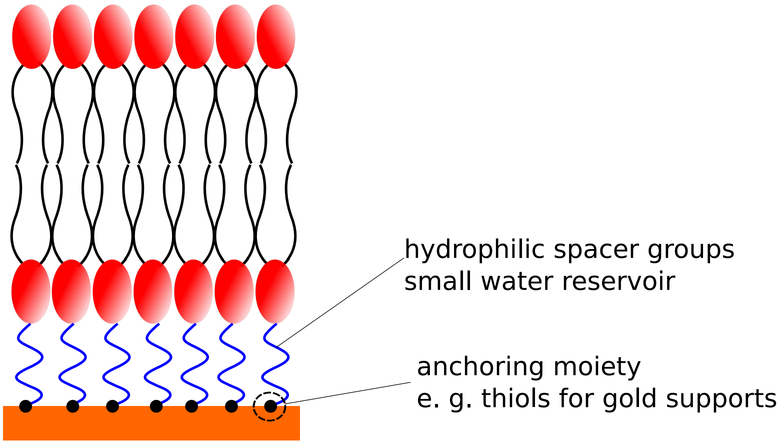

Figure 1.1: Schematic representation of a tethered BLM on a solid substrate. The sub-membrane space consists of anchor lipids attaching the first leaflet of the membrane to the support. The chemical method used for anchorage depends on the support. For gold supports thiols are used in most cases.

the protein signal from the leak current of the membrane. Self-healing of defects in the membrane architecture can also be of interest, as defects enhance the leakage of the membrane. Furthermore, the size and nature of the water reservoir below the membrane is of great importance, as it is a prerequisite to enable measurements of leakage or flux.

Many different spacer groups have been used throughout literature, the most common being ethylene oxide[3, 63, 64, 109, 128, 134]. However an alternative are oligopeptide sequences attached to the anchor group, which then form a peptide-tethered membrane[60, 91, 103, 117]. Cornell et al. were the first to use archaea lipids with phytanyl chains to stabilize the bilayer structure . Additionally they introduced full membrane spanning lipids to further enhance the stability of the architecture[23]. Based on a similar approach, Schiller synthesized a new thiolipid using phytanyl chains [116]and a tetraethylene glycol moiety linked to the lipoic acid anchor group yielding a molecule named di-phytanyl-glycerol-tetraethylene glycol-lipoic acid ester lipid (DPTL). With this molecule bilayers with resistances in the $10\,\mathrm{M\Omega{\cdot}cm^2}$ range and capacitances around $0.7\,{}^{\mu F}\!/_{cm^2}$ could be obtained, which is comparable to the values reported for BLMs.

tBLMs on oxidic surfaces and semi-conductor surfaces were also reported using the same strategy[3]. A different approach to obtain tBLMs is the use of hanging mercury drops as a electrode[103], as mercury has the advantage of providing a defect-free fluid surface. Using this strategy, tBLMs with a thiol peptide spacer could be obtained that were functionalized with valinomycin, though the electrochemical properties of these layers were quite low. On mercury it is possible to use the same anchorlipid (DPTL) than on gold surfaces to improve the sealing properties of the bilayer. However the resistance of the resulting bilayers is at its best around $0.2\,\mathrm{M\Omega{\cdot}cm^2}$ with capacitances around $1\,{}^{\mu\mathrm{F}}/_{\mathrm{cm}^2}$ showing a poor organization of the bilayer as compared to those on gold surfaces.

1.1.2 Protein-tethered BLM on metal electrodes

tBLMs have some major drawbacks despite their good sealing properties and mechanical stability. The spacer molecule which is also the anchor to the support has to be chosen appropriately in order to allow for a adequate reservoir in the sub-membrane space. Further, the spacer molecule itself hinders functional incorporation of membrane proteins into the tBLM.

A new model system, the protein-tethered bilayer lipid membrane (ptBLM), for the investigation of membrane proteins has been developed in our group on noble metal substrates[38, 96]. It is formed by, first immobilizing the protein utilizing the his-tag technology, while it is stabilized by detergent molecules. Then the protein is used as a scaffold to form a lipid bilayer. which is done by in-situ dialysis using bio-beads. Thereby, the detergens molecules are replaced by lipids and a bilayer forms around the protein. Surface analytical techniques such as SPR, EIS, SEIRAS and SERRS have been employed as yet[34, 58, 96]. The advantage of this method is that the protein is reconstituted in a bilayer in a functional manner. The size of the sub-membrane space is defined by the cytosolic part of the protein. Moreover, the membrane protein is incorporated in a well defined orientation, predetermined by the location of its histidine anchor.

The His-tag technology is based on the strong affinity of polyhistidine to metal complexes formed by nickel or cobalt ions. This property is utilized in the purification of polyhistidine-tagged proteins expressed in prokaryotic cells. Therefore, high affinity media such as Ni Sepharose are employed. These media contain bound metal chelate complexes, very often formed using a chelating compound such as nitrilotriacetic acid (NTA). During purification the his-tagged protein binds specifically to the

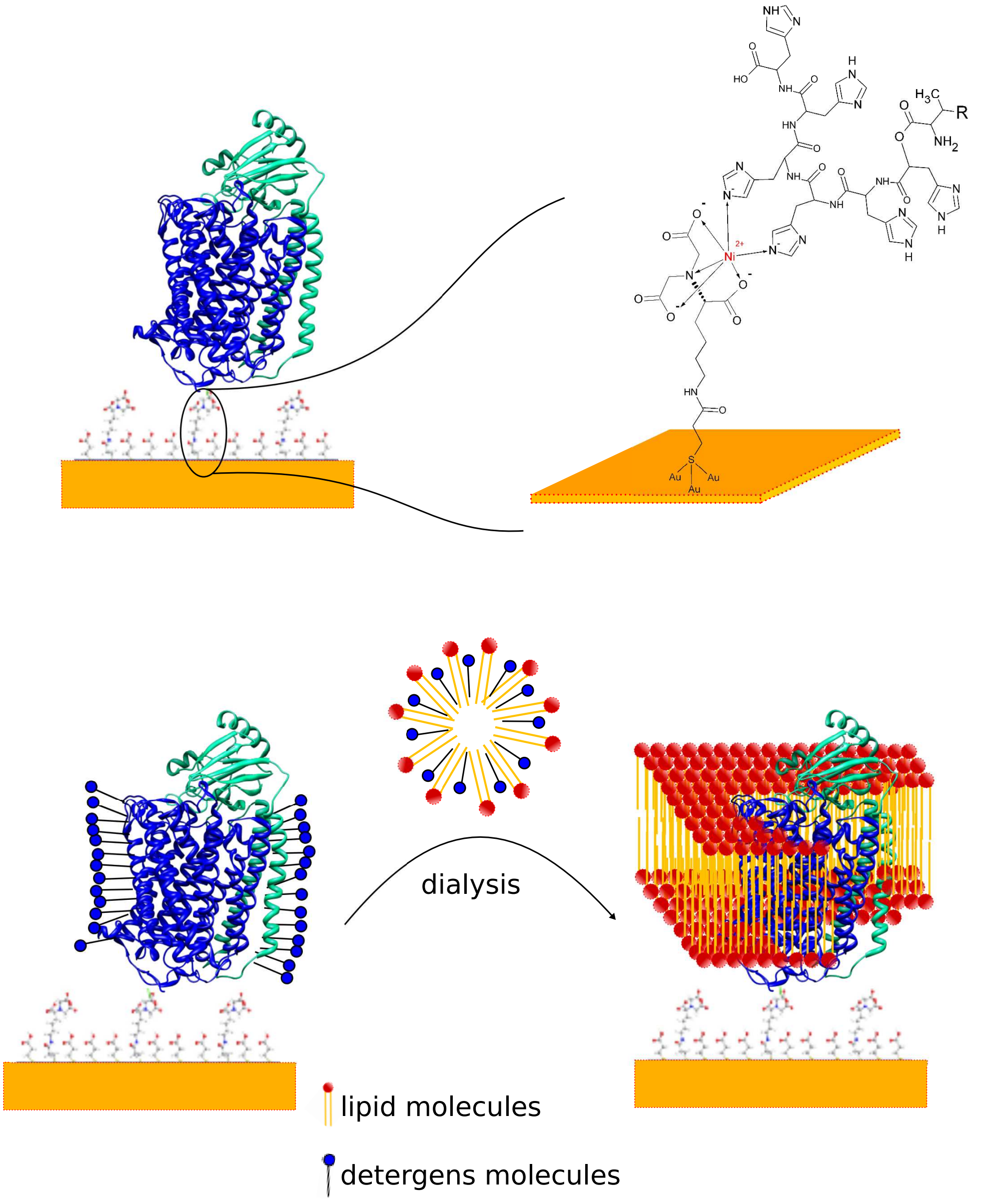

Figure 1.2: (a) Surface functionalization on gold for the immobilization of *cytochrome c oxidase* with the his-tag attached to SU I. The his-tag technology has been utilized in order to bind the membrane protein to the gold surface. (b) Schematics of the reconstitution of *cytochrome c oxidase* (CcO) into a ptBLM by *in-situ* dialysis.

metal chelate complex. Unspecific bound proteins are removed by subsequent washing. NTA-Ni^{2+} based affinity media show the highest binding capacity, whereas Co based resins offer the highest purity of the sample.

This technique is also suitable for the immobilization of membrane proteins onto electrode surfaces. For example, his-tagged *cytochrome c oxidase* was immobilized on gold in a analog manner. The surface was functionalized using dithiopropionate bearing a NTA terminal. The sample is incubated in a Ni^{2+} solution. NTA forms an octaheadral coordination complex with Ni^{2+}. Two of the coordination sites are occupied by water molecules. Upon binding of the CcO, the his-tag replaces the water molecules and coordinates to the NTA-Ni^{2+} chelate. Afterwards the protein is reconstituted into a lipid bilayer.

The His-tag is commonly located at the N- or C-terminus of a subunit within the protein. For CcO with the His-tag at the C-terminus of subunit II the protein was oriented with the cyt c binding site directed toward the electrode (down-configuration). Bio-electronic coupling of the protein to the electrode is achieved only in this orientation, when the primary electron acceptor, the Cu_A center, was directed toward the electrode. CcO with the His-tag at the C-terminus of subunit I allows the immobilization of the protein such that the cyt c binding site is showing to the opposite direction, away from the electrode. In this orientation the cyt c binding site is accessible to freely diffusing electron donors in the bulk solution.

1.2 Significance of the Membrane Potential

All cells in organisms are able to regulate the influx of important resources from their environment through the membrane into the cell compartment in order to run vital processes for intracellular bio-synthesis and energy production. At the same time waste products have to be transported out of the cell comportment, pH and water concentration are controlled in the same manner. The plasma membrane plays a critical roll in the regulation of influx and outflow's of ions and substances. The regulatory mechanisms can be separated into passive (e.g. diffusion driven) and active (e.g. proton pump) transport routes across the membrane. Some proteins, incorporated into the membrane, are able to specifically mediate the transport of solutes like nutrition's, amino acids or inorganic ions. In the passive route, carrier proteins (permeases), or

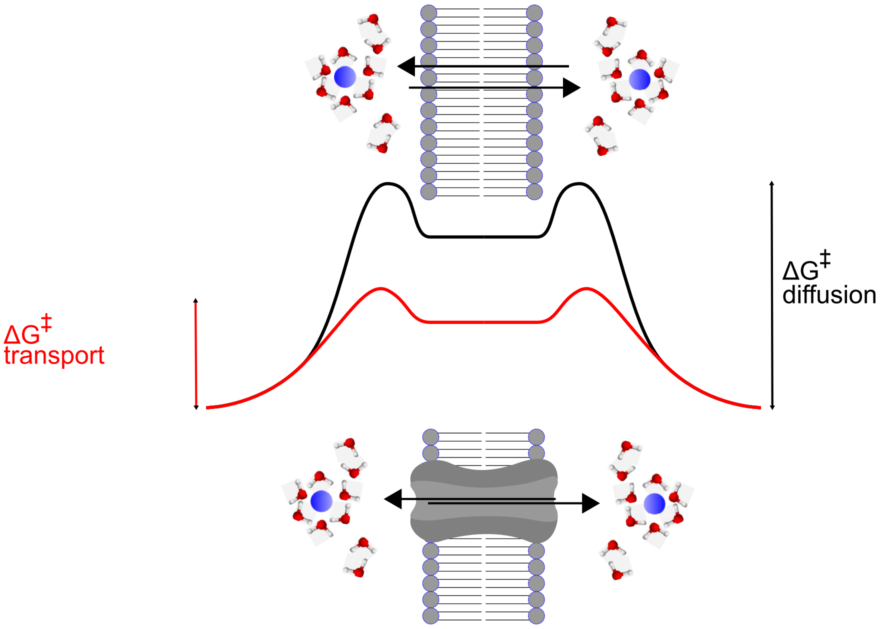

Figure 1.3: Change of the Gibbs free energy during the passage of an ion through the lipid membrane. Detachment of the hydration shell is a highly endorgenic process. A higher activation energy is required for simple diffusion of ions through the lipid bilayer compared to carrier mediated transport.

ion channels do efficiently transport molecules and ions, since the membrane is virtually impermeable to the relevant substances. Other proteins are even able to 'pump' - active transport - against an electrical or a concentration gradient, in contrast to the passive case where the transport always occurs along such a gradient. In the case of ion translocation across the membrane in either direction the transport processes is closely associated with the electrical fields formed across the membrane. In the next section the transport process of ions will be described in more detail. Later the focus will be on the active ion transporters in the respiratory chain and more specifically the proton pump *cytochrome c oxidase*.

1.2.1 Passive ion transport

The concentration difference of ions between the inner comportment, enclosed by the membrane, and the environment causes the diffusion of ions through the lipid membrane. While passing through the bilayer, the ion has to leave the energy minimum which it reached due to the formation of the hydration shell around it, move from a high dielectric constant region (aqueous phase) through a 3 nm thick lipid bilayer with a low dielectric constant and a hydrophobic interior and, finally, enter the aqueous phase on the opposite site. Consequently, the membrane acts as a high energy barrier to the diffusion of ions. Accordingly a high activation energy $\Delta G^{\ddagger}$ is required in order to get the ion from one side of the membrane to the other. Simple diffusion of ions through the membrane is a very slow process with time constants reaching several hours.

Based on the solubility-diffusion mechanism frequently referred to[29, 81, 105], the Gibbs free energy of the diffusion process can be separated into several terms describing the electrostatic, hydrophobic and other specific energy barriers that the ion has to permeate[101]

$$\Delta G^{\ddagger} = \Delta G_B^{\ddagger} + \Delta G_I^{\ddagger} + \Delta G_D^{\ddagger} + \Delta G_H^{\ddagger} \tag{1.1}$$

A continuum model is taken for the description of the bilayer, i.e. the membrane as a structureless, continuous dielectric layer separating the two aqueous phases. $\Delta G_B^{\ddagger}$ is than the Born energy describing the electrostatic energy required to place a charge from the aqueous phase into the interior of the hydrophobic layer. The second electrostatic term arises from the force acting on a charge q placed close to the interface separating two dielectric half spaces ϵ_1, ϵ_2. q located in ϵ_1, induces an image counter charge Q' in ϵ_2. Hence, an electrostatic image force acts on the ion close to the interface leading to $\Delta G_I^{\ddagger}$ in eq. 1.1. The last electrostatic term, $\Delta G_D^{\ddagger}$, describes the contribution of the membrane dipole potential, induced by the carbonyl groups at the head of lipids, to the Gibbs free energy. Observations show that it is due to the dipole potential that anions diffuse faster through the membrane than cations of comparable size[31, 32]. Consequently, $\Delta G_D^{\ddagger}$ is negative for anions, lowering the energy barrier imposed by the bilayer for anions in comparison to cations. The last term $\Delta G_H^{\ddagger}$ takes into account the energy that is required to remove an ion from the aqueous phase and place it into the hydrocarbon region of the membrane, since the hydrophobic effect causes a substantial barrier to ion diffusion, $\Delta G_H^{\ddagger}$ can outweigh the combined electrostatic effect represented by the other three terms.

Various semi-empirical approaches exist in order to quantify $\Delta G^{\ddagger}$ by expressing each term in eq. 1.1 into a mathematical form[31, 93, 100]. The different models will not be described here. Once $\Delta G^{\ddagger}$ can be determined the permeability P of the membrane can be calculated using an equation derived from Ficks first law of diffusion

$$
\begin{aligned}
P &= \frac{KD}{d} && (1.2)\\
K &= \exp{-\Delta G^{\ddagger}/RT}. && (1.3)
\end{aligned}
$$

However, there were strong evidences suggesting that some mechanisms facilitate permeation of ions at considerably higher rates, e.g. the transmembrane potential was shown to be influenced by the passive permeation of ions through biological membranes, especially in electrically active tissues[104] which can only be explained by an additional, faster permeation process through the lipid matrix.

Transient defects within the membrane produced by thermal fluctuations[85], electric fields[12, 55, 131, 136], antimicrobial peptides[16, 107, 118] or mechanical stress[13, 25] can offer a pathway for ion permeation, avoiding the Born energy barrier associated with the solubility-diffusion mechanism. The bypass is formed by hydrophilic and hydrophobic pores in the membrane, of which the latter are of particular relevance for cations permeating thin lipid bilayers. Moreover, the electroporation method for example, where pores are intentionally induced by applied electric fields, allows the introduction of foreign agents, genes or peptides into the cell and thus became an important tool in cell biological applications.

In free-suspended BLMs on electrodes, where defined electrical fields can be applied to the bilayer, electroporation can become the dominating mechanism for passive, pore-mediated ion transport. The population of aqueous pathways is closely associated to the increased permeability P of the membrane to ions (electropermeabilization). The effect on P can be quite well described using theoretical models, though the structure of the pores or the phase transition itself, i.e. the different states of pore formation, are difficult to determine. For that reason, in the following electropermeabilization will be further elucidate. Formation of hydrophilic pores most likely arises from the transformation of hydrophobic pores, which are formed as a consequence of lateral thermal fluctuations. Thermal fluctuation is a zero order process which in turn can be modelled according to the absolute rate theory for chemical reactions. The change of Gibbs free energy for pore formation can be described as[135]

$$
\begin{aligned}
\Delta G_p^{\ddagger}(\Delta\phi_m, r) &= W_{mech} + W_{el} && (1.4)\\
W_{el} &= \Delta\phi_m^2 \pi r^2 (\epsilon_w - \epsilon_m)/2d_m && (1.5)
\end{aligned}
$$

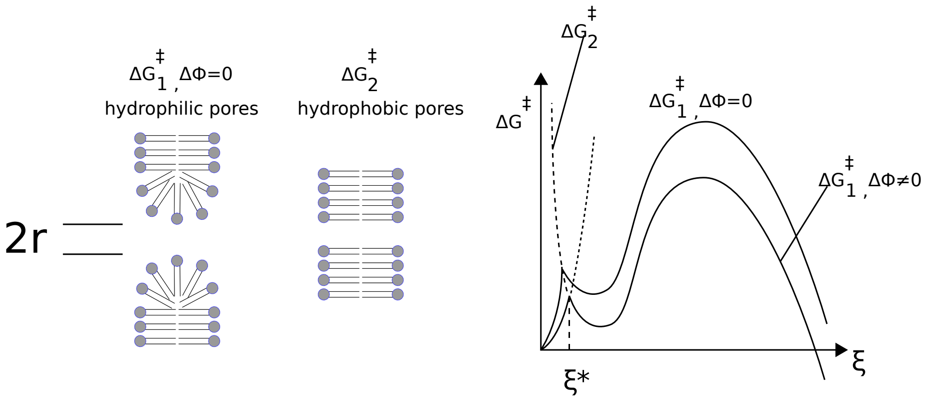

Figure 1.4: Examples of the formation energy (right) of single pores with radius r in a lipid membrane eq. (1.4). Schematic presentation of the two basic pore types is shown on the left: hydrophilic (dashed line) and hydrophobic (solid line) pores. At nonzero electrical potentials the energy barrier is lowered significantly (second curve in graph).

The electrical work $\mathrm{W_{el}}$ is determined by the membrane thickness $\mathrm{d_m}$, it's dielectric constant ϵ_m, the ϵ_w of the aqueous phase, the pore radius r and the electric potential $\Delta\phi_m$. The mechanical work for pore formation can be described by simply taking the change of surface area of the lipid film compared to that of the pore edges. However, the hydrophobic interaction of the pore edges has also to be taken into account. This leads then to[135]

$$W_{mech} = 2\pi r d_m \gamma(r) \tag{1.6}$$

$$\gamma(r) = \gamma_\infty I_1(r/r_0)/I_0(r/r_0) \tag{1.7}$$

The tension at the interface between the hydrophobic lipid tails and the water column in the pore is taken into account by $\gamma(r)$, where I_0, I_1 are the modified Bessel functions of n-th order. r_0 is a scaling length. The rate constant of pore formation is then

$$k_p \propto \exp -\frac{\Delta G_p^\ddagger}{kT}. \tag{1.8}$$

The free energy $\Delta G^\ddagger(\Delta\phi_m, \xi)$ can be written as a function of the dimensionless radius $\xi = r/d_m$. At $\Delta\phi_m$=0 the left term of eq. 1.4 leads to the first energy curve $\Delta G_1^\ddagger$ in Fig. 1.4. Below the critical radius ξ^* - the intersection between hydrophobic and hydrophilic curve - formation of hydrophilic pores having small radii requires so much energy (dashed part of curve 1 in Fig. 1.4) that this transformation becomes very unlikely. Hydrophobic pores dominate in this regime. Above the critical radius, the rearrangement of lipids becomes energetically more favorable resulting in the formation of hydrophilic pores. Additionally, if a electrical field is applied, $\Delta\phi_m \neq 0$, the energy barrier for pore formation is further lowered (see $\Delta G_2^\ddagger$ in Fig. 1.4).

Finally, since the total permeability of the membrane at steady state is proportional to the accumulation of hydrophilic pores, P can be written as[113]

$$P(\Delta\phi_m) = P_0 \exp - \frac{\Delta G_p^\ddagger}{kT} \tag{1.9}$$

where P_0 is the total permeability at $\Delta\phi_m = 0$. The resealing of the pores is considered to be independent of $\Delta\phi_m$.

In general, ion permeation by pores is the dominant mechanism in passive transport only if the membrane is sufficiently thin in terms of ξ. For increasing membrane thickness ion transport through partition and diffusion, as described before, become of greater importance.

Solubility-diffusion and electroporation prove to be relative simple models that describe passive ion permeation very well. Unfortunately, these theoretical tools do not account for the molecular structure and the inhomogeneity of the membrane. Molecular dynamics simulations (MD) offer a great potential in this respect, however, are out of the scope of this work. Lately in our group ion transport across tBLMs was modeled using a electrical hybrid network description which combines potential dependent rate equations with passive electrical elements. Passive permeation of ions was described by the integrated Nernst-Planck Flux equation. Simulations based on this model were then performed using the network simulation program SPICE (Simulation Program with Integrated Circuit Emphasis). The concept of this method will be presented later in this work.

In the next sections active ion transport will be described taking the proton pump CcO from the respiratory chain as an example.

1.2.2 The respiratory chain

The main function of the respiratory chain is the conversion of the Gibbs free energy released during the reduction of oxygen through NADH and $FADH_2$ into the chemical form adenosine triphosphate (ATP). ATP is the universal energy source in living organisms. Almost all energy consuming processes such as nerve stimuli or muscle contraction are driven by ATP. The metabolic pathway that consumes energy released through oxidation of nutrients such as glucose to produce ATP is denoted as the oxidative phosphorylation, since adenosine phosphate (APD) is phosphorylated to form ATP using the energy released by the reduction of oxygen to water. This process of conversion of nutrients under aerobic condition (oxygen as the oxidizing agent) delivers higher amounts of energy than any other oxidative pathway. Nevertheless, oxidative processes involving oxygen usually generate free radicals which have a toxic effect to organisms. The nature has developed specialized enzymes in order to avoid such dangerous intermediate products. Oxygen reduction is catalyzed by these enzymes in a controlled manner.

The reduction of molecular oxygen to water through NADH and $\mathrm{FADH_2}$ is a reaction involving a sequence of electron transfer steps through a chain of membrane proteins, denoted as the respiratory chain. The respiratory chain in eukaryotic cells is located within the inner membrane of the mitochondria, whereas in prokryotic cells it is located within the cytoplasmic membrane.

In the mitochondria the system consists of the electron transfer chain, which is coupled to proton translocation, and the ATP-synthase. The electron transfer pathway consist of the integral membrane proteins, complex I to IV. The driving force of the oxidative phosphorylation, and proton translocation from the matrix to the inter-membrane space in the mitochondria, is the high electron transfer ability of the energy-rich NADH compared to that of the molecular oxygen. The chemical reaction consists of several reaction steps taking place within the proteins in the chain and is described by

$$\tfrac{1}{2}\mathrm{O_2} + \mathrm{NADH} + \mathrm{H^+} + 10\,\mathrm{H^+_{in}} \longrightarrow \mathrm{H_2O} + \mathrm{NAD^+} + 10\,\mathrm{H^+_{out}}. \tag{1.10}$$

The change in Gibbs free energy of the reaction is

$$\Delta G = \Delta G^o + RT\ln\frac{[\mathrm{NAD^+}][\mathrm{H_2O}]}{[\mathrm{NADH}][\mathrm{H^+}][\mathrm{O_2}]} + RT\ln 10(pH_{out} - pH_{in}) + nF\Delta\phi_m \tag{1.11}$$

where ΔG^o is the standard change of Gibbs free energy, R the universal gas and F the Faraday constant. $\mathrm{pH_{in}}$ is the pH in the matrix and $\mathrm{pH_{out}}$ is the pH in the inter-membrane space. $\Delta\phi_m$ is the transmembrane electrical potential. The first two

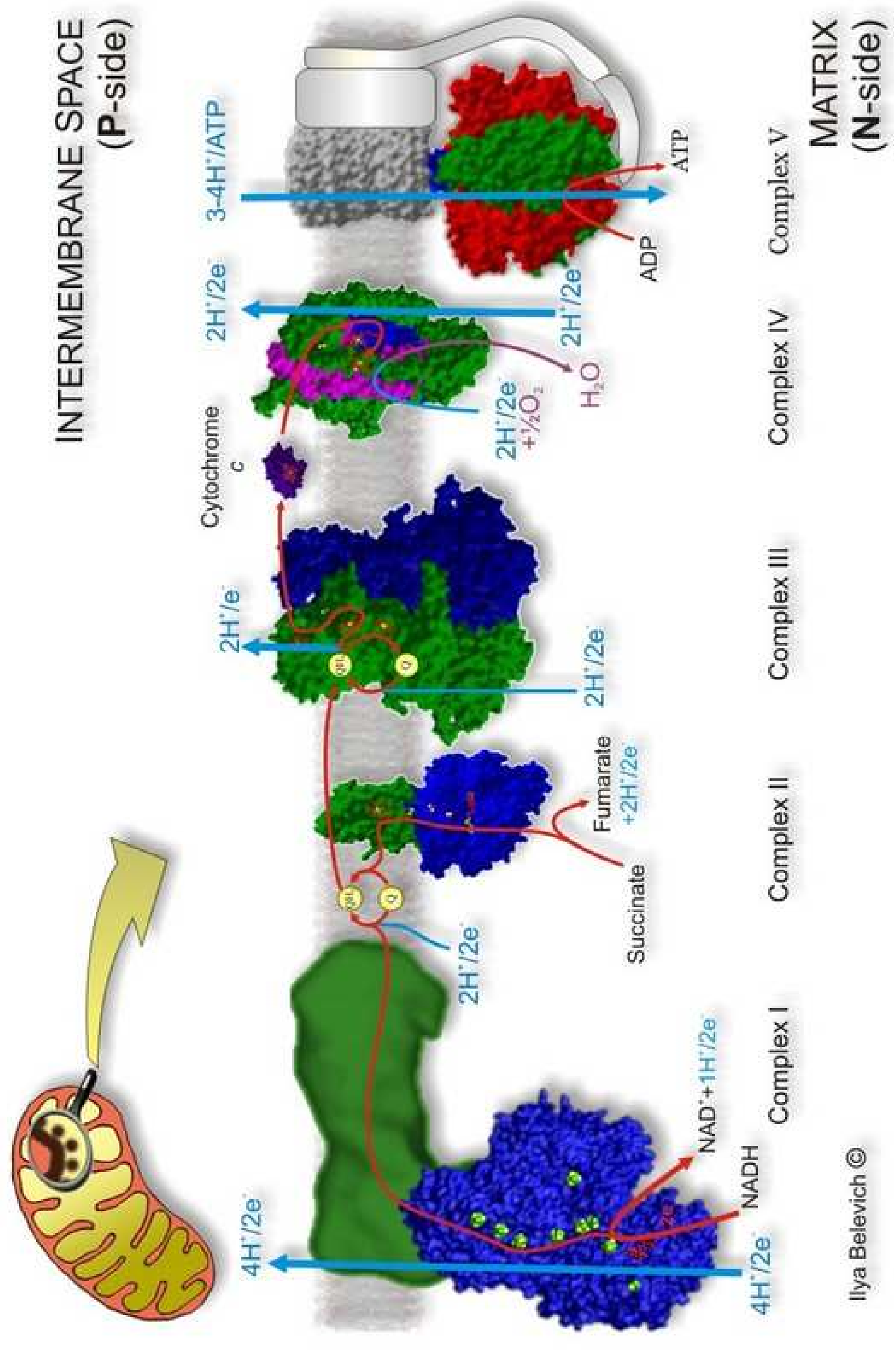

Figure 1.5: The mitochondrial respiratory chain. Picture: ©Ilya Belevich, Biocenter, University of Helsinki.

terms describe the change in Gibbs free energy due to the chemical reaction. The last two terms consist of the difference of the chemical potential, as a consequence of the difference of the concentration of protons between the intermembrane space and the matrix, and the electrical potential difference across the membrane. The theoretical value of ΔG is -220 $^{\mathrm{kJ}}/_{\mathrm{mol}}$. Under normal conditions the pH of the intermembrane space is 1.4 lower than that of the matrix. The membrane potential usually has a value around 0.14 V where the matrix is more negative than the intermembrane space. Applying these values to the last two terms (1.11) yields a change in Gibbs free energy for the translocation of one proton across the inner membrane to the inter-membrane space

$$\Delta\tilde{\mu}_{H+} = 21.82\,^{\mathrm{kJ}}/_{\mathrm{mol}} \tag{1.12}$$

hence the overall change in $\Delta\tilde{\mu}_{H+}$ during one cycle, where 10 protons are translocated, is 218,2 $^{\mathrm{kJ}}/_{\mathrm{mol}}$ and very close to -220 $^{\mathrm{kJ}}/_{\mathrm{mol}}$ released during the chemical reaction. The energy released by the reduction of molecular oxygen is used to form a pH difference and a change of membrane potential $\Delta\phi_m$ across the inner membrane of the mitochondrial.

The sequential electron transfer path from NADH to O_2 is formed by a chain of three trans-membrane proteins: the complex I NADH-coenzyme Q *oxidoreductase* (NADH-CoQ), the complex III *cytochrome c oxidoreductase* (bc_1-complex) and the complex IV *cytochrome c oxidase* (CcO). Electron transfer from NADH-CoQ to bc_1-complex is mediated by the coenzyme *ubiquinone Q*. Ubiquinone also plays a role in the transfer of electrons from $FADH_2$ over complex II to the bc_1-complex. This reaction is part of the citric acid cycle and takes course at the membrane complex *succinate dehydrogenase* (SQR). SQR catalyzes the reduction of succinate to fumarate and the electrons generated from this reaction are transferred sequentially to ubiquinone thereby reducing it to ubiquinol. The final transfer of electrons in the transport chain is to the complex IV (CcO). The transfer is mediated by its substrate *cytochrome c*.

The electron transport through all these complexes is coupled to proton translocation over the inner membrane of the mitochondrion. Consequently, a difference in pH and electrical potential is formed between either side of the membrane. According to the Chemiosmotic Theory proposed by Mitchell[84], this two factors determine the proton-motive force driving the ATP-synthase to produce ATP from ADP and the anorganic phosphate P_i.

1.2.3 Cytochrome c oxidase and active proton transport

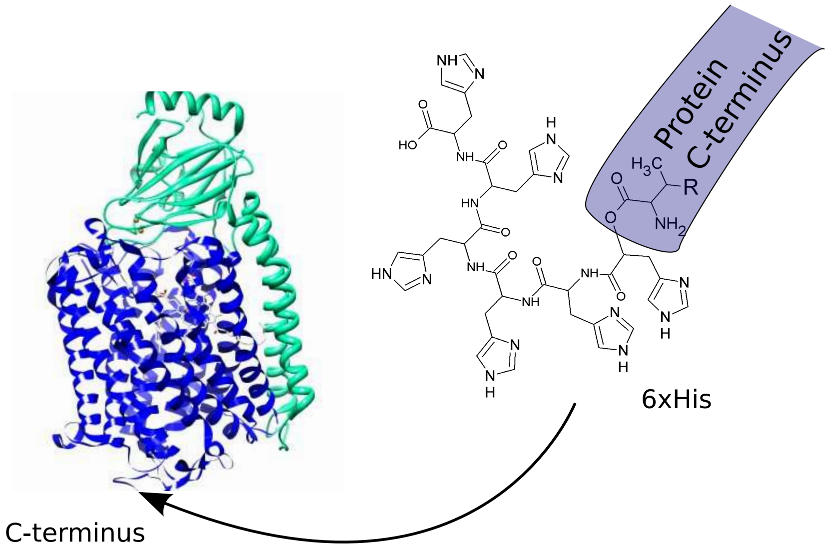

Figure 1.6: Structure of the two subunit CcO from *P. denitrificans* with a 6xHis-tag at the C-terminus of subunit I (blue) [61]. Subunit II is shown in turqiouse.

As already explained, the CcO is the terminal complex of the electron transport chain in the mitochondria. CcO catalyzes the reduction of O_2 to $2\,H_2O$. The work presented here will focus on the bacterial complex IV, the CcO from *paraccocus denitrificans* [78, 79, 124]. The structure of the protein from prokaryotic organisms is by far less complex compared to the structure of CcO from the mitochondria. Moreover, genetic alteration of the proteins from prokaryotic organisms can be easly realized. Because of the homology between the prokaryotic and the mitochonrial protein complexes and their identical functionality, the results from experiments on membrane proteins from the bacterial respiratory chain can be directly related to the mitochondrial proteins.

The CcO in this work incorporates a 6xHist-tag at the C-terminus of subunit I. The His-tag was attached through genetic modification. The protein complex consist of two heme centers, heme a and heme a_3, and three copper ions denoted in two Cu centers, Cu_A and Cu_B. The Cu_A-domain comprises both the binding site for the substrate (*cytochrome c*) and the electron entry site of the CcO. The heme a_3-Cu_B pair is the catalytic site of the complex, i. e. where the reduction of O_2 to $2\,H_2O$ is taking place. Therefore, during enzyme turn over four electrons from reduced cyt c are consecutively transferred from Cu_A, over heam a, to the catalytic site of the complex.

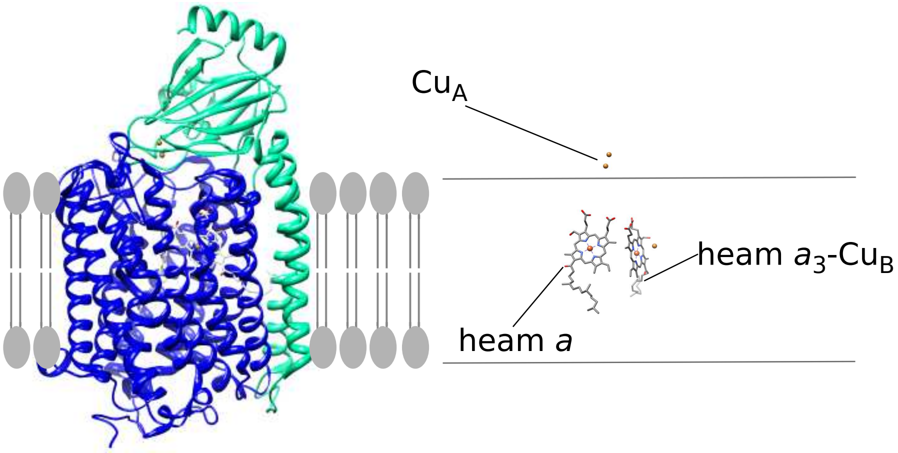

Figure 1.7: Location of the electron acceptor sites in CcO from *P. denitrificans* relative to the membrane surfaces.

Electron transfer is coupled to an uptake of four substrate H_s^+ and four translocated protons H_p^+ from the proton-input (N) to the output side (P). The overall reaction catalyzed by CcO is

$$4\,\mathrm{cytc}^{+2}_{\mathrm{P-side}} + \mathrm{O}_2 + 4\,\mathrm{H}^+_\mathrm{s} + 4\,\mathrm{H}^+_{\mathrm{p(N-side)}} \longrightarrow 4\,\mathrm{cytc}^{+3}_{\mathrm{P-side}} + \mathrm{O}_2 + 2\,\mathrm{H}_2\mathrm{O} + 4\,\mathrm{H}^+_{\mathrm{p(P-side)}} \quad (1.13)$$

In the R intermediate (Fig. 1.8b) the catalytic site was reduced by the uptake of two electrons forming the heme $a_3(\mathrm{Fe}_2^+)/\mathrm{Cu}_\mathrm{B}^+$. Protons transfer was linked to this electron transfer and resulted in two protons already present at the catalytic center and two protons pumped from N to P side. At this state the complex is able to bind molecular oxygen. In a recent report [141] it was suggested that O_2 is bound to Cu_B site before the A state is formed when O_2 binds to the ferrous heme a_3. The O-O bond is broken in a concerted reaction. To break the O-O bond, four electrons and at least one proton is required. Two of the electrons are donated by the heme a_3 iron forming the ferryl state (Fe_4^+). The source of the additional electron depends on whether heme a is oxidized, drawn as the dashed route to P_M in the circle Fig. 1.8b, or reduced, the path through P_R, when oxygen binds to the reduced catalytic site.

The state of the catalytic site formed by the reduction either of the P_M or P_R intermediates is denoted as F. The difference between this two intermediates lays only in the tyrosinate radical formed at the catalytic site in the P_M state but not in the P_R state. In both of this branches the transfer of one electron is coupled to the uptake

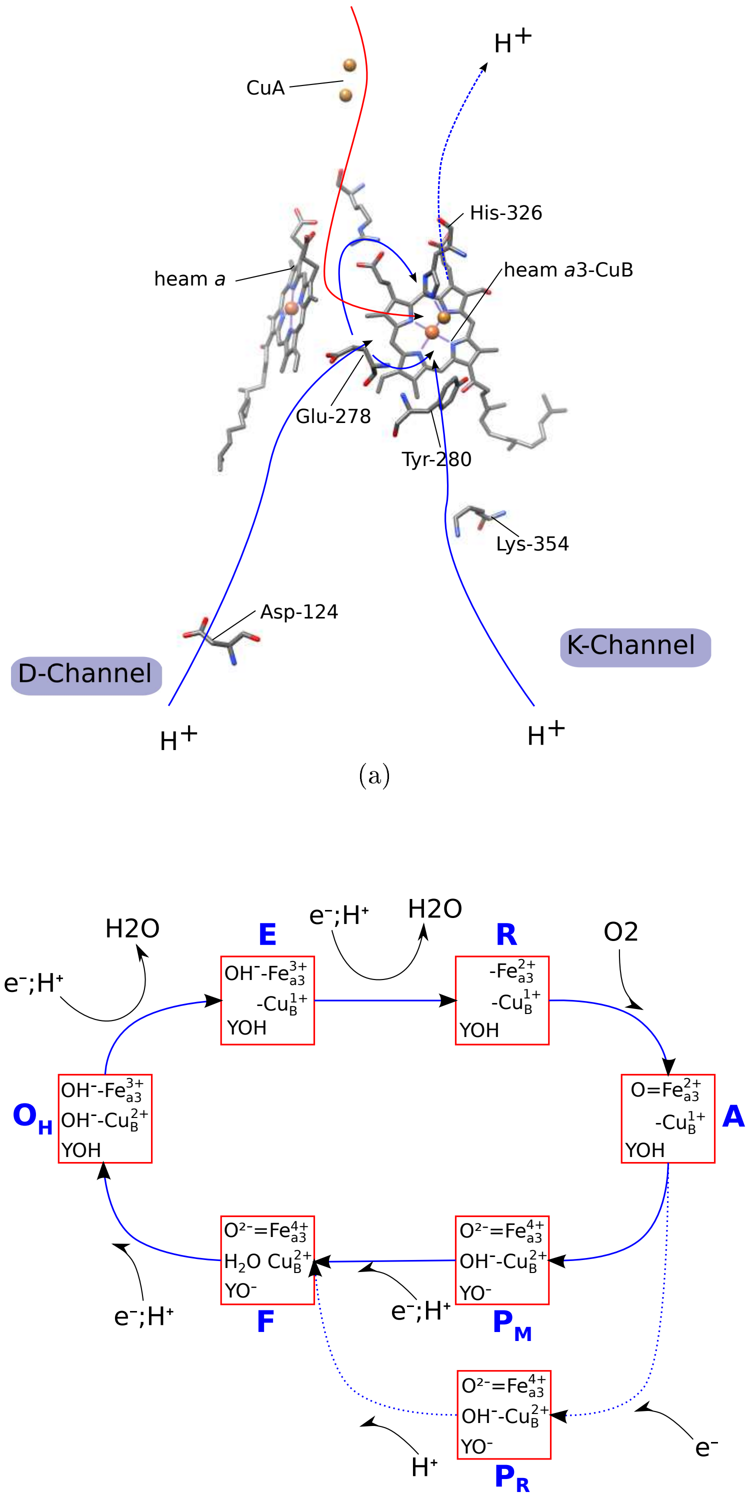

(a)

(b)

Figure 1.8: Pathways of (a) electron and proton transfer in CcO. (b) Model of the enzymatic cycle of CcO.

of two protons. One H^+ is bound to the catalytic center and the other is pumped from the N to the P-side. Transfer of an additional electron (4th electron) to the catalytic site is again coupled to the uptake of two protons and the release of one pumped proton. This process results in the formation of the fully oxidized catalytic site, denoted as O. The presence of additional reductant allow the transitions O→E and E→R and the associated proton uptake/pumping. Afterwards the enzyme returns to the fully reduced state.

The very details of the proton transfer pathway in CcO are still matter of current research. However, it was Wikstrœm who proposed the first model for the catalytic cycle of CcO [139] in 1989 and which was challenged by Michel [83] ten years later. Wikstrœm and Verkhovsky finally presented a new model for proton translocation in CcO from *P. denitrificans* [14, 140].

Two pathways exists within the CcO complex in order to direct protons from the N-side to the catalytic center. The same routes are utilized for proton pumping. The pathways are denoted as the D-channel and the K-channel. The D-channel contains water molecules providing a continuous sequence of hydrogen bonds facilitating proton diffusion by the Grotthus principle [88]. The K-channel provides two chemical protons for the reduction reaction at the catalytic site, whereas the D-channel provides both, the remaining two chemical protons and all four pumped protons per enzyme cycle. In this mechanism protons are transferred along the pathway from one hydrogen bond donor to the next hydrogen bond acceptor until they reach the next site within the channel. In contrast to what is expected, the K and the D-channel do not adopt the anticipated roles regarding the separation between pumped and chemical protons [62]. Though this is true for some part of the channel track, there seems to be a branching point at the glutamic acid Glu286. This site functions as a 'track switch'. Water molecules in the pathway from Glu286 to the pump proton acceptor and to the catalytic site determine in an alternating manner, which one of the pathways is opened and which is closed [112, 140, 143].

An additional channel denoted as the H-channel was suggested for the mammalian CcO [87, 119]. In this postulation, the H-channel is the transfer route for the pumped protons and the K and D-channels are providing the chemical protons. However, the H-channel is probably not important in the prokaryotic cell and there are speculations that the proton pumping pathways could be different for mitochondrial and bacterial CcO [132].

1.2.4 The membrane potential

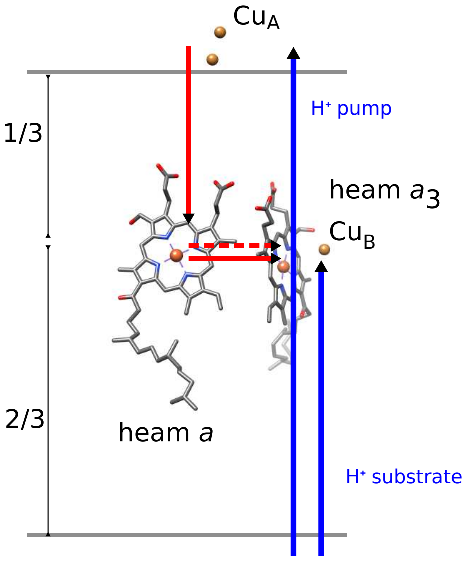

Figure 1.9: The dielectric depth of the redox sites in CcO. The vectorial charge transport is indicated as red (e-transfer) and blue (proton transfer) arrows. Only the component perpendicular to the membrane surface has an effect on $\Delta\phi_m$.

The catalytic reaction in CcO described so far is highly exorgenic. The energy released during reduction of oxygen is conserved by the enzyme in the form of a electrochemical difference ($\Delta\mu_{H+}$). $\Delta\mu_{H+}$ comprises a chemical component ΔpH, difference of proton concentration across the membrane, and a electrical component $\Delta\phi_m$, the transmembrane electrical potential difference (membrane potential). As already explained, this conserved energy is used by ATP-synthase to generate ATP. ΔpH accumulates when CcO operates in the continuous turnover regime. In the transient regime, when a single CcO turnover is measured, $\Delta\mu_{H+}$ is dominated by its electrical component $\Delta\phi_m$.

The generation of $\Delta\phi_m$ is driven by two mechanisms: the vectorial charge transport determined by the spatial distribution of the electron acceptor groups within the enzymes dielectric. The second mechanism is proton pumping. Generally, the maximum change of $\Delta\phi_m$ depends on the dielectrically weighted distance that a charge travels perpendicular to the membrane plane and to the number of the net charges transferred. Based on the catalytic model described before (Fig. 1.8b), the stoichiometry of the electrogenic charge transfer in CcO can be summarized in a system of linear differential equations (ODE) [10] of $\Delta\phi_m$ accumulated in the three main reactions steps from fully reduced to fully oxidized state with the associated rate constants $R \rightarrow O_{\mathrm{H}} \rightarrow E \rightarrow R$.

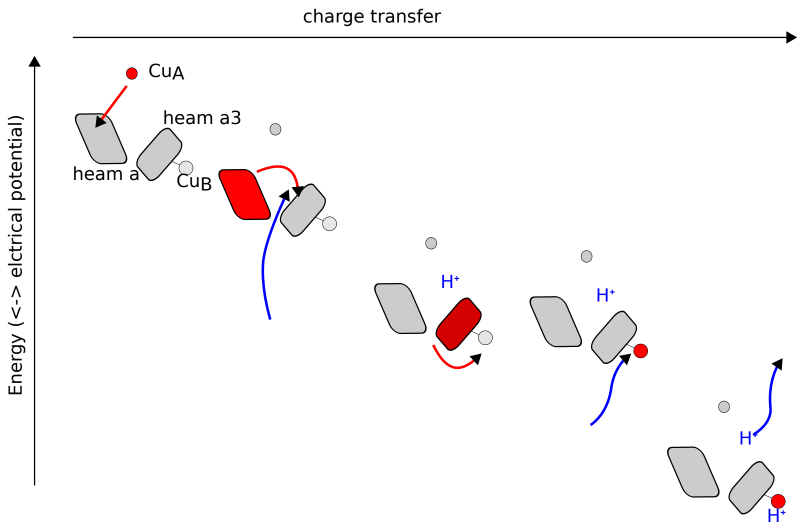

Figure 1.10: Scheme of the electrogenic charge transfer in CcO. The electron transfer is indicated with red arrows and the reduced site are red colored. Blue arrows are proton transfers. Each steps causes a change of membrane potential[8].

$$\begin{array}{rcl} \Delta\dot{\phi}_m^1 & = & Q_1\, C\, k_1\, x_1(t) - (k_2 + k_4)\Delta\phi_m^1 \\ \Delta\dot{\phi}_m^2 & = & Q_2\, C\, k_2\, x_2(t) + k_2\, \Delta\phi_m^1 - (k_3 + k_5)\Delta\phi_m^2 \\ \Delta\dot{\phi}_m^3 & = & Q_3\, C\, k_3\, x_3(t) + k_3\, \Delta\phi_m^2 - k_6\Delta\phi_m^3 \end{array} \tag{1.14}$$

This system of ODEs can be solved directly to give the time course of the transmembrane potential during a single enzyme turnover

$$\Delta\phi_m(t) = \sum_{j=1}^{3} \Delta\phi_m^j(t). \tag{1.15}$$

The parameters: $\mathrm{Q_j}$ are the equivalent dielectrically-weighted charges within a single CcO and C is the conversion factor used to translate $\mathrm{Q_j}$ into a voltage. $\mathrm{k_j}$ are the apparent rate constants (Fig. 1.11) and $\mathrm{x_j}$ the reduced concentration of R, O, E states (Fig. 1.11). The transition from the fully reduced state to the fully oxidized R->O is described by a single-exponential with $\mathrm{k_1}$ as the apparent rate constant of the reaction

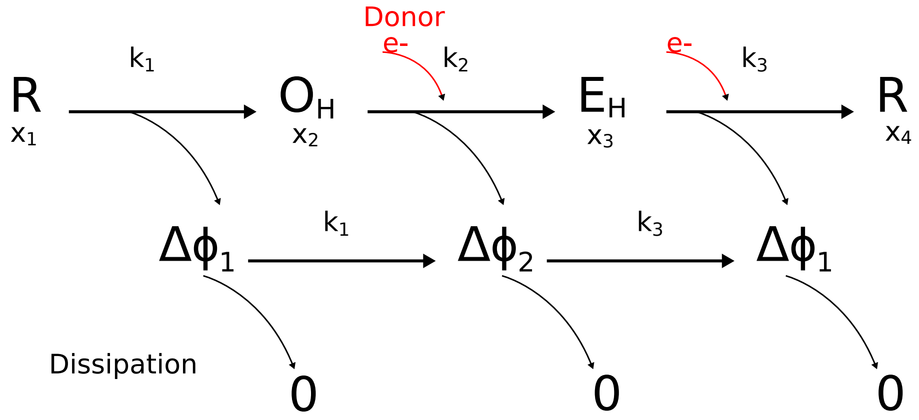

Figure 1.11: Formation and dissipation of the membrane potential shown within the kinetic scheme for the transition between the catalytic states in a single turnover of CcO. The variables are described in the text [10].

Investigation of $\Delta\phi_m(t)$ in the transient regime yields detailed information about the electron transfer process in CcO.

1.3 Aim of this Work

As described in the previous section, the self-generated membrane potential $\Delta\phi_m$ across the membrane is closely associated to the catalytic cycle of CcO. The membrane potential in a ptBLM can be measured by fluorescence spectroscopy. In order to deduce quantitative results from such investigations one has to perform calibration measurements using defined electrical potentials applied to the model membrane system. The aim of the work presented here was to perform such calibration measurements by fluorescence spectroscopy using a ptBLM with CcO. However, fluorescence techniques can not be applied on metal supports, utilized so far for the ptBLM. Strong quenching of emission light occurs if the fluorescent probe is located close (2-3 nm) to the metal surface, which is the case in the ptBLM configuration.

Consequently, the ptBLM model system has to be developed on transparent conducting substrates such as indium tin oxide (ITO). ITO enables simultaneous implementation of electrochemical and fluorescence spectroscopic techniques. The primary aim of this work was to develop the ptBLM system on ITO using *cytochrome c oxidase*. Once the model system was established, the membrane potential $\Delta\phi_m$, induced by applied external voltage could be measured.

The use of ITO as a support for the ptBLM also enables the application of other optical methods, e.g. optical waveguide spectroscopy (OWS). Using OWS, more information about the ptBLM can be derived, which would not be accessible by the techniques (SEIRAS/SERRS) applied so far on metal supports. For example, another aim of this work was to investigate the arrangement of the ptBLM on the electrode surface by multimode OWS, thereby also extending scope of interesting methods that can be applied to the ptBLM system on ITO.

One of the two strategies adopted during this work for the formation of a ptBLM on a transparent electrode was the development of a polymer support.

The idea of using macromolecules as a 'cushion' to mimic the cytosol/cytoskeleton of the cell to create a extended hydrophilic space between membrane and solid support was first introduced by Ringsdorf and Sackmann[66, 120]. Since then polymer-supported lipid membranes have been widely used, as documented in several major review articles[120, 127]. However, they were mostly applied as a model system of the cell surface rather than a model system for ion transport through proteins. The restricted applicability of such systems is due to the fact that many of these polymer-supported BLMs, as opposed to the oligo-supported tBLMs, do not fulfil the requirement known from patch clamp techniques, the giga-seal, to separate the signal of the receptor from the leak current of the membrane. Highly insulating polymer-supported membranes have been prepared, though in rare cases, a very smooth surface of the hydrophilic polymer could be achieved[47, 82]. Alternatively, specifically designed lipopolymers were employed, which were pre-oriented by the Langmuir-Blodgett technique[89, 95, 106]. However, the polymer-supported membrane having good electrical sealing properties remains a challenge.

A new approach in this direction is the use of a polymer layer as a substrate for the ptBLM developed previously on the basis of short linker molecules. Briefly, this approach employs the protein immobilized on the substrate as a scaffold for the membrane reconstituted around the protein. Consequently, the new methodology begins with immobilizing the protein specifically onto the top layer of the polymer. This can be achieved by using a hydrogel as the polymer layer with mesh sizes smaller than the size of the protein. The gel is provided with a binding motif such as a NTA functionality chelated with Ni^+ ions designed to bind the protein via the his-tag technology. Since the protein is too big to penetrate the gel, it stays on the surface. The lipid bilayer is then assembled around the protein. Electron and ion transport processes through the CcO have been observed in previous studies[35]. In the present study a hydrogel consisting of poly(N-(2-hydroxyethyl)acrylamide-co-5-acrylamido-1-carboxypentyl-iminodiacetate-co-4-benzoylphenyl methacrylate) (P(HEAAm-co-NTAAAm-co-MABP)) was prepared by polymer analogous reactions that offers a NTA moiety to bind the CcO. Optically transparent ITO layers were used as conducting substrates, different from previous studies using metal films.

Chapter 2

Theoretical Principles of the Experimental Methods

The following chapter is intended to present the theory underlying the experimental techniques that have been used for the characterization of the model membrane system at different steps of sample preparation. The fluorescence technique used to measure the membrane potential is described in chapter 4.

2.1 Electrochemistry

Electrochemical measurements are used to investigate the electrical properties of model membrane systems on planar solid supports like gold, silver or transparent conducting materials. Quantitative measurements regarding the conductivity or the capacitance of the membrane system can be performed. Such techniques also allow for the detailed investigation of electron transfer process occurring at the electrode-solution interface. During this work two methods were applied out of numerous electrochemical techniques.

Electrochemical impedance spectroscopy (EIS) was used to characterise the electrical properties of membrane systems, particularly the protein-tethered bilayer lipid membrane on ITO. Impedance and capacitance of the membrane layer after each preparation step were determined by EIS. The values were used as a control of the efficiency of each preparation step.

Electron transfer between the electrode and a surface bound redox protein were investigated by cyclic voltammetry (CV). CV is an easy and fast, qualitative or semi-quantitative method for the diagnosis of faradayic processes at the electrode surface. For example, by analyzing peak currents and peak position as a function of the scan rate electrochemical properties of redox species at the electrode surface can be evaluated.

2.1.1 The Ideally Polarizable Electrode (IPE) and the electrical double layer

Electrodes where no electron transfer can occur at the metal-solution interface are denoted as ideal Polarizable electrodes, IPEs. In reality every electrode allows charge transfer at the interface at certain potential ranges. For example, a mercury electrode in contact with a KCl solution undergoes transfer reactions at 0.25 V.

$$\mathrm{Hg^{+}Cl_{<}^{-}{=}_{>1/2}Hg_{2}Cl_{2}^{+}e}$$

However, e.g. gold in a electrolyte solution behaves like an IPE within a certain potential range. Since charges cannot be transferred across the interface an electrical double layer is formed at its surface.

The double layer is divided into three regions extending from the electrode surface to the bulk solution (Fig. 2.1). The first layer close to the surface, the inner Helmholtz plane (IHP), is formed due free charges accumulating at the electrode surface. As a consequence, a thin layer of charge compensating ions from the solution adsorb to the surface. The IHP is the closest distance $\mathrm{I_{IHP}}$ from the surface, to which the charge compensating ions approach. Excess charge in the IHP are compensated by counter ions from the solution phase, thereby forming the outer Helmholtz plane (OHP).

The Gouy-Chapman double layer, or diffuse double layer, is present if there are not sufficient ions in the outer Helmholtz plane to compensate the surface charge. In concentrated electrolytes the Gouy-Chapman layer is very thin and can usually be neglected.

2.1.2 Electrochemical Impedance Spectroscopy (EIS)

In recent years, EIS gained growing importance in the fields of biophysics and biosensor technologies. In order to explore the potential application of EIS as a transducer

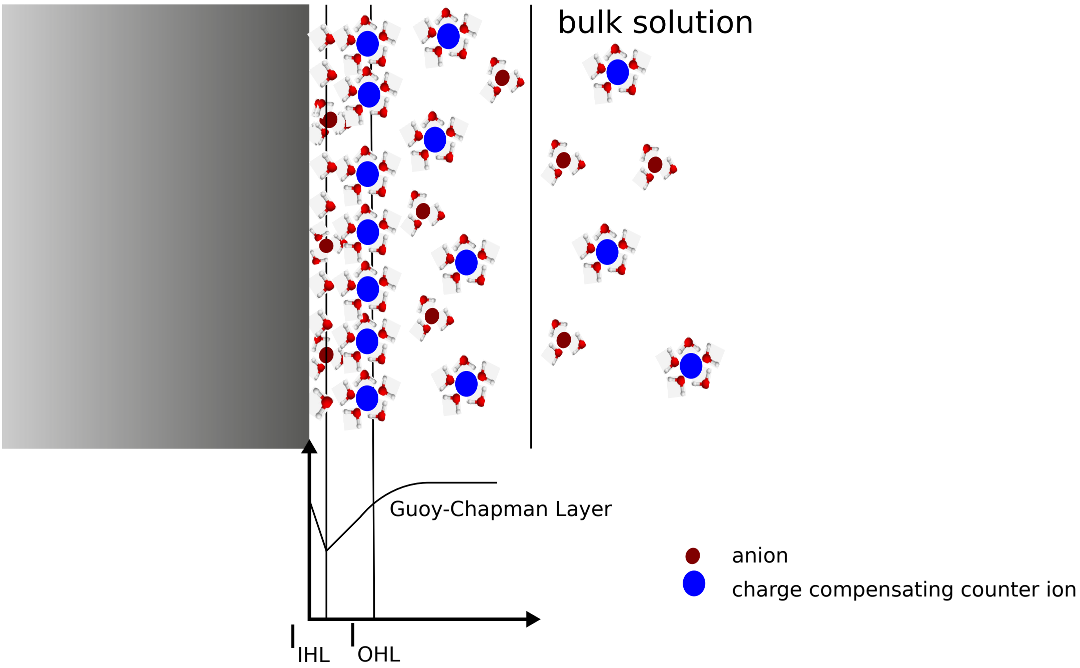

Figure 2.1: The electrochemical double layer formed at the electrode surface. The Helmholtz layer consisting of the inner Helmholtz plane (IHP), outer Helmholtz layer (OHP). The diffusive layer is usually neglected.

principle in bio-sensing devices, efforts were undertaken to develop appropriate systems. Most of these systems are composed of functional proteins (e. g. ion channels) as actual sensing elements in a lipid bilayer, that is supported by an electrode or a field-effect transistor.

A typical EIS experiment can be described as follows: The measurement is accompanied by theoretical considerations on an appropriate physical model of the studied system. An equivalent circuit (mostly consisting of capacitors and resistors) is derived from the model and is fitted to the measured spectra. This results in values for the resistors and capacitors in the circuit that describe the studied system in terms of the applied physical model. The fundamentals of EIS and the equivalent circuits are first described.

The impedance Z is the extension of the concept of classical electrical resistance in direct currents (DC) to the case of alternating currents (AC). Additionally to the 'resistance' of the circuit, Z also contains the phase shift Θ of the AC current relative to the AC voltage applied to the system. The phase shift is caused by capacitive or inductive circuit elements. In EIS, a sinusodial voltage with the amplitude E_0

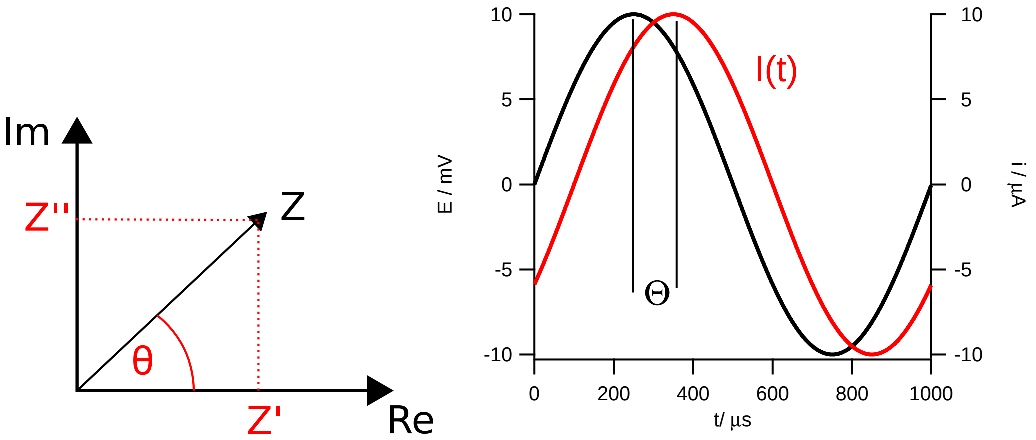

Figure 2.2: The electrical impedance presented in a polar plot (a) showing real and imaginary part of Z as well as the phase shift Θ. (b) Example of the sinusodial potential E(t) applied and the current response I(t). The phase shift is -45°.

(Fig. 2.2)

$$E_\omega(t) = E_0 \sin \omega t \tag{2.1}$$

is applied to the electrode using small amplitudes (10-25 mV) in order to avoid nonlinearities in the current response of the sample/electrode system measured at sequential frequencies ω

$$I_\omega(t) = I_0 \sin(\omega t + \Theta) \tag{2.2}$$

The data is than analyzed in terms of Z, which is defined as

$$Z(\omega) = \frac{E_\omega(t)}{I_\omega(t)} = |Z(\omega)| \exp \jmath\Theta(\omega) = Z(\omega)' + \jmath Z(\omega)'' \tag{2.3}$$

The representation of impedance data differs throughout literature. The experimental focus and the system under investigation determine the most instructive representation. Two out of a variety of representations will be shown here in a brief summary, in order to visualise the different characteristics. The aim of graphical data representation is firstly, to illustrate distinct features of the system under study and secondly, to visualise changes in these features.

In the Bode plot (Fig. 2.4) the magnitude |Z| of the impedance (logarithmic scale) and phase shift Θ of the current are plotted versus the frequency ω (logarithmic scale).

$$|Z(\omega)| = \sqrt{Z'(\omega)^2 + Z''(\omega)^2} \tag{2.4}$$

$$\Theta(\omega) = \arctan Z''(\omega)/Z'(\omega) \tag{2.5}$$

The frequency normalized Admittance plot presents the imaginary part of the Admittance against the real part, where each is normalized to ω.

$$Y(\omega)/\omega = \frac{1}{\omega Z} = Y'(\omega)/\omega + \jmath Y''(\omega)/\omega \tag{2.6}$$

For the analysis of EIS data equivalent circuit models are used in order to fit the data. From such fitting procedures one can derive the parameters of the circuit elements and, hence, the electrical parameters of the measured sample itself. The circuit elements used here are a ohmic resistor R, a capacitor C and a constant phase element (CPE). For a resistor the impedance is independent from frequency and equal to R, Z=R. The capacitive impedance is frequency dependent and is defined as

$$Z_C = \frac{\jmath}{\omega C}. \tag{2.7}$$

A CPE is used if the capacitive element of the system cannot be described by a normal capacitor. For example, surface inhomogeneities on the electrode in the microscopic scale will cause a distribution of capacitance of which the impedance can be model by a CPE as

$$Z_{CPE} = \frac{1}{(\jmath\omega)^\alpha Q}. \tag{2.8}$$

where α is the parameter between 0 and 1 representing the deviation from a normal capacitive behavior and Q a frequency independent real constant. At $\alpha = 1$ the CPE becomes a normal capacitor and Q=C. In our measurements the value of α usually was between around 0.96.

The total impedance, e.g. from the circuit introduced in Fig. 2.3 can be calculated by using equations 2.7 to 2.8 For elements in series the total impedance of an equivalent circuit is the sum of the individual impedance's and for elements in parallel the smallest

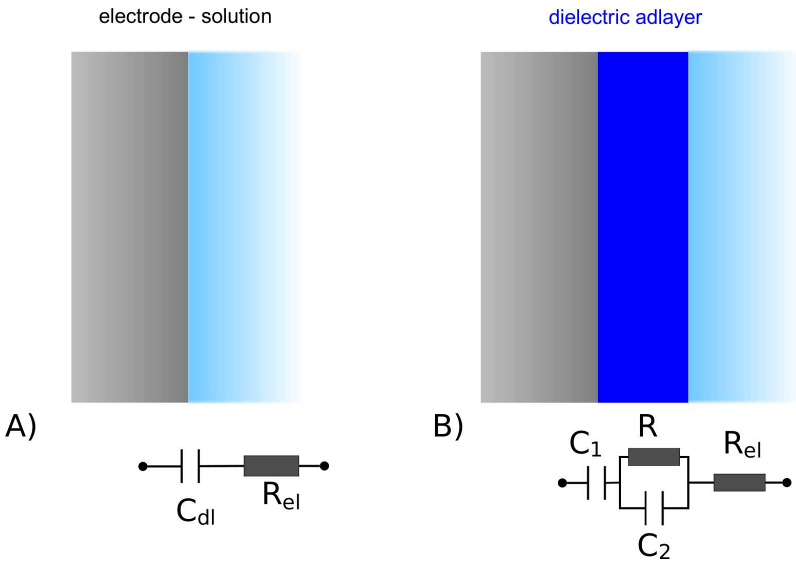

Figure 2.3: Equivalent circuits for the analysis of EIS data. (a) A bare electrode surface in contact with a electrolyte solution with resistance R_{el} forms a double layer capacitance C_{dl}. (b) A dielectric coating on the surface can be modeled by a RC circuit. The circuit capacitance is in general dominated by the coating capacitance C_2. In the low frequency range C_1, e.g. can be attributed to the spacer region (for tBLMs) or the depletion region for semi-conductor electrodes.

impedance determines Z.

$$Z_{series}(\omega) = \sum_i Z_i(\omega) \tag{2.9}$$

$$Z_{parallel}(\omega) = \sum_i \frac{1}{Z_i(\omega)} \tag{2.10}$$

The circuit elements are selected according to the physical model implied. The mathematical equation represented by the model circuit is fitted to the data in Fig. 2.4. In the case of an IPE in contact with a solution where no electron transfer occurs at the electrode-solution interface, the EIS spectra can be described by Fig. 2.3a.

The capacitance C_{dl} is attributed to the Helmholtz double layer formed at the interface. According to eq. (2.9) the smallest capacitance in a series of capacitors determines Z. For semi conductors (see next section) where the capacitance of the depletion region C_{sc}, or space charge region, can be several orders of magnitude less than the double layer capacitance, C_{dl} is substituted by C_{sc}. R_{el} is the electrolyte resistance.

If the electrode is covered by a dielectric layer permeable to ions the system can be described by a so-called RC circuit Fig. 2.3b, which is the most common circuit used to model dielectric layers like BLMs on planar electrodes. The resistor R_{el} is in series to a RC element (resistor R and capacitor C in parallel). The overall impedance of this circuit can be written as

$$Z_{RC} = R_{el} + (\jmath\omega C + \frac{1}{R})^{-1} + (\jmath\omega C_{sc})^{-1} \tag{2.11}$$

For better understanding of the mathematical fitting of the curves, a brief introduction based on the RC model is given in the following, on how to extract preliminary values from the Bode and Admittance plot. In Fig. 2.4 a typical data set for an RC equivalent circuit is presented. Phase and impedance are overlaid to allow easier interpretation and distinction of the dominating effects in the Bode plot. The impedance shows one region with a positive slope in the frequency range 0.03 Hz to 4 kHz. These regions are accompanied by a phase shift of -90°, which shows that the impedance in these frequency range is purely capacitive. In these region, the current is dominated by resistive effects, and by extrapolating through the flat region, a preliminary value for the impedance of the dielectric + electrolyte can be obtained. For resistors in

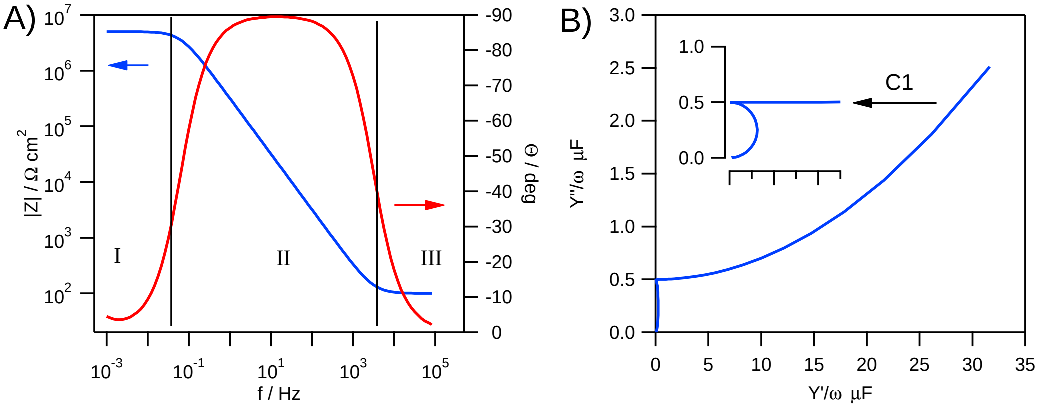

Figure 2.4: Electrochemical impedance spectra presented in the (a) Bode and (b) Admittance plot. The data was simulated using the model in Fig. 2.3b: $C=0.5\,{}^{\mu F}/_{cm^2}$, $R=5\,M\Omega\cdot cm^2$ and $[R][el]=100\,\Omega\cdot cm^2$. The Helmholtz double layer capacitance was set to $50\,{}^{\mu F}/_{cm^2}$. The spectra of an RC equivalent circuit can be divided into three distinct sections I, II and III (see text).

the circuit, the impedance is equal to the resistance, so this value directly gives an approximation of the resistances of the system under study. The high frequency resistance is usually the electrolyte resistance R_{el}. So the Bode representation gives a direct measure of the resistors under study, but no direct value for the capacitors can be inferred.

Therefore, the Admittance plot Fig. 2.4b is introduced to give information about the number and value of the capacitors in the system. This plot is not frequency dependent, as the real and imaginary parts of the admittance are frequency normalised before plotting. In the Admittance plot of Fig. **??** two semi circles are shown, each representing a capacitor. The intersection point at the imaginary axis yields a value for each capacitance of the system. In this case, where the data in Fig. 2.4 were simulated using the RC in Fig. **??**, the lower capacitance is attributed to C_1 and the higher to C_2.

If two capacitors are present in the equivalent circuit a second slope occurs (Fig. 2.5) in the Bode plot. Two spectra are drawn in Fig. 2.5, corresponding to an example of data for the formation of a tBLM. This time the circuit elements are assigned to the electrical properties of the BLM: R_m membrane resistance, C_m membrane capacitance and C_{sr} the capacitance of the spacer region formed by the tethering moities below the membrane. The capacitance of the spacer region dominates over C_{dl}. From the

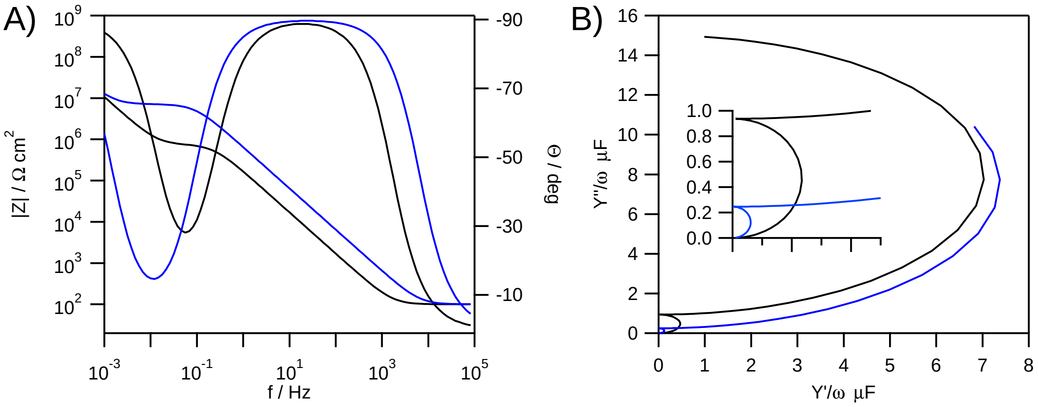

Figure 2.5: Examples of EIS spectra presented in the Bode (a) and Admittance plot (b). The spectra were simulated using literature values for a tBLM formation on a planar electrode.

position in the Bode plot it is possible to tell that the low frequency capacitance C_{sr} has a higher value than C_m showing up in the higher frequency domain. Additionally, the impedance shows a flat area with low phase angle in the high frequency domain around 0.1 Hz. Here, the example shows a 10 fold higher resistance for the bilayer compared to the spacer region.

In the Admittance plot, the first (spacer region) and last (bilayer) data set are presented, each showing two semi-circles. The first semi- circle is intersecting the y-axis at 1 µF for the the spacer region, the second at 0.25 µF for the bilayer (inset in Fig. 2.5b). Thus, this values can be directly assigned to the spacer region and bilayer respectively. For the bilayer, the second semi-circle is not completed, but an extrapolation towards the y-axis shows that this capacitance remains the same as for the spacer region, as it intersects at the same value attributed to C_{sr}. In this special case, the values obtained from the plots Fig. 2.5 are exactly the values used for the simulation. In reality, this procedure gives a first approximation of the values before the fit and the preliminary values are used as starting parameters likewise.

The elements for equivalent circuits have to be selected by considering the structure and the dominating electrical effects of the system. As there are many possibilities of assembling model circuits and many more elements than simple resistors and capacitors that can mimic effects of natural non-ideal systems, the variety of interpretation of the EIS data is huge. However, the careless assembly of equivalent circuits with many elements often results in misinterpretation.

As many minor processes contribute to the systems response that can not be discriminated by the analysis, the model might not perfectly fit the spectra in all points. On the other hand, the characteristics of a more complex model, especially when composed from a large number of elements, are rarely unique. Consequently, a simple model should be preferred over a too complicated one, to get reproducible effects and more reliable results. Only the simplest circuit can be said to be unambiguous in its description of the experimental data.

2.1.3 Cyclic voltammetry

Cyclic voltammetry (CV) is a electrochemical method for the analysis of surface bound or freely diffusing redox species. It enables fast quantitative analysis of electrode processes. From CV measurements one can provide insight into the thermodynamics and kinetics of redox processes. The redox peaks in the CV curves usually appear at very well defined potentials which can readily be evaluated to give detailed information about the properties of redox systems.

In a CV experiment a linearly changing potential is applied to the working electrode. The direction of the linear scan is switched to the negative slope at a certain time or a defined switching potential E_1. A complete CV sweep is accomplished when the starting potential has been reached after a second switching at E_2. The current flowing through the system is recorded during the potential scan. A typical CV scan is presented in Fig. 2.6.

The current measured during the CV scan originates from Faradayic and Non-Faradayic processes.

Non-Faradayic currents result form the reorganization of ions at the electrode-solution interface and are also denoted as capacitive currents I_C. If the potential waveform is described by a triangular shape $E = E_{start} \pm \nu_{scan} t$ where ν_{scan} is the scan rate and E_{start} the starting potential, then the current can be written as

$$I_C = E_{start}/R_e \cdot \exp -t \cdot C/R_e + \nu \cdot C(1 - \exp -t \cdot C/R_S) \tag{2.12}$$

and R_e is the electrolyte resistance. The difference in I_C between backward and forward sweep is $I_C = 2\nu C$.

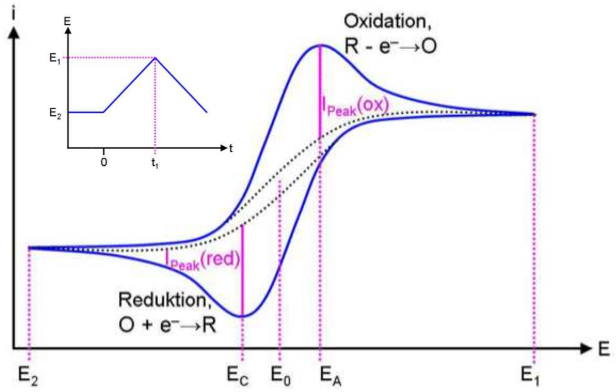

Figure 2.6: A typical cyclic voltammogram showing a fully reversible electron transfer process: E_C cathodic and E_A anodic peak potential. E_1, E_2 switching potentials, E^0 redox potential. The applied potential in CV has a triangular waveform (inset). Picture from [57].

Faradayic currents originate from heterogeneous electron transfer at the electrode-solution interface

$$O + e^- \rightleftharpoons R \tag{2.13}$$

The form of the CV scan is thereby determined by the mass transport to and from the electrode and the heterogeneous electron transfer at the electrode itself. The later is described by the fundamental equation from the electrochemical kinetics theory, the Butler-Volmer equation

$$j_A(0,t) = c_O(0,t)k^0 \exp\{-\alpha nF/RT(E-E^0)\} - c_R(0,t)k^0 \exp\{-(1-\alpha)nF/RT(E-E^0)\} \tag{2.14}$$

the parameters are; k^0 standard rate constant, α transfer coefficient, E^0 formal potential and $C_R(0,t)$,$C_O(0,t)$ the concentration of reduced and oxidized species at the electrode-solution interface respectively. $C_R(0,t)$,$C_O(0,t)$ are different than C_R,C_O in the bulk solution leading to a diffusion controlled mass transport which is described by Ficks law of diffusion, which in turn causes a current

$$j_A(0,t) = -D_{R,O}(\frac{\partial C_{R,O}}{\partial x})_{x=0} \tag{2.15}$$

If the heterogeneous electron transfer is fast in terms of k^0 (>0.1 cm/s), an equilibrium is reached at the phase boundary and the process is denoted as reversible electron transfer, eq. (2.14) simplifies then to the Nernst equation

$$E = E^0 + \frac{RT}{nF} \ln \frac{C_O}{C_R} \tag{2.16}$$

and the surface concentrations $C_R(0,t)$,$C_O(0,t)$ dependent only on the applied potential E. The position of the redox peaks become independent from the scan rate and the peak separation is constant $\Delta E = |E_A - E_C| = \frac{59}{n} mV$.

2.2 Ellipsometry

Ellipsometry is based on the detection of the change of the polarization state of light reflected from a surface. This technique is well-known for the measurement of the optical constants and the thickness of thin films on various substrate materials like Si, Ge, GaAs, or metallic and polymeric layers. By theory, the sensitivity of ellipsometric techniques can go down to angstrœms. Therefore it is often applied *in-situ* in the field of material science of soft matters, e.g. to study monolayers of biological complexes or the characterization of surface functionalization methods.

Though the whole potential was not utilized throughout the experiments, ellipsometry was employed in order to measure thickness and the refractive index of thin functional layers on a transparent substrate. Moreover, protein immobilization was followed by kinetic ellipsometry. A brief introduction into the fundamentals of ellipsometry measurements and the optical modelling of the data are given here.

Polarized Light in Ellipsometry. The temporal and spatial evolution of an electromagnetic wave is described mathematically by the wave equation derived from the Maxwell equations. According to the standard physics convention a useful solution is presented by an orthogonal set of monochromatic plane waves propagating along the z-axis

$$\vec{E}(t) = Re\left\{ \begin{pmatrix} E_x \\ E_y \end{pmatrix} \exp \jmath (k_z z - \omega t) \right\} \tag{2.17}$$

with the dispersion relation $k_z = \frac{\omega}{c}\sqrt{\epsilon}$. The plane waves solution can be rewritten into a more convenient form by choosing the z=0 base of the coordinate system to describe the polarization state of the light (Fig. 2.7). For elliptic polarized light eq.

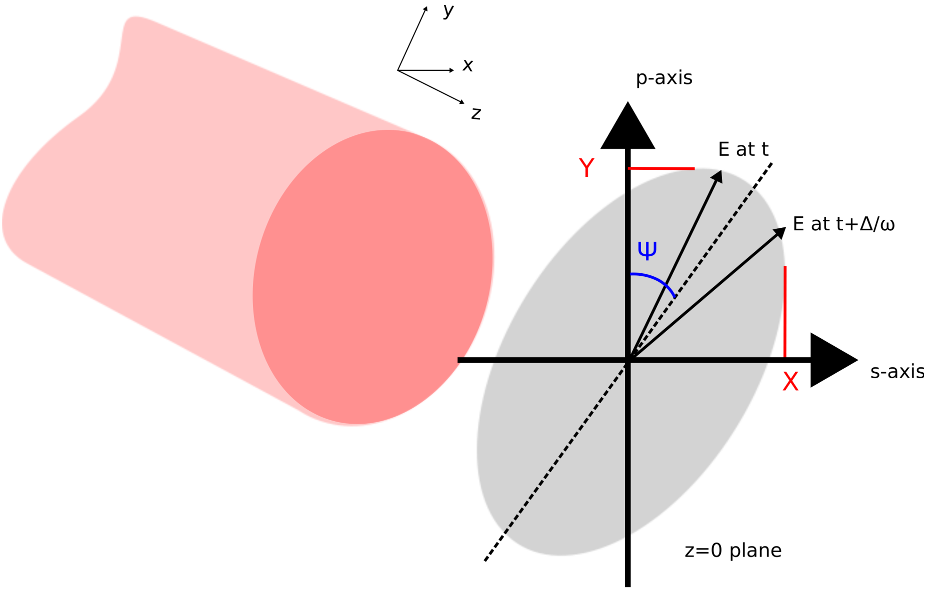

Figure 2.7: Polarization ellipse described by the ellipsometric parameters Δ and Ψ. The propagation of the light is in z-direction.

2.17 becomes than

$$\vec{E}(t) = Re\left\{\begin{pmatrix} Xe^{\jmath\Delta} \\ Y \end{pmatrix} \exp -\jmath\omega t\right\}. \tag{2.18}$$

Two parameters are introduced here in order to describe the ellipsometric data: if the ps-coordinate system is chosen, i.e. p-axis is parallel and the s-axis is perpendicular to the incident plane (Fig. 2.8), than Ψ becomes the ratio of the absolute amplitudes X and Y which can be defined in the usual way by

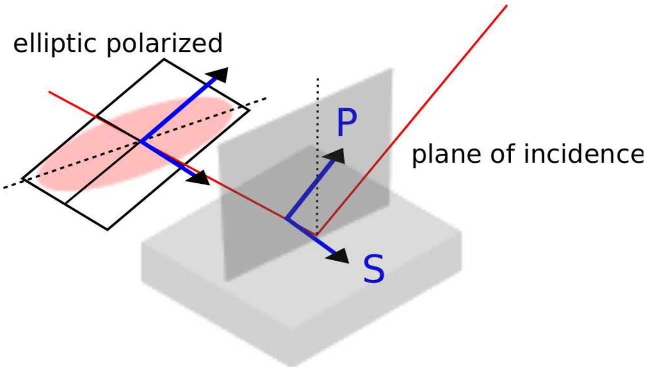

Figure 2.8: Schematics of the p-s-coordinate system and the polarization plane of elliptic polarized light reflected from a surface.

$$\tan\Psi = \frac{X}{Y}. \tag{2.19}$$

The parameter Δ describes the phase difference between the x and the y-oscillations of the electric field. When the light is reflected from the sample at an incident angle θ the polarization state described by these parameters is changed. In the experiment Δ and Ψ have to be related to the material constants of the sample, which can be readily done for isotropic materials by the ellipsometric parameter ρ

$$\rho = \frac{R_p}{R_s} = \tan\Psi e^{\jmath\Delta}. \tag{2.20}$$

R_p and R_s are the Fresnel reflection coefficients for the p and s-polarization respectively. The aim of an ellipsometry measurement is to determine the change of Δ and Ψ upon reflection from the sample surface. The reflection coefficients are derived through the Transfer Matrix Method. For the general case, given by a stack of thin films on a substrate in ambient air, the reflection coefficients can be derived from the matrix multiplication (Fig. 2.9)

$$M_s = \chi_{s,air}\left(\prod_{j=1}^{N} T_{j,s}\right)\chi_{s,sub}, \qquad M_p = \chi_{p,air}\left(\prod_{j=1}^{N} T_{j,p}\right)\chi_{p,sub} \tag{2.21}$$

where χ_{air}, χ_{sub} are characteristic matrices in p and s for the ambient and the substrate[1, pp.247]. The products in the braces describe the alteration of the reflected and transmitted light beam at each interface of the layer stack and $T_{j,s}$, $T_{j,s}$ are the corresponding Transfer Matrices in p and s-polarization according to the Abelés

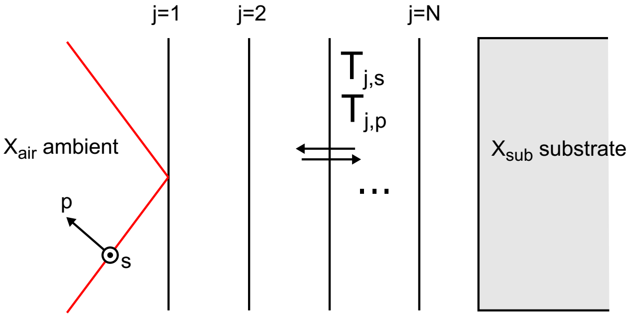

Figure 2.9: Schematics of a light beam reflected from a stack of N layers. The transfer matrix relates reflected field amplitude from one layer to the field amplitude in adjacent layers.

method

$$T_{j,s} = \begin{pmatrix} 1 & -\jmath\frac{\cos\theta_j}{\tilde{n}_j}b_j \\ \jmath\frac{\tilde{n}_j}{\cos\theta_j}b_j & 1 \end{pmatrix}, \quad T_{j,p} = \begin{pmatrix} 1 & \jmath\frac{\tilde{n}_j}{\cos\theta_j}b_j \\ \jmath\tilde{n}_j\cos\theta_j b_j & 1 \end{pmatrix} \tag{2.22}$$

The parameters are as following: $b_j = \frac{2\pi d}{\lambda}\tilde{n}_j\cos\theta_j$ is the phase factor, θ_j is the incident angle at the jth interface, $n_j = n_j - \jmath\kappa_j$ the complex refractive index of the jth layer. The relation 2.22 is only valid for very thin films, $d \ll \lambda$, i.e. the film thickness d is smaller than the wavelength λ of the incident light, The reflection coefficients in 2.20 than can be calculated from the matrices in 2.21 through their matrix elements

$$R_p = \frac{M_{21,p}}{M_{11,p}} \qquad R_s = \frac{M_{21,s}}{M_{11,s}}. \tag{2.23}$$

Using an appropriate layer model refractive index and film thickness can be derived employing one of the various nonlinear fitting methods, e.g. the Levenberg-Marquardt algorithm. Most of the automatic ellipsometry systems commercially available today offer a built in data analysis framework, where the layer model is fitted to the raw data (Δ, Ψ) on the basis of (ñ,d) of the layer investigated.

PCSA Ellipsometer. Different ellipsometer setups exist in order to investigate thin layers on various substrates. Here, the polarizer-rotating compensator-sample-analyzer configuration (PCSA) will be described. The same configuration was also used during this work.

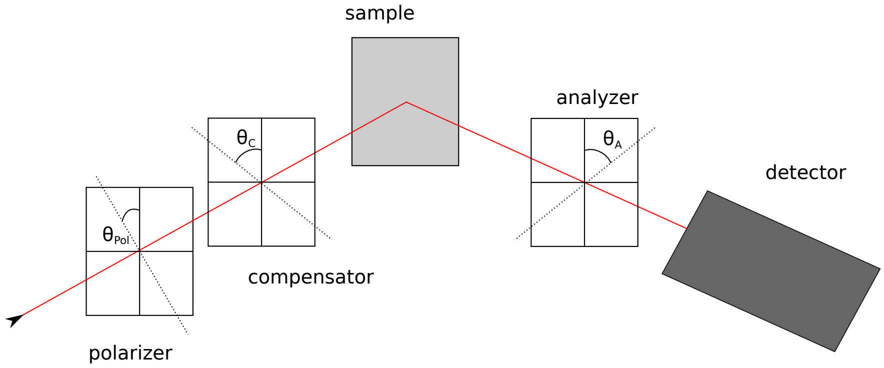

Figure 2.10: The polarizer-rotating compensator-sample-analyzer configuration of an ellipsometer.

In the PCSA scheme the light beam goes through the polarizer P in first place

(Fig. 2.10). Note that the transmittance of the polarizer to unpolarized or elliptical polarized light is independent of the azimuth θ_{Pol} of the polarizer. The wave reaches the compensator with a defined polarization state expressed in the complex amplitude E_P. The azimuth of the compensator is θ_C. The wave incident on the compensator is than a superposition of the components along the fast $E_{Pol}\cos(\theta_{Pol} - \theta_C)$ and the slow axes $E_{Pol}\sin(\theta_{Pol} - \theta_C)$ of the compensator (Fig. 2.10) so that the transmitted amplitude becomes

$$E_{fast} = E_{Pol}\cos(\theta_{Pol} - \theta_C), \qquad E_{slow} = E_{Pol}\sin(\theta_{Pol} - \theta_C) \tag{2.24}$$

and t_{fast}, t_{slow} are the complex transmission coefficients of the compensator along the fast and the slow axis respectively. In order to describe the wave reflected from the surface, it is convenient to apply a transformation from the fast-slow axis of the compensator to the ps-coordinates of the incident plane. Using 2.24 the amplitudes E_{rp}, E_{rs} of the reflected wave than can be written as

$$\begin{pmatrix} E_{rp} \\ E_{rs} \end{pmatrix} = \begin{pmatrix} R_p \\ R_s \end{pmatrix} \begin{pmatrix} \cos\theta_C & \sin\theta_C \\ -\sin\theta_C & \cos\theta_C \end{pmatrix} \begin{pmatrix} E_{fast} \\ E_{slow} \end{pmatrix}. \tag{2.25}$$

After passing the analyzer the field amplitude at the detector is determined by the field amplitude E_A along the direction of the azimuth θ_A of the analyzer

$$\begin{aligned} \begin{pmatrix} E_A \\ 0 \end{pmatrix} &= \begin{pmatrix} T \\ 0 \end{pmatrix} \begin{pmatrix} \cos\theta_A & -\sin\theta_A \\ \sin\theta_A & \cos\theta_A \end{pmatrix} \begin{pmatrix} E_{rp} \\ E_{rs} \end{pmatrix} \\ E_A &= E_{rp}\cos\theta_A + E_{rs}\sin\theta_A \end{aligned} \tag{2.26}$$

where T is the complex transmittance of the analyzer and usually close to 1, which leads to 2.26. The intensity detected is proportional to $|E_A|^2$.

The so-called 'Null Ellipsometry' allows a fairly simple determination of the ellipsometric parameters (Δ, Ψ) using the PCSA configuration. The term 'Null' ref errs to the aim to extinguish the light at the detector by finding the right settings of polarizer, compensator and analyzer, thus setting E_A=0 in eq. 2.26. Using eq. 2.20 and

2.24-2.26 one than obtains

$$\rho = \frac{\tau_C \tan(\theta'_{Pol} - \theta'_C) + \tan\theta'_C}{\tan(\theta'_{Pol} - \theta'_C)\tan\theta'_C - 1} \tan\theta'_A \tag{2.27}$$

where $\tau_C = \frac{t_{slow}}{t_{fast}} = \tan\Psi_C e^{\jmath\Delta_C}$ is the transmission coefficient ratio for the compensator defined similarly to the reflection coefficient ratio of the sample in eq. 2.20. The azimuths $\theta'_{Pol}, \theta'_C, \theta'_A$ are the particular settings of the components where E_A=0. A very simple scheme can be employed if a quarter wave is utilized as a compensator. In this case, where $\tau_c = \jmath$, the compensator is set to a constant azimuth $\theta_C = \pi/4$ and the equations are further simplified. The E_A=0 condition yields two sets of solutions $\theta^1_{Pol}, \theta^1_A$ and $\theta^2_{Pol}, \theta^2_A$ which are related to each other by $\theta^2_{Pol} = \pm\theta^1_{Pol}$ and $\theta^2_A = -\theta^1_A$. The ellipsometric parameters can be derived from this solutions using eq. 2.27 and 2.20

$$\Psi = \theta^1_A, \qquad \Delta = 2\theta^1_{Pol} + \pi/2. \tag{2.28}$$

In automatic ellipsometry setups the software tends to find the intensity minima at the detector by varying the azimuth of polarizer and analyzer. This procedure is performed at an compensator azimuth set to $\pi/4$ and is repeated with the compensator at $-\pi/4$. The measured (Δ, Ψ) pairs are fitted using the equations 2.23 for R_p,R_s.

2.3 Optical Waveguide Spectroscopy

Planar integrated optical waveguides have been widely used in a variety of experimental configurations for optical characterization of organic thin films. OWS is similar to surface plasmon resonance spectroscopy, which is another label-free technique that has been widely used for measuring optical parameters of thin films on noble metal surfaces. SPR as well as OWS have been employed extensively for studies of model bio-interfaces, e.g. monitoring binding of protein complexes to functionalized surfaces. In terms of instrumental design, both methods are identical and essentially practiced in two distinct modes:

1. angular mode: a thin dielectric layer on on the surface changes the boundary conditions of the propagating mode at the metal/dielectric interface and, hence the angle at which the optical modes are excited (resonance angle). This shift of the resonant angle can be detected by varying the angle of incidence of a

monochromatic light beam to the sample and detecting the intensity of the reflected light. This is also the mode used during this work employing the Kretschmann configuration (see below).

2. spectral mode: the resonant wavelength at which the optical modes are excited is monitored using a polychromatic light source incident at a fixed angle.

One eminent advantage of OWS compared to SPR is that, depending on the design of the waveguide, multiple optical modes denoted as $\mathrm{TM_m}$ (p polarized) and $\mathrm{TE_m}$ (s polarized) can be excited. Consequently, more than one optical parameter of the thin film layer can be determined from one experiment. For example, if the layer has an anisotropic index OWS allows the probing of different components of the dielectric tensor.

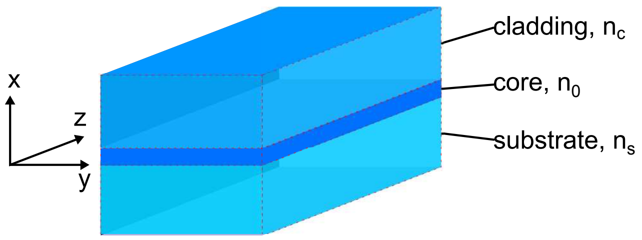

Figure 2.11: Slab optical waveguide.

The propagation constants of the guided modes can be derived from wave optics. The derivation of the dispersion equation only for the TE modes will be described, since the approach for TM modes is analog. The plane-wave solution of the Maxwell equations for wave propagation in a planar waveguide is used. The slab optical waveguide is depicted in Fig. 2.11. Considering y-symmetry of the equations, $\partial\vec{E}_y/\partial y = 0$, $\partial\vec{H}_y/\partial y = 0$, the TE mode propagating in the slab then satisfies the following equations including the wave equation

$$\frac{d^2E_y}{dx^2} + (k^2n^2 - \beta^2)E_y = 0 \tag{2.29}$$

$$H_x = -\frac{\beta}{\omega\mu_0}E_y \tag{2.30}$$

$$H_z = \jmath\frac{1}{\omega\mu_0}\frac{dE_y}{dx} \tag{2.31}$$

$$E_z = E_x = H_y = 0. \tag{2.32}$$

with k,ω,μ_0 and n as the usual parameters. β and κ are the propagation constants in z and x-direction respectively. They are expressed by

$$\beta = kn_0 \cos\theta \tag{2.33}$$

$$\kappa = kn_0 \sin\theta \tag{2.34}$$

where n_0 is the refractive index of the core and θ the inclination angle of the propagating wave. For a uniform refractive index profile in the core of the slab waveguide (Fig. 2.12), as well as the cladding and substrate, one gets solutions of the wave equation (2.29) in the three dielectrica of the slab

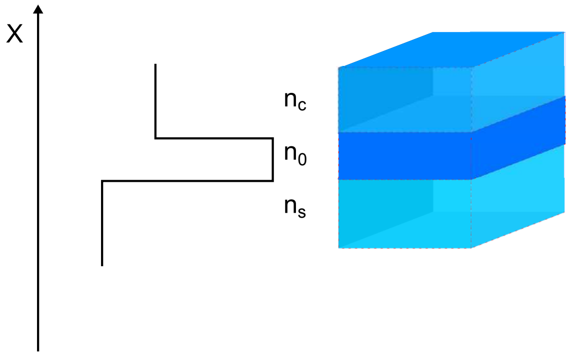

Figure 2.12: Refractive index profile across the slab in the x-direction.

$$E_y = \begin{cases} A\cos(-\kappa a - \theta)e^{-\sigma(x-a)} & x > a, \text{ cladding} \\ A\cos(-\kappa x - \theta) & -a \leq x \leq a, \text{ core} \\ A\cos(-\kappa a + \theta)e^{-\xi(x+a)} & x > a, \text{ substrate} \end{cases} \tag{2.35}$$

d=2a is defined as the thickness of the waveguide. As can be seen from E_y for the substrate and the cladding, the fields outside the core should be exponentially decaying within the cladding and the substrate in order to confine most of the light energy in the core. κ, σ and ξ are the wave numbers along the x-axis of the cladding, core and substrate respectively

$$\kappa = \sqrt{k^2 n_c^2 - \beta^2} \tag{2.36}$$

$$\sigma = \sqrt{\beta^2 - k^2 n_0^2} \tag{2.37}$$

$$\xi = \sqrt{\beta^2 - k^2 n_s^2} \tag{2.38}$$

If exponentially decaying fields outside the core are required, then β and κ need to be real, consequently the solution should satisfy following condition

$$n_s \leq \frac{\beta}{k} \leq n_c \tag{2.39}$$

where β/k is a dimensionless value relating the wave velocity in a vacuum to that in the waveguide, hence, playing the role of a refractive index. In literature it is often denoted as the effective refractive index $\mathrm{N_{eff}}=\beta/k$. $\mathrm{N_{eff}}$ will also be the parameter measured during some experiments in this work.

Finally, the continuity condition for $\mathrm{E_y}$ and $\mathrm{H_z}$ leads to the eigenvalue equations

$$u = \frac{m\pi}{2} + \frac{1}{2}\tan^{-1}(\frac{w}{u}) + \frac{1}{2}\tan^{-1}(\frac{v}{u}) \tag{2.40}$$

$$\theta = \frac{m\pi}{2} + \frac{1}{2}\tan^{-1}(\frac{w}{u}) - \frac{1}{2}\tan^{-1}(\frac{v}{u}) \tag{2.41}$$

where new wave numbers are introduced: $\mathrm{u}=\kappa\mathrm{a}$, $\mathrm{w}=\xi\mathrm{a}$ and $\mathrm{v}=\sigma\mathrm{a}$. Solving the eigenvalue problem gives θ and with it the propagation constant β, which in turn yields $\mathrm{N_{eff}}$. Graphical or numerical methods can be employed in order to solve (2.40) which will not be discussed here. More importantly, the value of $\mathrm{N_{eff}}$ changes significantly if a thin ad-layer is adsorbed in the cladding region of a slab, or in generally speaking, if the optical constants in the cladding are changed. In this respect, OWS is a very sensitive method for the investigation of thin ad-layer on the waveguide. In the following it will be explained, how the change of $\mathrm{N_{eff}}$ can be detected using the Kretschman configuration for the OWS measurements.

Kretschmann Configuration In order to be able to excite waveguide modes one has to realize the resonant condition where exciting light and waveguide mode are in phase. In general, this can also be described as following: for efficiently coupling a light wave from one medium to another two conditions have to be met. First, the wave velocities in the two media must be the same and, second, the length along the coupled boundary must be adjusted according to the strength of the coupling. One way to meet the first criterion, the phase-matching, is to use a prism as illustrated in Fig. 2.13a. The second condition can be met easily by adjusting the prism base on the waveguide. The z-component $\mathrm{k_z}$ of the wave vector $\vec{k}_{ph}$ of the incident wave at the prism base will be $k_x = k_{ph} n_p \sin\phi$ with $\mathrm{n_p}$ as the refractive index of the prism and ϕ

the angle of incidence at the prism-waveguide boundary. The z-component of the m*th* waveguide mode has been denoted as the propagation constant β_m before. This two wave numbers have to match in order to satisfy the first condition, leading to

$$\beta_m = kn_p \sin\phi_m \tag{2.42}$$

and therefore to $\mathrm{N_{m,eff}}$. For ϕ above the critical angle, an evanescent field with an exponential decay into the direction of the waveguide exist at the prism base. Upon phase-matching, light energy from the incident wave is continuously fed into the waveguide. The intensity of the light reflected from the prism base will decrease. If ϕ is adjusted continuously while measuring the reflectance from the prism base the curve will show several sharp minima, which can be assigned to the excited waveguide modes (Fig. 2.13b). The angles ϕ_m at the minima are the resonance angle for the m*th* mode. ϕ_m will shift if the optical constants of the layer adjacent to the waveguide change. As already mentioned, this shift allows the determination of the optical constant and thickness of the ad-layer investigated. Therefore, the reflectance data are fitted on the basis of a multi-layer model. In the experiments presented here, the Fresnel equations were used for fitting in order to derive $\mathrm{N_{m,eff}}$ for a ptBLM on an ITO waveguide. A thin gold layer was introduced between the base of the prism and the waveguide layer. The metal layer was thin enough (40 nm) in order to avoid the complete damping of

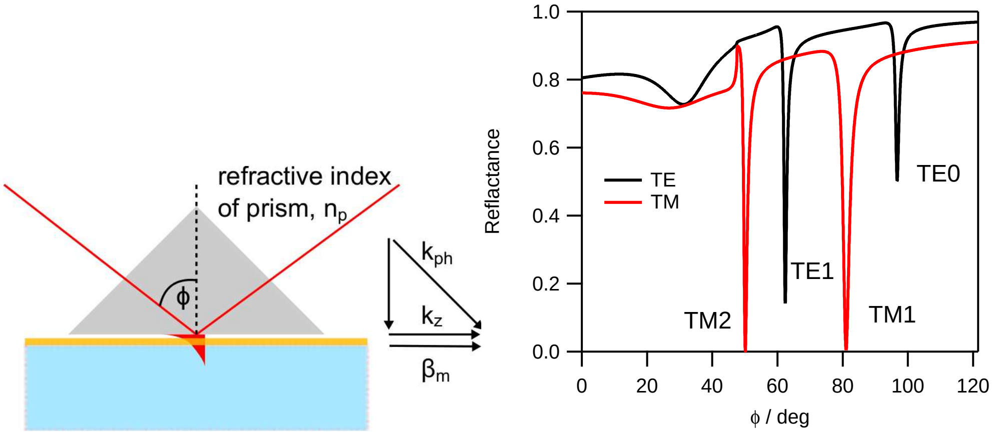

(a) (b)

Figure 2.13: The Kretschmann configuration for the excitation of optical waveguide modes through a thin gold layer.

the evanescent field at the prism base. Two purposes were served by the metal film

1. coupling of the harmonic wave through the metal film to the waveguide modes. A neat description of this phenomena can be served by quantum mechanics. The solution of the Schrödinger equation is the same as the solution presented above. It describes an evanescent wave at the prism base and an oscillating wave between prism and waveguide (leaky-mode)[122, 129]. The gold layer can be treated as a potential wall of finite height and width. This gives rise to the reflection by anti-tunneling and the coupling into and out of the waveguide by tunneling. The coupling efficiency (depth of the minima in the reflectance data) depends than on the width of the potential wall, or in other words the thickness of the gold layer.

2. the waveguide core is sandwiched by two layers of lower refractive index. This satisfies (2.39) for a bound optical mode in the waveguide core.

Chapter 3

Development of a Membrane Model System on Transparent Substrates

The self-generated potential difference $\Delta\phi_m$ across the membrane is closely associated to the catalytic cycle of CcO. $\Delta\phi_m$ generated by CcO can be measured by fluorescence spectroscopy. As already elucidated in section 1.3, in order to be able to perform calibration measurements by fluorescence spectroscopic techniques, a transparent conductor has to be utilized as a substrate, since fluorescence spectroscopy is not applicable on metal supports due to the strong quenching of emission light.

Therefore, a ptBLM model system has to be developed on transparent conducting substrates such as indium tin oxide (ITO). ITO enables simultaneous implementation of electrochemical and optical methods such as fluorescence spectroscopy and optical waveguide spectroscopy (OWS).

The formation of ptBLMs on ultra smooth metal films had been described previously [2, 33, 38]. According to this procedure the gold or silver surface was modified using a sulfur functionality bearing active ester (DTSP), followed by coupling with N-(5-Amino-1-carboxypentyl) imino-diacetic acid (ANTA) and complexation with Ni^{2+} ions. The protein was bound to the surface thus prepared via a 6xHis-tag, attached to one of the subunits. Subsequently, a lipid bilayer was formed around the protein by in-situ dialysis.

An equivalent procedure had to be established for oxidic surfaces such as ITO or silicon dioxide. For this purpose the oxidic surfaces were functionalized by silanization with silane molecules designed for ANTA coupling. Alternatively, a polymer layer was prepared on the silanized surface, provided with active ester functionality also designed for ANTA coupling.

Both strategies were applied in this work. In the first instance the binding and reconstitution of CcO on silanized silicon wafer will be described. Silicon wafer surfaces consist of a naturaly grown silicon dioxide layer. This system offers a proper platform to verify and test the ptBLM on silanized semiconducting surfaces. Then the ptBLM on silanized ITO will be introduced before the ptBLM on hydrogel coated ITO will be presented.

3.1 Protein-tethered BLM on Silicon Wafer

Due to its very low roughness the silicon wafer is an ideal model of an oxidic surface. For the immobilization and re-constitution of CcO p-doped Si was chosen as a substrate. The surface consisted of a naturally grown SiO_2 layer which usually had a thickness of 2 nm. After silanization and ANTA coupling the protein was adsorbed to the surface and re-constituted into a lipid bilayer membrane.

3.1.1 Self-assembly of the NHS-Silane monolayer

It is well known that many parameters determine the properties of a silane monolayer deposited by self-assembly from liquid phase: the surface coverage of hydroxyl groups determined by the pretreatment of the surface, the molar ratio of water to silane in the solution, the incubation time and the temperature[28]. Concerning the first factor, pretreatment of the surface by hydroxylation, different procedures were already applied. A very common way is to use fresh piranha solution based on sulfuric acid or ammonium hydroxide. Using Ar^+ plasma is an alternative way. Plasma cleaning, as will be shown here, does deteriorate the silicon surface and thereby increases the surface roughness, which also is a crucial point for silanization. Monolayer on surfaces with increased roughness are less defined and have a reduced reproducibility[17]. To examine the effect of Ar^+ plasma cleaning silicon samples were treated for 10 min in a plasma cleaner with 10:1 $Ar^+_/O_2$ pressure ratio. AFM scans before and after treatment were recorded and compared. The RMS value increased slightly from 0.14 nm for a clean untreated surface to 0.16 nm for the plasma treated surface. Hence, to avoid

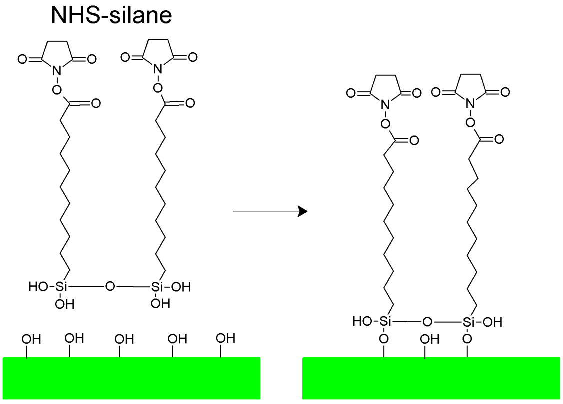

Figure 3.1: NHS-silane structure and binding to the oxide surface of a silicon wafer pretreated using piranha solution.

increase of surface roughness the hydroxylation of the silicon surface was carried out using fresh piranha solution based on sulfuric acid.

The second parameter that has an effect on the silanization was the relative water content. For trialkylsilanes it is generally accepted that a small water content is necessary for the monolayer formation. Excess water amount, however, results in fast polymerization and deposition of polysiloxane onto the surface. Triethoxysilanes are more stable to polymerization. Yet higher water amounts do still lead to polymer deposition. In the present work NHS-silane (Fig. 3.1) was dissolved in desiccated THF having a water content of approximately 0.005 % v/v. To assure that the water content did not change the solvent bottle was stored under a glove box. Incubation was also performed in the glove box. Under this conditions, assuming that this way the water content of 0.005 % in THF was stable, the molar ratio of water to silane was controlled by using different silane concentrations.

In order to find the best conditions for the silanization of the SiO_2 surface, the silane concentration was varied between 0.1 %, 0.2 % and 1 % w/w. Prior to incubation the samples were cleaned using piranha solution followed by thorough rinsing using DI water. The incubation time was 1 h. After self-assembly the samples were cleaned by sonication in THF. For each concentration the NHS-silane layer was analyzed by means of ellipsometry, atomic force microscopy (AFM) and contact angle measurements. Ellipsometry and contact angle data are summarized in Tab. 3.1 and Tab. 3.2. For the evaluation of the ellipsometry data the refractive index n of the silane was set to n=1.46, assuming the silane forms a homogeneous monolayer on the surface. This

Medium	d of SiO_2 layer in nm	contact angle
Air	1.35	26°
Water	1.14	-
PBS	0.9	-
PBS/DDM	1.06	-
Air (after piranha)	2.13	<10°

Table 3.1: Thickness d of the SiO_2 layer in different media. The thickness are results of a least squares fit to the layer model based on the Fresnel equations. The refractive indices of Water, PBS, PBS/DDM are 1.33.

conc. of silane in THF	incubation time			
c_{silane}/ % (w/w)	30 min	1 h	overnight	3 days
0.1	-	-	-	-
0.2	0.71	0.73	0.9	0.9
1	1.1	1.55	2	2.1

Table 3.2: Change of thickness in nm after deposition of NHS-silane by self-assembly under different conditions. The thickness change in was measured by ellipsometry in air. A silicon substrate coated with a silane/SiO_2 hybrid layer having an effective refractive index of n=1.46 was assumed as a layer model. The values were obtained from least squares fits to the data based on Fresnel equations.

refractive index corresponds to that of the silicon dioxide surface. Therefore, in the fitting model, oxide and silane layer were considered as a single ad-layer on a p-doped amorphous silicon substrate (n=4.86 nm). To verify the parameter setting, like refractive index of the oxide surface, the thickness of the oxide layer in different media was determined prior to silanization. The thickness of the oxide layer before cleaning measured in air was approximately 1.3 nm and did not vary significantly from this value over different samples. The contact angle prior to cleaning was at 26°. In PBS, DDM/PBS and Ni-solution the thickness decreased slightly to 1.1 nm. After cleaning of the bare oxide surface using piranha solution, which also hydroxylated the surface for further modification, the thickness of the oxide layer increased to approximately 2.1 nm in all media. A contact angle below 10° verified the hdrophilicity of the surface. Silanization increased the thickness to 3.5 nm for 1 % silane solution and 2.9 nm for 0.2 %. The contact angle also increased to 75°. Using a 0.1 % solution of silane did not show any significant thickness change and the contact angle usually was approximately 46°.

To compare the surface topography under the respective silanization conditions the AFM images of a 1x1 µm area were recorded. The location of the area was chosen randomly. For each silanization condition three different spots on the surface were scanned and compared for location to location variations. Over an area of 1 cm^2 the recorded pictures usually showed similar surface profiles. The height profile was analyzed regarding the surface roughness and the average "peak-valley" height referred to as the Z-range value. A bare silicon surface after piranha cleaning was scanned as a reference (Fig. 3.2a). The RMS value showed an average of 0.1 nm and Z-range was 1.1 nm. After silanization at 0.1 %, 0.2 % and 1 % the samples were sonicated in THF, blown dry using nitrogen and immediately scanned. For silane concentration of 0.1 % no significant difference in surface morphology compared to a bare silicon surface could be detected. The RMS value was 0.1 nm and the Z-range 0.7 nm. The single spike that is clearly seen in Fig. 3.2c has a peak height of 12.6 nm. Using a concentration of 0.2 % increased RMS to 0.2 nm and Z-range to 3.7 nm. In Fig. 3.2e a noticeable number of spikes appear. However, their average height measured from the lowest point in the same scan line was only 2 nm. The spikes can be interpreted as polymerized NHS-silane. A low silane concentration relative to water causes all three ethoxy groups (Fig. 3.1) being hydrolyzed which results in facile polymerization. At concentrations of 1 % hydrolysis of all ethoxy groups is reduced due to a low water/silane ratio. Hence, silane chains are formed and deposited on the surface instead of aggregates formed by polymerized NHS-silane. This can be clearly seen in Fig. 3.2g where the AFM picture shows that the surface is homogeneous and free of silane aggregates. The features that were present before almost vanished. Thickness measurements by ellipsometry also prove the compactness of the monolayer having a thickness of 2 nm, a contact angle of 75° supports this conclusion. The RMS value was 0.2 nm and Z-range was 1.6 nm.

As already mentioned in the beginning, other than the two parameters of silanization that have been described yet, which are the pretreatment of the surface and the molar ratio of water to silane, the incubation time and the temperature also influence the formation of the monolayer. The values for both parameters that were used in previous works vary over a wide range. Often, it was found that depending on the exact properties of the silane, incubation at approximately 28 ℃ for i. e. several days gave reproducible results[5, 15]. Whereas in other reports monolayer formation was accomplished within minutes to hours. In the present work, silanization was performed under the stabilized atmosphere of a glove box. A temperature of 22 ℃ was maintained during incubation. The silane concentration used was 1 % w/w. The incubation time was varied between 30 min, 1 h, overnight and 3 days. Ellipsometry measurements showed that silane coverage of the surface reached saturation after 24 h (Tab. 3.2). The contact angle reached a maximum value of approximately 75°. Using an incubation time up to 1 h resulted in a thickness change of 1.5 nm. If the samples were incubated overnight the thickness increased by 2 nm. An attempt was made to use even longer silanization times ranging from overnight to several days. The thickness did not increase further. AFM scans recorded for varying incubation times are not shown here, since the scans do not differ significantly from Fig. 3.2g.

In summary, using a silane concentration of 0.1 % ellipsometry and contact angle data indicate a very low or no functionalization of the silicon surface with NHS-silane. AFM scans also reveal that the surface roughness did not change in comparison to a bare silicon surface. Instead NHS-silane aggregates appeared having a height of approximately 12 nm. The best results in terms of thickness measured by ellipsometry and contact angle measurements were achieved using a silane concentration of 1 %. If the sample was incubated overnight or longer in a 1 % solution the results were even better. In that case the thickness of the silane layer was found to be 2.1 nm. AFM scans of respective surfaces show that the roughness in RMS decreased significantly

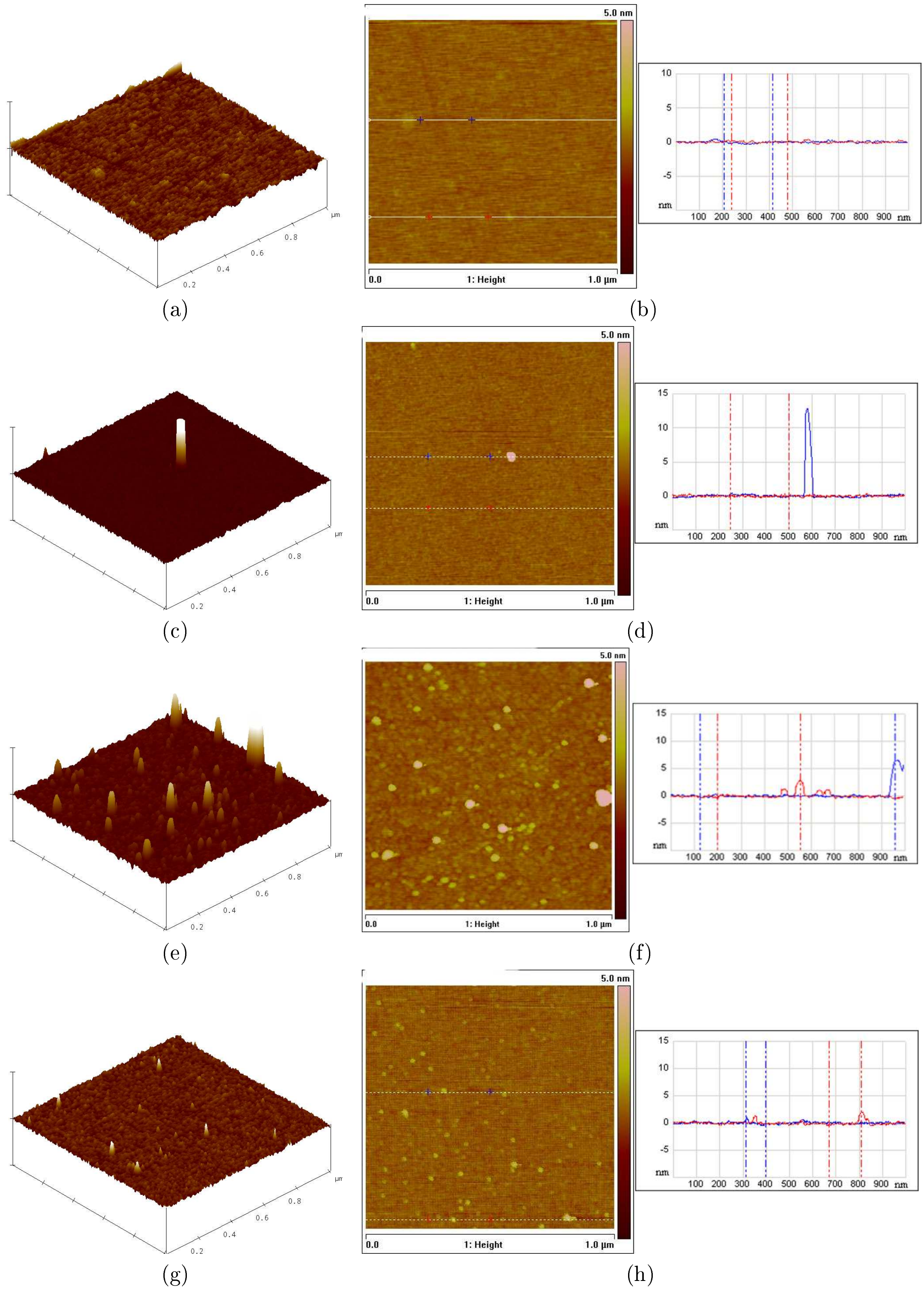

(a) (b)

(c) (d)

(e) (f)

(g) (h)

Figure 3.2: AFM pictures of the NHS-silane modified silicon surface. The 3d profiles (left) and the linescans (right) of three different concentrations are shown. For comparison the picture of a bare silicon surface (a) was included. The concentrations used were 0.1 % (c), 0.2 % (e) and 1 % (g) of NHS-silane in THF.

with concentration. Here again the lowest roughness of the surface in terms of RMS and Z-range values were achieved using a concentration of 1 % w/w NHS-silane.

3.1.2 Functionalization of the silanized Si surface and binding of CcO measured by ellipsometry

The thickness of the CcO layer bound to functionalized silicon surface was measured by ellipsometry. Therefore, the samples were first silanized using the optimized silanization parameters presented in the previous section: the slides were incubated in a 1 % NHS-silane solution in dessicated THF for one day. After silanization the samples were incubated ex-situ in a aqueous solution of ANTA for two days. Covalent coupling of ANTA to the monolayer is realized through the formation of an amide bond between the amine group of ANTA and the NHS-silane. The coupling reaction is schematically shown in Fig. 3.3. The samples were than rinsed using DI water and the flow cell was assembled. A $NiSO_4$ solution in acetate buffer was filled into the cell. The Ni^{2+} ions in the solution form a complex with the NTA head group of ANTA by coordinating to the free COOH groups. To remove excess Ni the cell was flushed using nickel free acetate buffer and DI water. The sample surface had to be treated using DDM/PBS in order to avoid protein denaturation at contact with the surface. Therefore, a small amount of DDM/PBS was filled into the cell prior to CcO adsorption. Finally CcO dissolved in DDM/PBS was introduced. CcO has a poly-histidine group attached to the C-terminus of SU I. The histidine group coordinates to the Ni-NTA chelate and forms a stable complex, thereby anchoring the enzyme to the surface (Fig. 3.3).

To follow the adsorption of CcO on the surface the change of the ellipsometry parameters Δ and ψ as a function of time was measured (Fig. 3.4). Right in the beginning of the measurement a jump in both parameters can be observed. This coincides with the moment of CcO injection. After CcO injection the parameters change continuously during CcO adsorption before they reach a saturation level after 2 h. The most significant change occurs within the first 30 min, where Δ changes approximately from 176° to 173° and ψ changes from 18.5° to 18.6°. The final values after carefully flushing the cell with DDM/PBS were 176.1° for Δ and 18.6° for ψ.

The thickness of the protein layer can be derived from the ellipsometry data. Therefore the data has to be simulated in terms of a two layer model, using the oxide/silane/ANTA layer as a single sublayer. The refractive index and the thickness

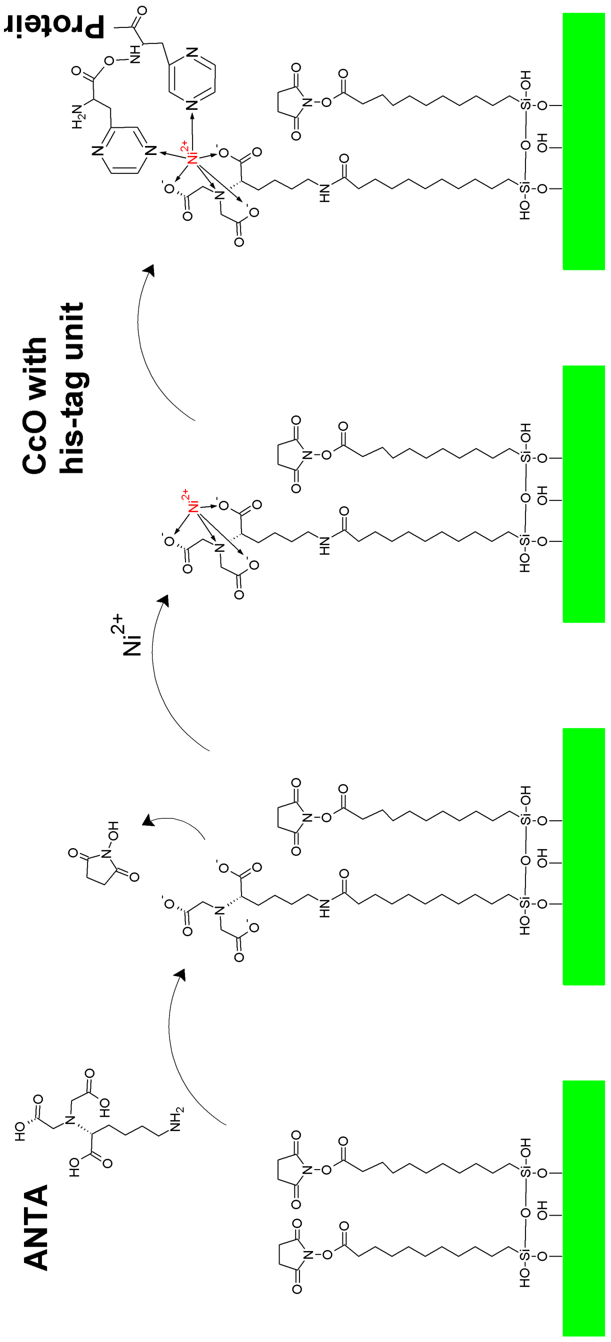

Figure 3.3: Schematic depiction of the ANTA coupling reaction and Ni^{2+} complexation on NHS-silane functionalized silicon wafer.

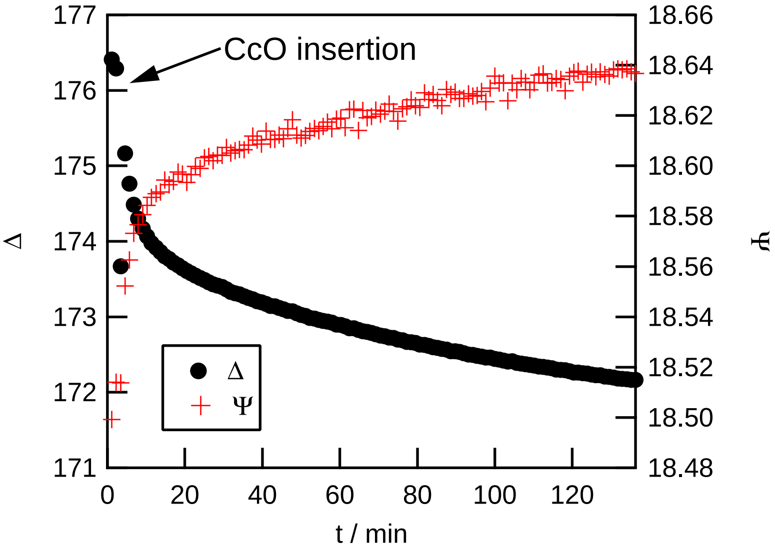

Figure 3.4: CcO binding on silicon surface followed by ellipsometry. The AOI was fixed at 60° and the wavelength was 532 nm. Time of injection of CcO is indicated in the graph. The change of Δ and ψ indicates adsorption of CcO.

of the sublayer are 1.46 and 3 nm respectively. The ellipsometry parameters Δ and ψ measured as a function of time reflect not only the thickness change of the ad-layer but also the change of the its refractive index. Thus, to derive the final thickness of the protein layer only the values of Δ and ψ before CcO insertion and after final flushing using DDM/PBS were taken. A refractive index of 1.45 was assumed for the CcO layer. This way a thickness of approximately 6 nm was calculated. The thickness calculated from the length of CcO at 100 % coverage, along the axis of orientation on the surface, is 9 nm [61]. From this result it can deduced that the surface coverage of CcO tethered to a SiO_2 surface is 66 %.

3.1.3 Formation of the ptBLM on Si wafer by EIS

The binding of CcO measured by ellipsometry was described in previous section. In order to initiate the formation of a lipid bilayer around the tethered CcO the phosphocholine lipid DiPhyPC solubilized in DDM/PBS was added to the bulk solution. The detergens molecules around CcO were replaced with lipids by *in-situ* dialysis using bio-beads leading to the formation of BLM patches between the proteins. CcO

preparation step	C_m in $\mu F/cm^2$	R_m in $M\,\Omega{\cdot}cm^2$
After Ni	-	-
After CcO binding	7	0.2-5
After in situ dialysis	3-5	5.4-13

Table 3.3: Change of capacitance C_m and resistance R_m of the ptBLM on silicon at different steps of the preparation. The data was normalized to the area of the working electrode which is 0.28 cm². The values are ranges measured for 10 different silicon samples.

binding and BLM formation were monitored by impedance spectroscopy.

The impedance spectra were recorded using a three electrode configuration where the p-doped silicon wafer was the working electrode, a Ag–AgCl (saturated KCl) the reference and a platinum wire the counter electrode. The equivalent circuit Fig. 3.5, used to evaluate the impedance spectra, consisted of three RC circuits Fig. 3.5 in series with the electrolyte resistance R_e. Instead of pure capacitors, constant phase elements were used because of the heterogeneous property of the underlying system. The space charge region of the semiconducting silicon was accounted for by $R_{sc}C_{sc}$. The circuit $R_{sr}C_{sr}$ represents the silane/NTA sublayer referred to as the spacer region. In the last RC circuit R_m,C_m is the membrane/protein resistance and the membrane/protein capacitance respectively. The NTA activated surface without CcO was evaluated using a double RC circuit, in which R_m,C_m was omitted. The results were derived from a nonlinear least squares fit to the normalized spectra. The results of the fittings are summarized in Tab. 3.3.

Before adsorption of CcO on the complexed monolayer a spectra had been recorded as a reference. From the example of a impedance spectra in Fig. 3.5 it can be seen that the resistance of the oxide/silane/ANTA sublayer is already in the range of $2M\,\Omega{\cdot}cm^2$ and has a low capacitance of approximately $10\,\mu F/cm^2$. This was attributed to the thin oxide layer between the tethered moieties and the silicon bulk. In section 3.1.1 the thickness of the oxide layer was shown to be 2 nm after treatment using piranha solution. The layer acts as an electrical barrier interface. After binding of CcO to the surface the resistance increases to $5M\,\Omega{\cdot}cm^2$ and the capacitance decreases slightly to a minimum of $7\,\mu F/cm^2$. The values changed again after removal of the detergent using bio-beads. The resistance increased to $13M\,\Omega{\cdot}cm^2$ and the capacitance reached a minimum value of $5\,\mu F/cm^2$. The value ranges of resistance and capacitance derived

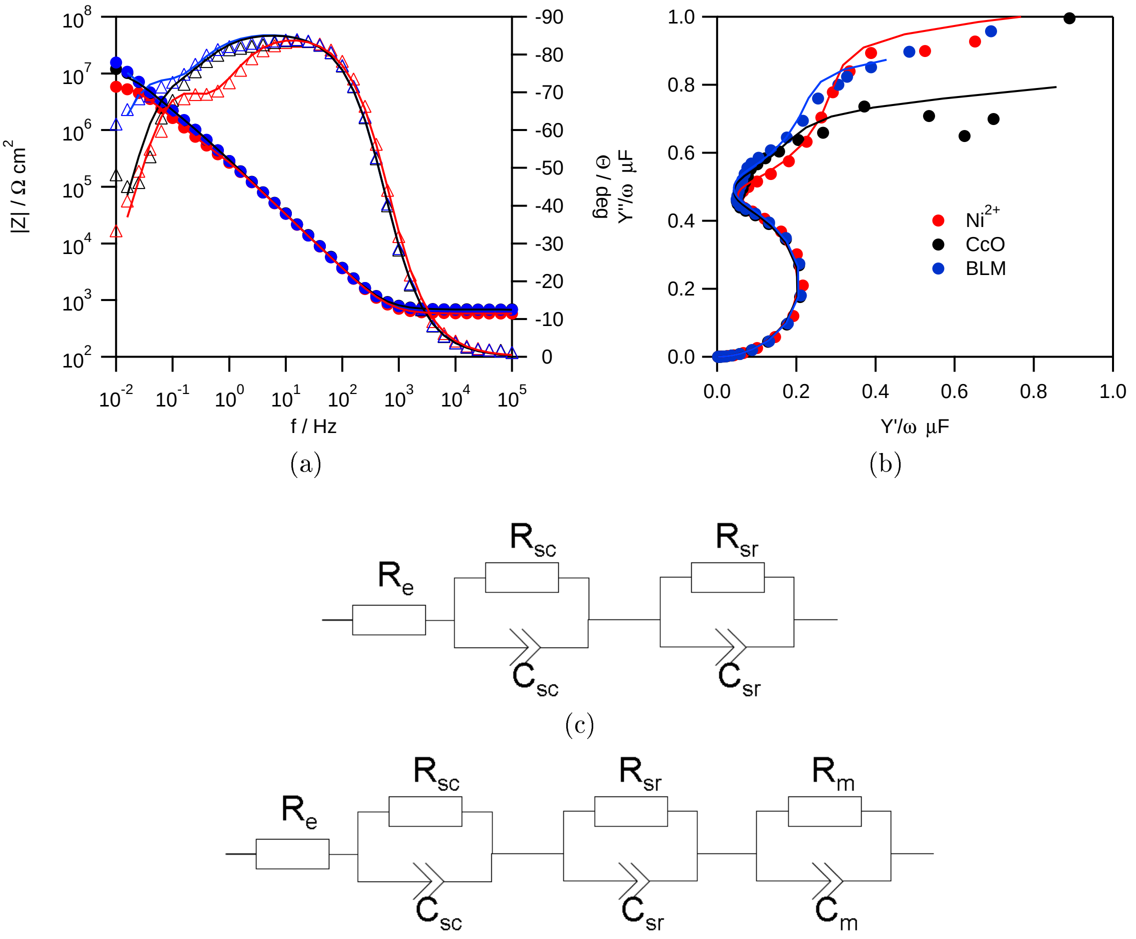

(a) (b)

(c)

(d)

Figure 3.5: Bode (a) and Admittance (b) plot of the impedance spectra measured at different steps of the ptBLM formation on silicon. Before CcO binding (red); after CcO binding (black) and after in situ dialysis using bio-beads (blue). Equivalent circuit (c) was used to calculate the fits (solid lines) before CcO binding and (d) after CcO binding and BLM formation. The circuit elements in sequence: R_e electrolyte resistance; R_{sc},C_{sc} space charge region of the p-doped silicon; R_{sr},C_{sr} sub-membrane space consisting of the oxide layer, silane, ANTA; R_m,C_m the CcO/lipid membrane layer.

from impedance spectra of 10 silicon samples are presented in Tab. 3.3.

This finding indicates the formation of a ptBLM on silicon. The theoretical value of capacitance and resistance for a pure lipid bilayer is $0.2\,{}^{\mu\mathrm{F}}/_{\mathrm{cm}^2}$ and $>1\mathrm{M}\,\Omega{\cdot}\mathrm{cm}^2$ respectively. The capacitance measured here is higher but still in accordance to the CcO surface coverage derived in the previous section. There it was shown that the coverage must be approximately 60 %. Accordingly the amount of lipid in the ptBLM bilayer is much lower compared to a pure lipid bilayer. Assuming a bilayer thickness of 5 nm and a dielectric constant of 30 for CcO and 2 for the lipids the capacitance for the ptBLM is then expected to be around $4\,{}^{\mu\mathrm{F}}/_{\mathrm{cm}^2}$ which is close to the measured value of $5\,{}^{\mu\mathrm{F}}/_{\mathrm{cm}^2}$.

3.2 Tethered BLMs on ITO

The binding of CcO and formation of a BLM around CcO on silicon were shown. Here an analog procedure will be applied to build a ptBLM on ITO, which is a transparent semiconductor. First the deposition and characterization of the ITO layer will be described. Then a tethered BLM on ITO will be shown. This system offers a adequate platform to test formation of lipid bilayers on ITO. Finally a ptBLM on ITO is presented.

3.2.1 Preparation of the ITO layer

The ITO layers were prepared by DC sputtering on glass slides. The aim was to achieve good optical and electrochemical properties of the layer, whereby the surface should have a low surface roughness. Prior to deposition the slides were cleaned using piranha solution. Sputtering was performed under varying conditions regarding process pressure $\mathrm{P_b}$ and argon/oxygen ratios. The DC power was set to a constant value of $2.2\,{}^{\mathrm{W}}/_{\mathrm{cm}^2}$. The slides were always prepared on the same day and numbered according to their sequence of deposition. After deposition using different parameter sets the sheet resistance $\mathrm{R_s}$ was measured by a four-point probe method[123]. The deposition time usually was 10-15 min and the layer thickness, measured by step-profiler and ellipsometry (n of ITO 1.9065) was 80-120 nm.

Deposition was performed in a sequence within the same day. The $\mathrm{R_s}$ of the corresponding day were compared. For the first sequence (sample 1-3 in Tab. 3.4) the

sample	O_2 / % vol.	P_b / Pa	R_s / Ω/sq
1	0	0.6	2k-2.5k
2	5	0.6	250k-500k
3	10	0.3	35-85
4	2	1	250-700
5	1	1	250
6	0	1	15-25

Table 3.4: ITO layer properties after sputtering at varying chamber pressure P_b and oxygen volume concentration. The samples are numbered according to the deposition sequence within the same day. The DC power density was set to a constant value of $2.2\,{}^{W}/_{cm^2}$. The layer thickness was 80-120 nm. For samples 1-3 the ITO target was pre-sputtered for 15 min at P_b=0.3 Pa using pure argon, and for samples 4-6 at P_b=1 Pa using 1 % vol oxygen. The resistivity R_s was measured by the four-point method.

target was pre-sputtered using pure argon. The process pressure P_b was decreased from 0.6 Pa to 0.3 Pa and the relative oxygen content was increased stepwise from 0 % to 10 %. R_s decreased thereby from 2k Ω/sq up to 35 Ω/sq. In the second sequence (sample 4-6 in Tab. 3.4) the target was pre-oxidized before deposition using a P_b of 1 Pa and 1 % vol oxygen. During deposition P_b was kept constant at 1 Pa for all three samples. In the beginning a small amount of oxygen was used. In that case R_s did not change much from 250 Ω/sq. For the last sample oxygen was omitted leading to a sheet resistance of 15 Ω/sq.

From this data it can be clearly seen that the electrical properties of the ITO layer depend on the state of the target before deposition. The target condition changes with sputtering time. To explain this behavior it is appropriate to use the terms of 'non-oxidized' and 'oxidized' state of the target[67]. In the beginning, the first set of three samples in Tab. 3.4, only argon had been used for pre-sputtering. Thereby the target was brought into the non-oxidized state leading to a brownish color of the layer and high resistivity values of 2k-2.5k Ω/sq. A low oxygen content is known to reduce transparency and conductivity[54, 72] of DC and RF sputtered ITO layers, whereas a high oxygen content still gives good transparency but decreased conductivity. Low oxygen concentrations reduce the grain boundary scattering due to larger grain sizes. Hence charge carrier mobility is increased. If the oxygen concentration is increased further the carrier mobility decreases again, which is attributed to the trapping effect of neutral $(SnO_2)_2$ clusters. Therefore, for samples 2 and 3 oxygen was added with increasing partial pressure. This lead to decreasing resistance where the best result in terms of R_s were realized using 10 % vol of oxygen. Though sputtering had been started from an non-oxidized target, using oxygen flow during deposition seems to re-oxidized the target thereby bringing it close to the optimal oxidization state. In the second sequence of samples this effect has been simulated by pre-sputtering the target without samples in the chamber. The conditions used for pre-sputtering were a process pressure P_b of 1 Pa and 10 % vol. oxygen. The sheet resistance got much lower compared to sputtering with a non-oxidized target. After the first two samples in the second set (sample 4 to 6), where an $Ar-O_2$ mix had been used, the target reached the optimal oxidized state. Starting deposition from this state resulted in the best values with R_s even close to 35 Ω/sq.

It can be concluded that after installation of the ITO target before deposition, pre-oxidization of the target using a $Ar-O_2$ mix is necessary. This way good electrical and optical properties of the layer can be achieved. To test this assumption a new series was produced starting from a non-oxidized target and using a higher oxygen amount for pre-sputtering. This time the target was pre-sputtered for 15 min using 10 % vol. oxygen at 1 Pa process pressure. Thereafter, only argon was used for deposition. As expected, R_s had a reproducible value of 15-35 Ω/sq.

3.2.2 ITO surface characterization

The ITO surface was characterized in terms of electrochemical properties and surface roughness. The surface morphology was recorded by AFM. To verify that no large scale inhomogeneities exist, different surface areas of 1x1 µm size were scanned in tapping mode. The location of these areas was within a section of 1 cm^2 in the center of the sample. No significant differences in surface morphology could be observed. Therefore, it was assumed that a single scan of a randomly chosen surface area from the center of the sample was representative for a 1 cm^2 section of the ITO layer.

All of the layers scanned by AFM featured a surface pattern formed by small spikes having a diameter of 15-20 nm. From AFM measurements of various samples it was also evident that the surface roughness of the layer did change when the chamber process pressure and relative oxygen content were varied. The most significant difference shown in Fig. 3.6 appeared between the first sample deposited at a process pressure

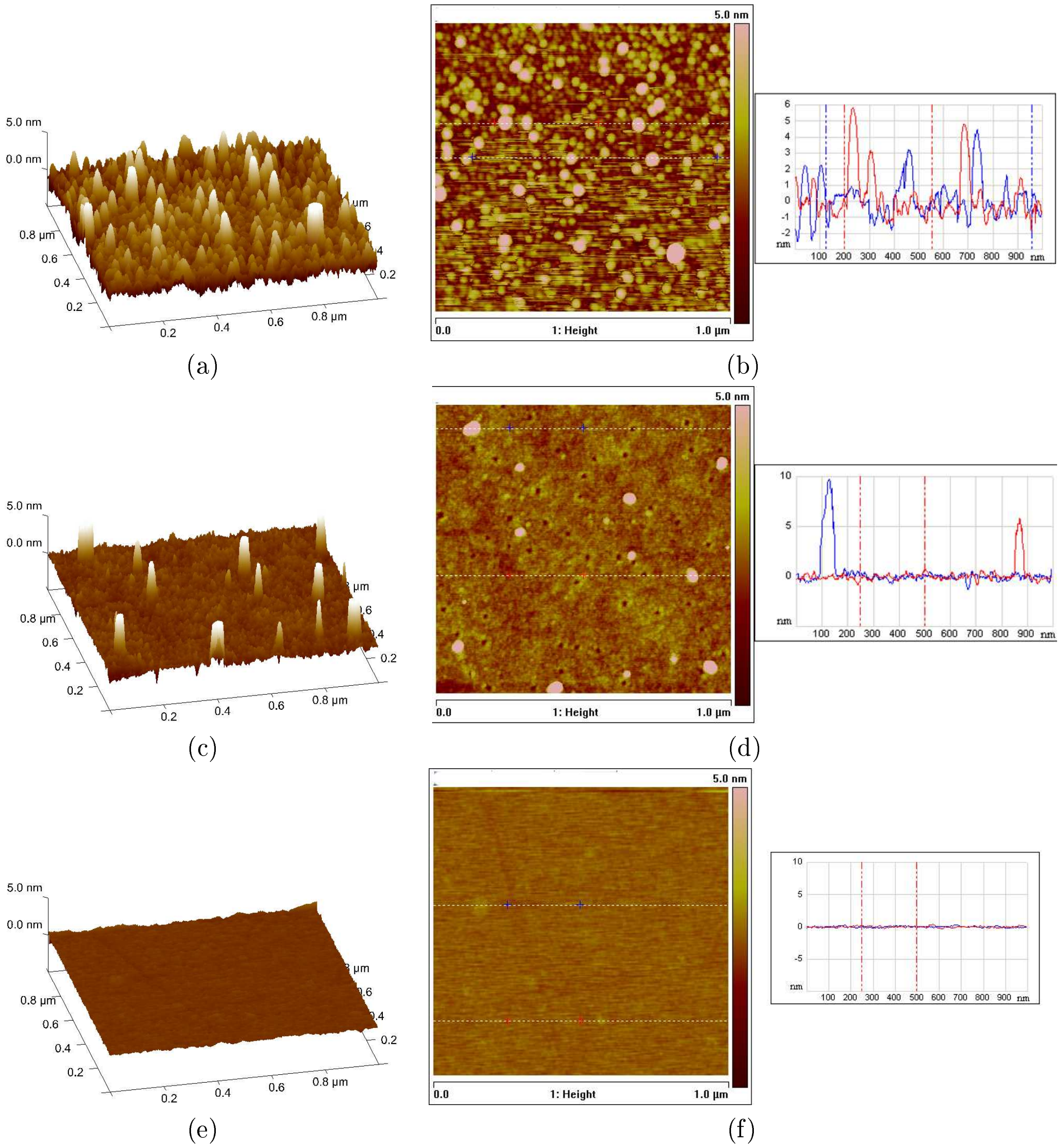

(a) (b) (c) (d) (e) (f)

Figure 3.6: AFM measurements of the DC sputtered ITO samples from Tab. 3.4. The 3d surface profile (left) and line scan data (right) are shown. The samples presented are those in Tab. 3.4 having the lowest R_s: (a)(b) sample 3 and (c)(d) sample 6. For comparison, the AFM scan of (e)(f) a bare silicon surface is added.

incubation time in PBS	$R_s=40\,\Omega$/sq	$R_s=60\,\Omega$/sq	$R_s=110\,\Omega$/sq
0 h	15k;13	1190k;10	569k;43
24 h	13k;14	59k;13	45k;26
48 h	13k;14	52k;13	45k;26

Table 3.5: Resistance and capacitance values $R/\,\Omega\cdot\mathrm{cm}^2$;$C/\,\mu\mathrm{F/cm^2}$ of the ITO surface in PBS measured by impedance spectroscopy. The values are least-squares fits to the data presented in Fig. 3.7. Results of three ITO samples having different sheet resistance R_s are presented.

of 0.3 Pa from a non-oxidized target (Fig. 3.6a) and those samples processed at 1 Pa from an oxidized target (Fig. 3.6c). In the first case, the AFM picture shows a surface consisting of homogeneously distributed spikes having an average height of 10 nm. The Z-range was 6 nm and the RMS value was 0.6 nm. For the sample in Fig. 3.6c, where oxygen and a higher pressure were used, the RMS increased to 1 nm and the Z-range to 10 nm. The same samples also show an increase of the spike height to 10-20 nm. Compared to the bare silicon surface both of the ITO layers show a drastic difference in terms of surface roughness and homogeneity.

To test electrochemical stability of the ITO layer impedance spectra were recorded for three different ITO samples at varying time intervals. Examples of the spectra are presented in Fig. 3.7. The ITO layer of the three samples had a specific sheet resistance R_s of $40\,\Omega$/sq, $60\,\Omega$/sq and $110\,\Omega$/sq respectively. The electrolyte used was the PBS solution of the CcO binding procedure. The slides were pre-cleaned using isopropanol and UV-ozone treatment. The electrochemical cell was assembled and PBS was filled into the cell. Impedance spectra were measured within time intervals of 0 h, 24 h and 48 h.

For all three ITO samples the resistance decreased significantly within the first 24 h, whereas the capacitance increased. This effect was even more predominant in the case of the ITO sample having a R_s value of $60\,\Omega$/sq. There, the resistance decreased by three orders of magnitude from around $1\mathrm{M}\,\Omega\cdot\mathrm{cm}^2$ to $60\mathrm{k}\,\Omega\cdot\mathrm{cm}^2$. The capacitance in all three cases decreased to a value of 13-14 $\mu\mathrm{F/cm^2}$. This value can be attributed to the space charge capacitance of the ITO semiconductor, since the Helmholtz capacitance under the conditions given here is usually around 25 $\mu\mathrm{F/cm^2}$. Capacitance and resistance of the ITO layer in PBS did not change further for time intervals longer than 24 h, as was deduced from the data after 48 h. An explanation for this behavior can be a

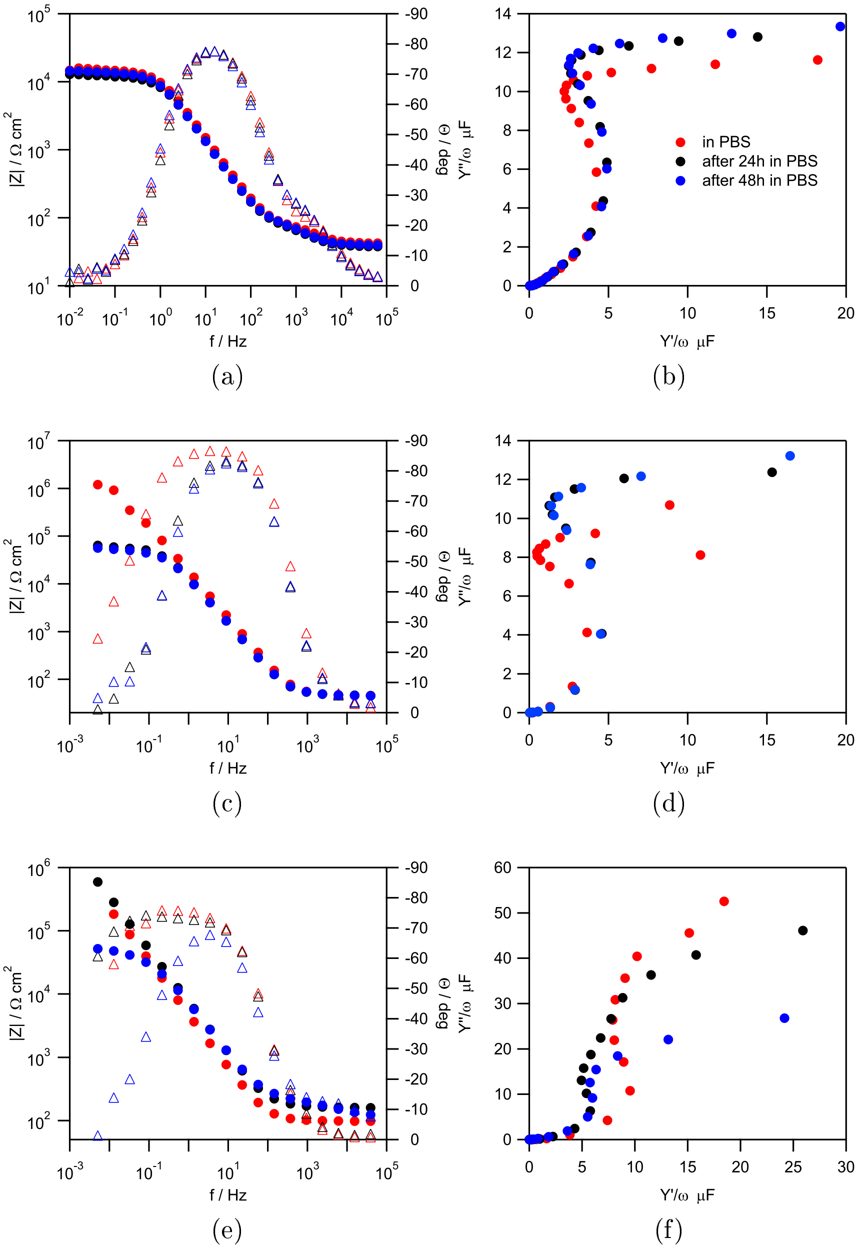

(a) (b)

(c) (d)

(e) (f)

Figure 3.7: Bode plot (left) and admittance (right) of the impedance spectra of bare ITO electrodes in PBS (red) measured after 24 h (black) and 48 h (blue). The sheet resistance of the ITO layers are 40 Ω/sq (c), 60 Ω/sq (a), 110 Ω/sq (e)

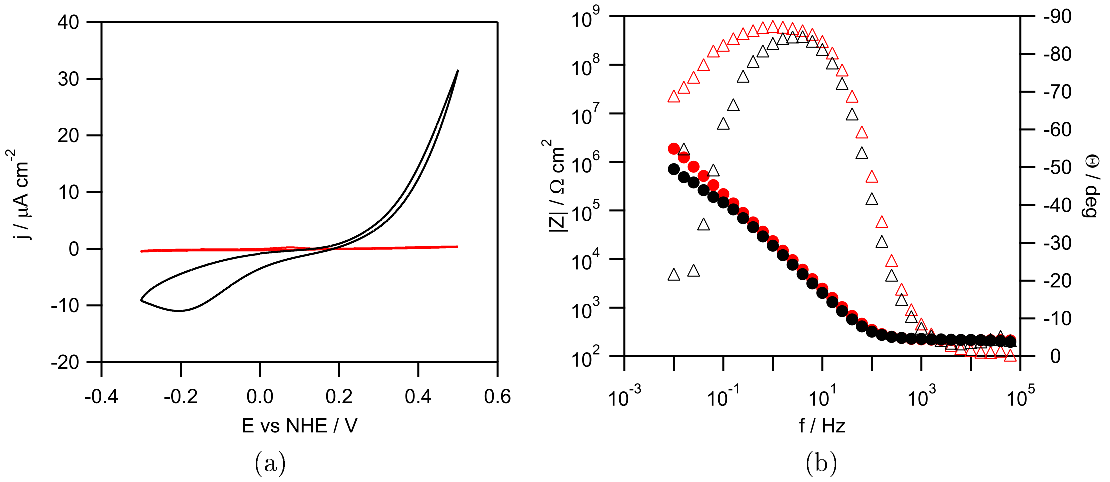

(a) (b)

Figure 3.8: Potassium ferrocyanide in KCl on a bare ITO electrode (R_s around 1k Ω/sq) measured by CV (a) and impedance spectroscopy (b). The concentration of $[Fe^{II}(CN)_6]^{-4}$ was 1 mM in a 0.1 M KCl buffer. The CV scan rate was 10 $^{mV}/_{s}$. The reference measurement without potassium ferrocyanide is shown in red.

'swelling' process during which water is taken up by the ITO layer. This uptake of water molecules would reach an equilibrium after a certain time. Since water has a dielectric constant of 80, the capacitance increases as expected. This suggestion is supported by the AFM measurements of the DC sputtered ITO surface. The ITO bulk layer itself consists of grains forming a column like structure into the direction of the layer growth. The grain size distribution depends on the sputtering parameters. The gaps between the grain structure can form pores. Hence the layer would also have properties similar to nano-porous materials, where diffusion of specimen into the pores was already observed[114].

The electron transfer properties of the ITO layer were measured by CV. Ferrocyanide $[Fe^{II}(CN)_6]^{-4}$ was used as redox species in a KCl solution. Before adding ferrocyanide background scans of the bare ITO surface were taken. The CV scans of ferrocyanide in KCl on unmodified ITO having a high sheet resistance R_s (Fig. 3.8a) show a quasi-reversible electrochemical behavior of ferrocyanide. In Fig. 3.8a, after 1 mM of ferrocyanide had been added the cathodic charge flow was 28 $^{mC}/_{cm^2}$ and the peak position at -76 mV. No distinct anodic peak could be observed. The impedance spectra show a decrease of resistance from 4.5M Ω·cm^2 to 0.35M Ω·cm^2 whereas the

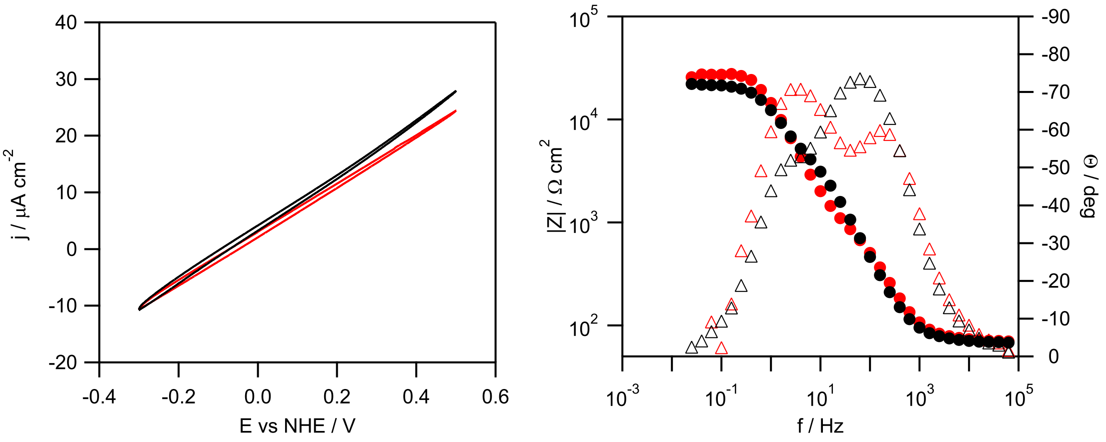

(a) (b)

Figure 3.9: Potassium ferrocyanide in KCl on a silanized ITO electrode measured by CV (a) and impedance spectroscopy (b). The concentration of Fe(CN)_{64}^{-} was 1 mM in a 0.1 M KCl buffer. The CV scan rate was $10\,\text{mV}/\text{s}$. The reference measurement without potassium ferrocyanide is shown in black.

capacitance increased from $7\,\mu\text{F}/\text{cm}^2$ to $9\,\mu\text{F}/\text{cm}^2$. This data suggest a comparably slow electron transfer of ferrocyanide to ITO [80] as expected from the high sheet resistance.

To investigate the effect of a 'blocking' ad-layer alkensilane had been used to silanize the ITO surface. Silanization was completed by incubation using a 1 % solution in THF. The monolayer thickness measured by ellipsometry was 1 nm. The CV scans of the silanized slides in Fig. 3.9a show no cathodic current peak when ferrocyanide was added, indicating the electrical 'barrier' properties caused by a dense silane monolayer. The resistance measured by impedance spectra decreased from 29k $\Omega{\cdot}\text{cm}^2$ to 19k $\Omega{\cdot}\text{cm}^2$. This decrease is lower compared to the CV scans of ferrocyanide in KCl on unmodified ITO. Hence, it can be concluded that any kind of electrical barrier having a comparable thickness will similarly hinder the electron transfer between a redox species and the electrode. This would also explain the very slow electron transfer properties of the ITO surface, if some kind of 'natural' passivating layer between the ITO bulk and the solution is existing. The existence of such a layer would than lead to the high charge transfer resistance observed for the bare ITO surface. As can be deduced from Tab. 3.5, the charge transfer resistance values for the bare ITO are by an order higher than expected from the R_s values of the respective surface.

The charge transfer property of the ITO layers having a low R_s (15 Ω/sq) was also

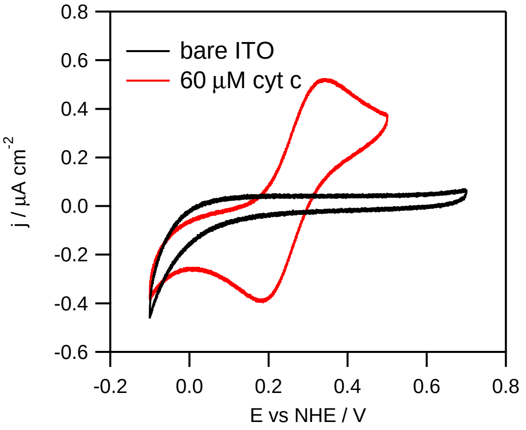

Figure 3.10: CV measurement of cyt c in PBS on ITO. R_s of the ITO layer $15\,\Omega/\mathrm{sq}$. A reference scan of the bare ITO layer is also presented. The scan rate was $10\,^{\mathrm{mV}}/_{\mathrm{s}}$.

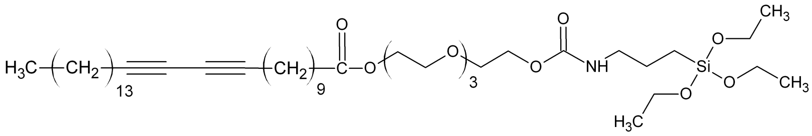

Figure 3.11: Single stranded anchor lipid $HC(EO)_4TES$ used for the formation of a tBLM on ITO. Synthesis by Mathieu Jung[53].

investigated. This time, a solution of cyt c in PBS has been used as the redox species. Cyt c will be employed as an electron donor for the CcO in a ptBLM, which will be presented later in this work. As can be seen from Fig. 3.10, the CV measurement shows a quasi-reversible electrochemical behavior indicating a low charge transfer resistance at the ITO-solution interface.

In summary, the characterization of the ITO surface has been presented so far. Here, it was shown by AFM that the ITO surface morphology features a comparably high surface roughness with distinct peaks covering the entire surface. Therefore, a tBLM system using anchor lipids was employed as a test system in order to analyze the formation of tBLM before the ptBLM was formed on ITO.

3.2.3 Tethered-BLM on ITO

The single stranded anchor lipid used here for the formation of a tBLM on ITO was synthesized by Dr. Mathieu Jung[53].

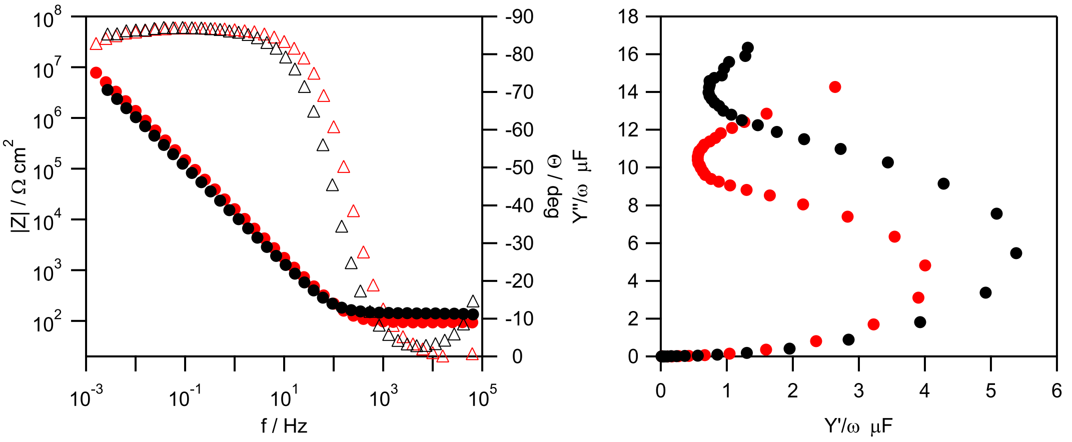

(a) (b)

Figure 3.12: Bode (a) and admittance (b) plot of the impedance spectra of the liposilane monolayer on ITO before (black) and after vesicle spreading (red). The spectra were measured in PBS. Lipid concentration of the vesicle solution was $0.04\,\mathrm{mg/mL}$.

A tethered bilayer lipid membrane (tBLM) was deposited on ITO. For this purpose the ITO surface was coated with Heptacosa-10,12-diynoic acid-tetraethylene glycol ester-[3-(triethoxysilyl) propylcarbamate] (HC(EO)$_4$TES) of which the structure is depicted in Fig. 3.11. The ITO slides were cleaned by sonication in isopropanol and afterwards hydroxylated by UV-ozone treatment. The surface was coated with HC(EO)$_4$TES by LB transfer. The monolayers were transferred at surface pressures of 50mN/m from the water subphase via LB transfer with a deposition speed of 1 mm/min. A suspension of liposomes in PBS was prepared by extrusion (100 nm). A diluted concentration of a stock solution ($2\,\mathrm{mg/mL}$) was added and the cell was flushed with PBS after 24 h. Finally the electrical sealing properties of the tBLM were measured by impedance spectra.

The impedance spectra of the lipid coated ITO show a high resistance value of $81\mathrm{M}\,\Omega\cdot\mathrm{cm}^2$ indicating a dense monolayer of lipids on the surface. The capacitance of the lipid layer was at $14\,\mathrm{\mu F/cm^2}$. After adding a diluted vesicle solution the resistance increased slightly to $82\mathrm{M}\,\Omega\cdot\mathrm{cm}^2$ whereas the capacitance decreased significantly to $11\,\mathrm{\mu F/cm^2}$ which is comparable to the values reported for a tBLMs on other oxidic surfaces[114]. Because of the already high resistance caused by the densely packed HC(EO)$_4$TES the increase of resistance derived from the nonlinear fit after formation of a lipid bilayer was comparably low. However, the decrease of capacitance indicates that a closed bilayer of lipids has formed. This conclusion was also supported by membrane potential measurements which will be presented in chapter 4.

3.2.4 Protein-tethered BLM on ITO

First, the ITO slides were sonicated in isopropanol then in Hellmanex. Thereafter, the ITO surface was hydroxylated by UV-ozone treatment. The same ptBLM binding procedure was used as the one described already for silicon surfaces in section 3.1: a 1 % NHS-silane solution (see 3.1) was used to modify the ITO surface. The slides were incubated overnight, according to the optimized conditions derived for silanization of a silicon oxide surface. For ANTA coupling an incubation time of 2 h was used, in order not to deteriorate the ITO surface. Afterwards CcO was immobilized on the surface and DiPhyPC solubilized in DDM/PBS was added. The formation of the lipid bilayer between the proteins started after adding pre-cleaned bio-beads. Enzyme activity was initiated by adding reduced cytochrome c.

preparation steps	$R/\ \Omega{\cdot}\mathrm{cm}^2$	$C/\ {}^{\mu\mathrm{F}}/{}_{\mathrm{cm}^2}$
after Ni^{2+} complexation	1-7M	15-19
after CcO adsorption	1-4M	13-18
after *in-situ* dialysis	0.2-1M	12-18

Table 3.6: Resistance and capacitance values of the ptBLM formation on NHS-silane functionalized ITO measured by impedance spectroscopy. The values are derived from least-squares fits to the spectra using equivalent circuit Fig. 3.13c.

The resistance decreased after each of the ptBLM formation steps as can be seen in Fig. 3.13. Before CcO adsorption the resistance was at $7\mathrm{M}\,\Omega{\cdot}\mathrm{cm}^2$. After CcO adsorption the value decreases to $4\mathrm{M}\,\Omega{\cdot}\mathrm{cm}^2$. *In situ* dialysis performed by adding bio-beads together with a solubilized lipid further decreased resistance to $0.2\mathrm{M}\,\Omega{\cdot}\mathrm{cm}^2$. The capacitance slightly decreased from $19\,{}^{\mu\mathrm{F}}/{}_{\mathrm{cm}^2}$ to $18\,{}^{\mu\mathrm{F}}/{}_{\mathrm{cm}^2}$ after CcO adsorption and did not decrease further after BLM formation. This results are in contrast to those obtained for the silicon surface. There an increase of resistance and a decreasing capacitance could be observed after each preparation step. To verify whether the enzyme had been reconstituted in a functional manner impedance spectra were measured before and after activation of CcO using reduced cyt c. The resistance decreased to

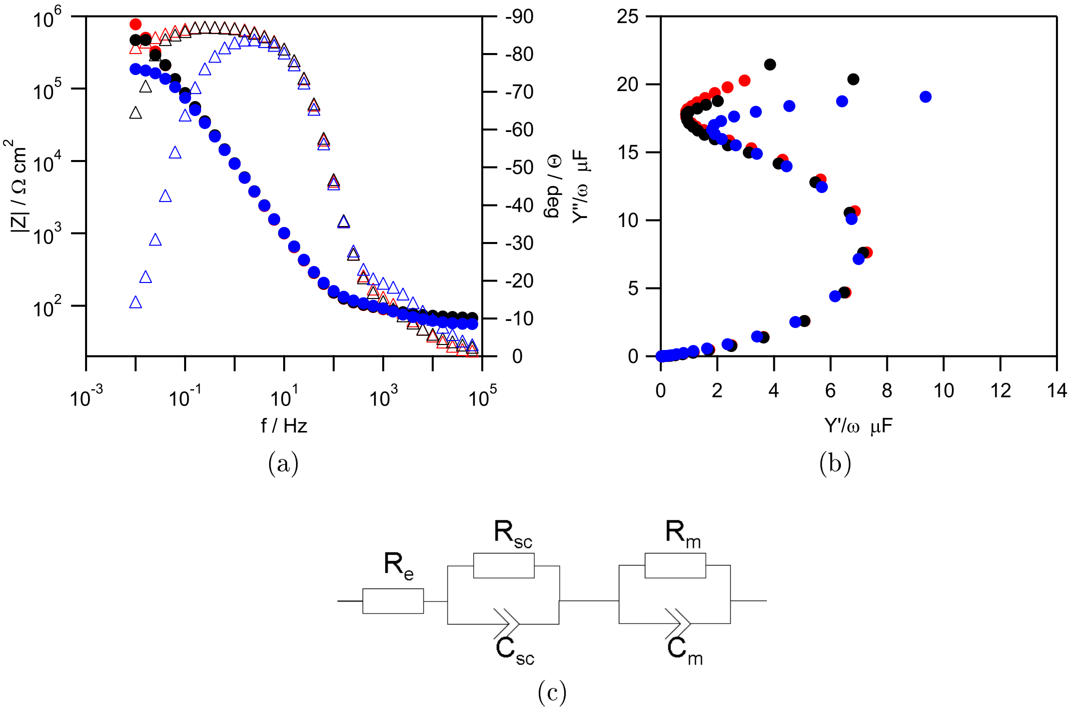

(a)

(b)

(c)

Figure 3.13: Bode (a) and admittance (b) plot of the impedance spectra of the ptBLM formation on NHS-silane functionalized ITO: Before CcO binding (red); after CcO binding (black), and after *in situ* dialysis using biobeads (blue). Equivalent circuit (c) was used for fitting.

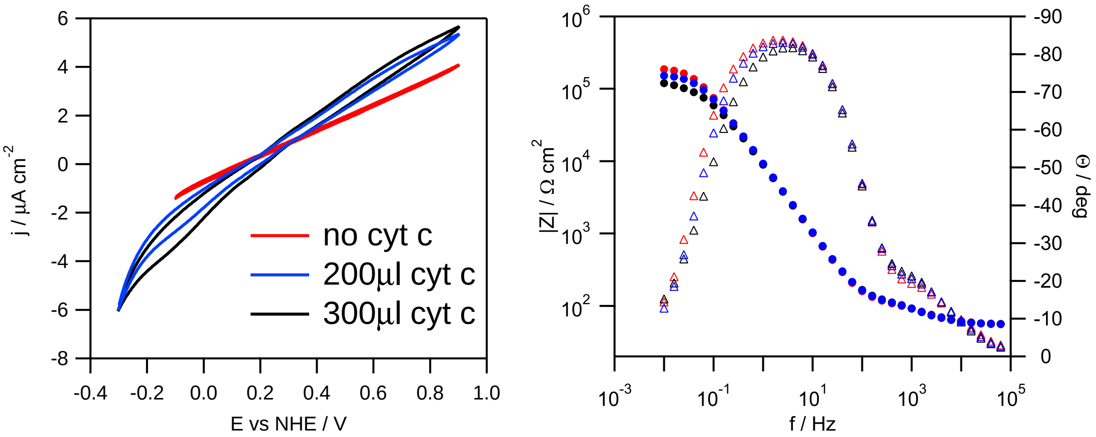

(a) (b)

Figure 3.14: Enzyme activity of CcO incorporated in a ptBLM on NHS-silane functionalized ITO measured by CV (a) and impedance spectroscopy (b): before adding cytchrome c (red), after addition of (black) 0.2 mM and (blue) 0.3 mM reduced cyt c. The scan rate was 10 $^{\mathrm{mV}}/_{\mathrm{s}}$.

120 Ω·cm^2 after reduced cyt c was added to the buffer solution. The enzyme activity was also measured by CV (Fig. 3.14). After adding reduced cytochrome c a weak cathodic peak at a potential of -100 mV could be detected.

Comparing both data, CV and impedance spectra, the formation of closed, electrically sealing lipid bilayer could not be verified. However, CV scans show that there is a small catalytic activity of reconstituted CcO on ITO suggesting that fragments of ptBLM exist on the ITO surface. An explanation for the insufficient ptBLM formation is the high surface roughness that could be observed for the ITO surface. The Z-range values presented in section 3.2.2 are within the range of 6-10 nm, which is already comparable to the size of the CcO on the surface. In addition, spikes having a height of 10-20 nm are distributed over the surface. This characteristics of the ITO surface clearly hinder the formation of a closed lipid bilayer. A modified surface modification technique has to be implemented. The drawback of a very rough surface has to be overcome and at the same time the modification has to provide the proper functionality to immobilize CcO and reconstitute the protein into a lipid bilayer. A polymer network bound to ITO possessing functional groups for ANTA coupling can achieve this goals. A new method will be presented now, employing a thin hydrogel layer as a polymer cushion for the ptBLM.

3.3 The Hydrogel-supported ptBLM on ITO

The work presented here was part of a cooperation with Robert Roskamp and Uli Jonas. The hydrogel described in this section was synthesized by Robert Roskamp, who also developed the spin coating procedure for the ITO.

A new approach in the direction polymer-supported membranes is an assembly that starts with immobilizing the protein to be investigated specifically on the top layer of the polymer. This can be achieved by using a hydrogel as the polymer layer with mesh sizes smaller than the size of the protein. The gel is provided with a binding motif such as an NTA functionality chelated with Ni^{2+} ions designed to bind the protein via the his-tag technology. Since the protein is too big to penetrate the gel, it stays on the surface. If a lipid bilayer could then assembled around the protein, the formation of a defect-free electrically sealing protein-lipid layer could be expected. A similar approach had been successfully applied before, however, on a short spacer layer rather than a polymer. The sealing properties of ptBLM were sufficient to allow for electron and ion transport processes through the cytochrome c oxidase. In the present study a hydrogel consisting of poly(N-(2-hydroxyethyl)acrylamide-co-5-acrylamido-1-carboxypentyl-iminodiacetate-co-4-benzoylphenyl methacrylate) (P(HEAAm-co-NTAAAm-co-MABP)) will be employed to bind the same protein via the already described His-tag technology. A lipid layer will be then assembled by in-situ dialysis around the protein. A number of surface-analytical techniques will be employed to characterize the system including the activity of the protein Fig. 3.15.

3.3.1 Polymerization of P(PFPA-co-MABP)

4-(3-triethoxysilyl)propyloxybenzophenone (benzophenone-silane) [37], pentafluorophenyl acrylate (PFPA)[26] and 4-methacryloyloxybenzophenone (MABP)[130] were prepared according to literature. Azodiisobutyronitrile (AIBN) was recrystallized from methanol. Dioxane was distilled over calcium hydride.

The reactive copolymer was polymerized from 98 % mol PFPA and 2 % mol MABP by free radical polymerization with 0.2 % mol AIBN in dioxane at 60ï£¡C for 48h. It was precipitated in methanol and dried in high vacuum.

The reactive copolymer P(PFPA-co-MABP) was obtained with a yield of 78 % after precipitating it three times from benzene in methanol. The molecular weight Mn was

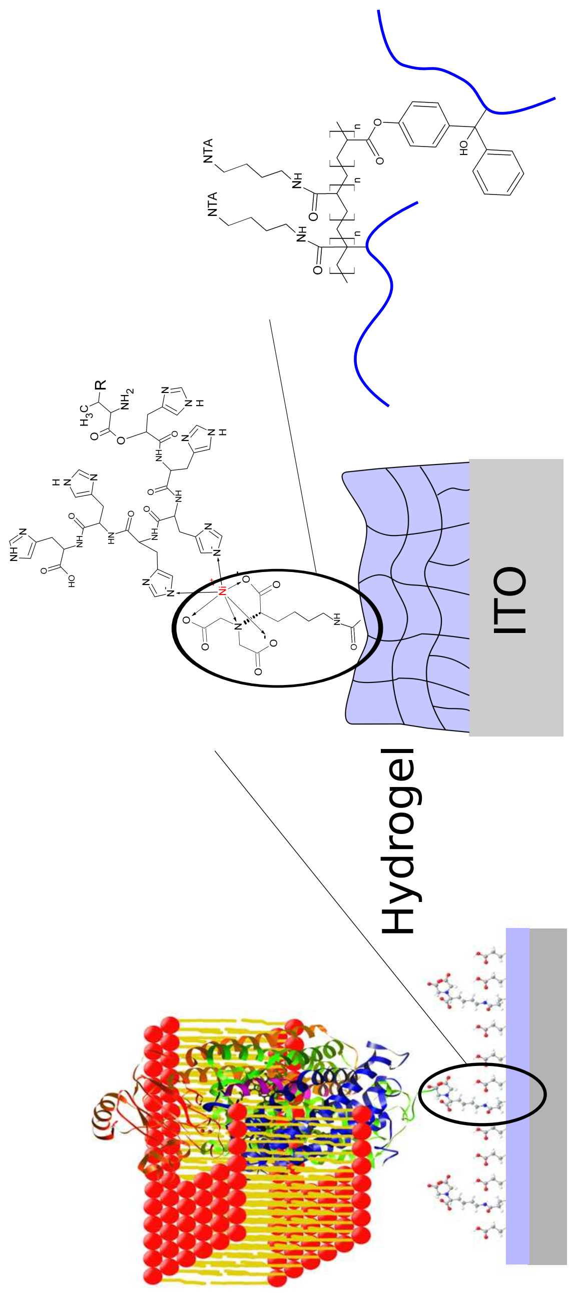

Figure 3.15: Schematics of the protein-supported bilayer lipid membrane (ptBLM) bound to the top layer of a hydrogel. Formation of the ptBLM started with immobilization of *cytochrome c oxidase* with the his-tag attached to SU I via the Ni complex to the NTA modified hydrogel P(HEAAm-co-NTAAAm-co-MABP).

determined by GPC (THF with pmma as standard) to be 14.000 g/mol and the molecular weight distribution was 2.1. The 1H-NMR shows the peaks of the PfpA and the MABP with a ratio of 98 : 2 as intended by the monomer mixture. 1H-NMR (700 MHz, CD2Cl2): [ppm] = 7.45 (br m, 9 H, benzophenone), 3.11 (br s, 1 H, CH, backbone), 2.15 (br s, 2 H, CH2, backbone), 1.48 (br m, 3 H, CH3, backbone).

3.3.2 The formation of the ptBLM on PFPA copolymer

ITO layers prepared as described in section 3.2.1 were provided with a 60 nm thick layer of the copolymer P(PFPA-co-MABP). At a mixing ratio of 98 mol PFPA and 2 mol MABP the copolymer is highly cross-linked and very hydrophobic due to the hydrophobic nature of the active ester functionalities (pentafluorophenyl). A high degree of cross-linking is needed to be able to mainly functionalize the surface functionalities of the polymer rather than the inner network. Nevertheless, the active ester allows for further functionalization with hydrophilic groups to form a hydrogel. The active ester functionalities were converted to NTA-groups by a reaction with ANTA. Residual active ester functionalities were converted to terminal OH groups by a reaction with aminoethanol. The thickness of the polymer layer was determined by SPR/OWS and AFM to be 60 nm.

AFM measurements showed the spike structures of the ITO layer described in section 3.2.2 almost completely covered by the polymer layer (Fig. 3.17). Electrochemical impedance spectra showed a dramatic increase of the capacitance and a decrease of the resistance due to the functionalization (Fig. 3.18). This can be explained by the hydrophobic active ester functionalities (PFPA), which do not allow for any water molecules to penetrate the polymer. The capacitance of the layer structure is thus determined by the space charge capacitance of the semiconductor. When the active ester was functionalized with hydrophilic groups such as NTA and OH, water molecules could enter the polymer together with ions from the buffer solution to form a kind of Guy-Chapman electrical double layer with capacitances in the order of magnitude of 16 $^{\mu F}/_{cm^2}$, actual values depending on the particular preparation. The resistance of this layer was in the order of kΩ as expected.

The NTA functionalities were converted to the Ni-NTA chelate by immersion of the gel layer into a buffered NiSO4 solution. The excess Ni was removed by rinsing with an acetate buffer solution (pH=4). After that a solution in detergent (DDM)

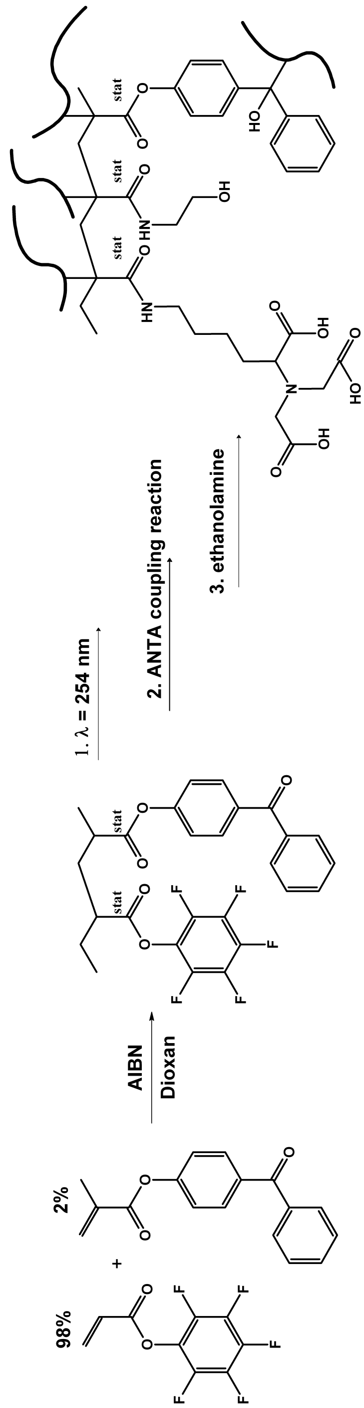

Figure 3.16: Synthesis of the precursor polymer P(PFPA-co-MABP) and its conversion into the PHEAAm-hydrogel with attached NTA groups (P(HEAAm-co-NTAAAm-co-MABP)).

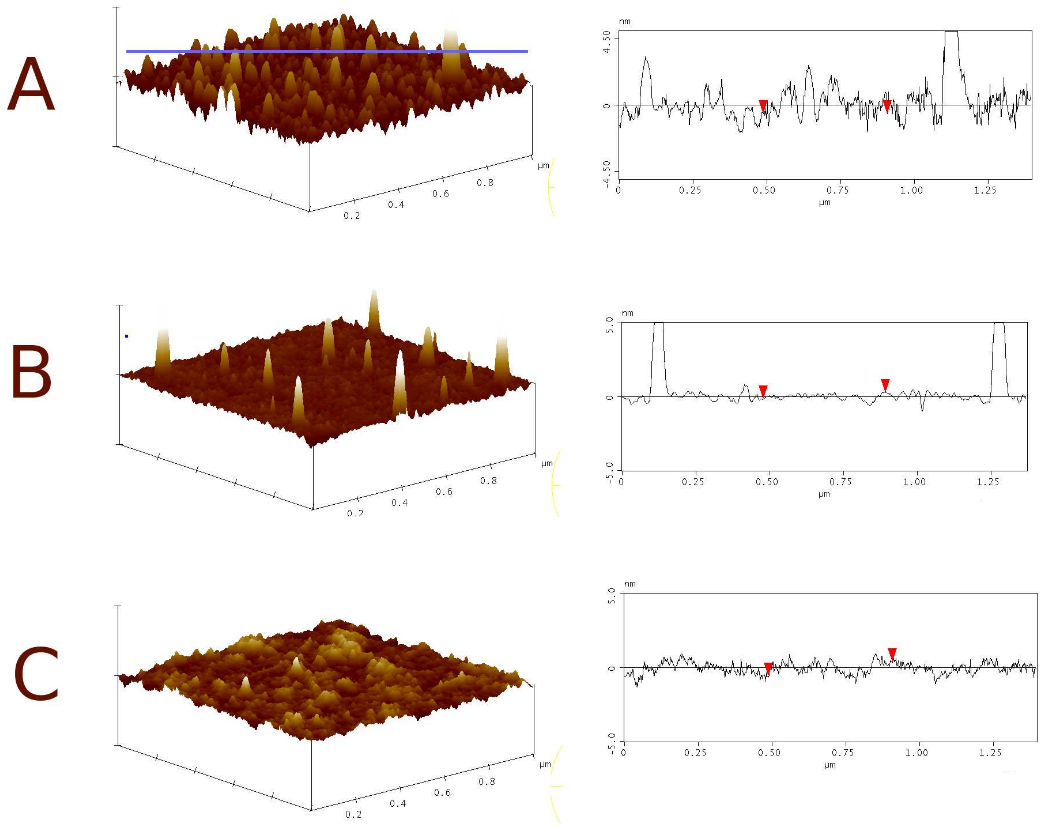

Figure 3.17: 3D surface profile (left) and corresponding line-scan (right) of DC sputtered ITO; (A) sample 3 and (B) sample 6 from Tab. 3.4. The hydrogel coated sample (C) is also shown. The electrode surface is smoothed and the spikes are covered by the gel. The location of the line scan on the left is indicated by the blue line in (A) and was the same in all three samples.

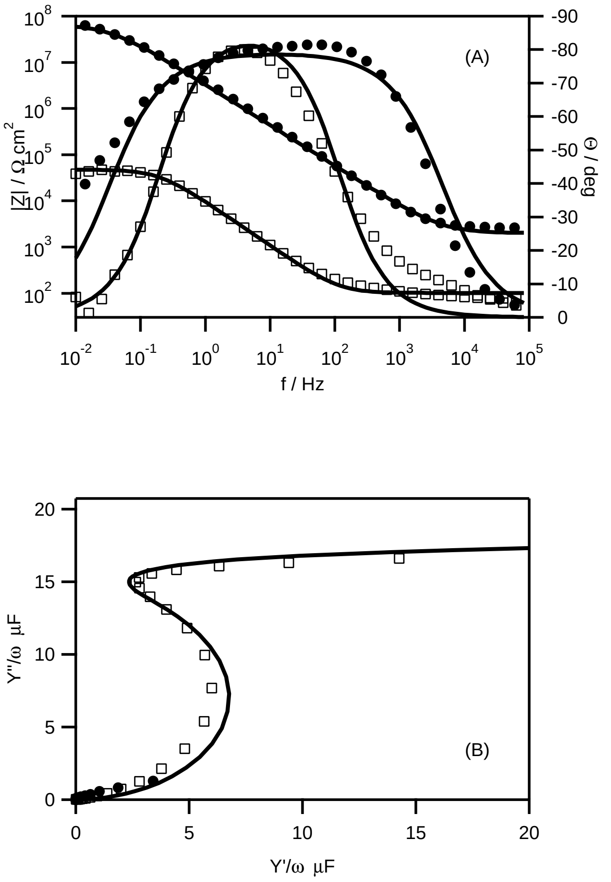

Figure 3.18: Frequency response presented as (A) bode and (B) frequency normalized admittance plot of the ITO coated with the P(PFPA-co-MABP) precursor; (•) before and (□) after conversion to P(HEAAm-co-NTAAAm-co-MABP) using ANTA and ethanolamine. Also shown are the fits (solid lines) using Fig. 3.19c.

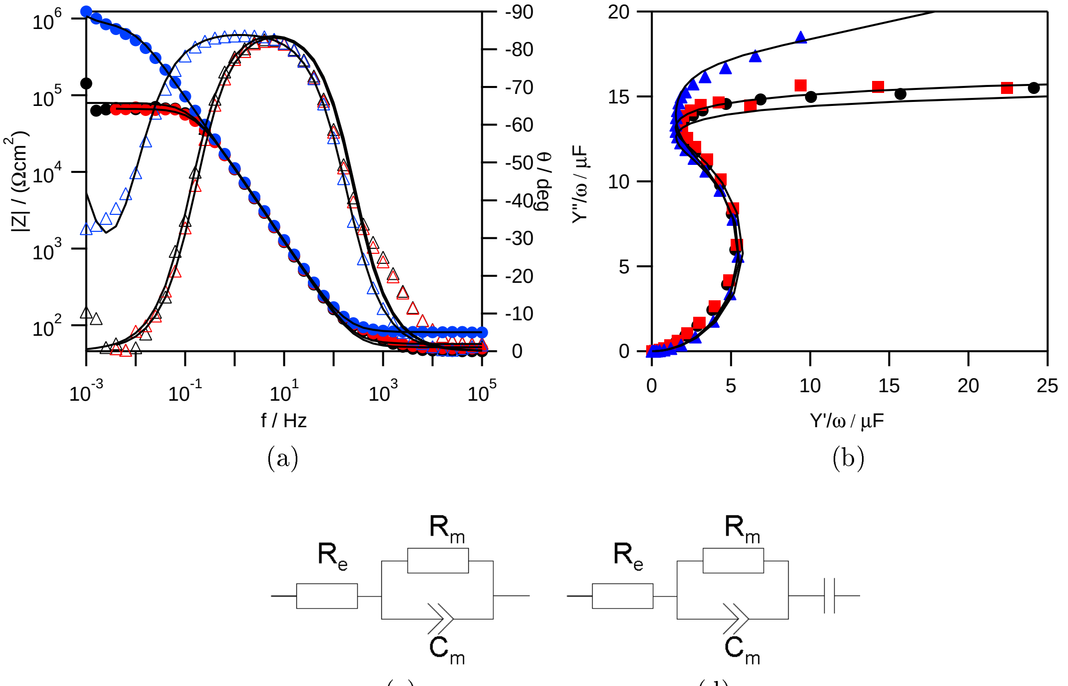

(a) (b)

(c) (d)

Figure 3.19: (a) Bode plot and (b) frequency normalized admittance of the Ni_2^+-NTA modfied P(HEAAm-co-NTAAAm-co-MABP) on ITO before (black) and after (red) binding of CcO; (blue) after in situ dialysis to form the lipid bilayer around the protein. Solid lines show the fitted curves using (c). For the fit to the blue data (d) was used.

ITO samples at different preparation step	$R_\mathrm{m}/\ \mathrm{M\Omega\cdot cm^2}$	$C_\mathrm{m}/\ \mathrm{\mu F/cm^2}$
P(PFPA-co-MABP) coated ITO	>60	0.04
...after conversion to hydrogel	0.02-0.04	13-16
...after CcO binding	0.07-0.11	14-16
...after in-situ dialysis	1-5	12-15

Table 3.7: Capacitance and resistance values after each step of the preparation of a ptBLM on polymer coated ITO. The values are results of a least squares fit using equivalent circuits in Fig. 3.19.

of CcO from *Rh. Sphaeroidis* with a his-tag attached to subunit II was added to the bathing solution. It is seen in Fig. 3.19 that the impedance spectrum did not change much, although the binding of CcO could be detected by waveguide measurements described further below. However, when the phopholipid (DiPhyPC) solubilized in DDM was added together with bio-beads, the resistance increased by two orders of magnitude to reach values around 0.6-2 $\mathrm{M\Omega\cdot cm^2}$, Fig. 3.19 shows a typical example. This indicates the insertion of lipid bilayer patches between the CcO molecules or in other words the formation of a ptBLM. EIS data are collected in Tab. 3.7. The resistance of 1-5 $\mathrm{M\Omega\cdot cm^2}$ is in accordance with results obtained for ptBLMs on smooth gold films without a gel layer. The resistance is known to be a very critical parameter to indicate a defect-free lipid bilayer. Values in the order of magnitude of $\mathrm{M\Omega\cdot cm^2}$ are known from BLMs and tBLMs, whereas for polymer-supported bilayers such high sealing resistances were hard to achieve. The capacitance does not change because it is dominated by the capacitance of the gel as well as the protein layer, which are expected to be in the same order of magnitude. The high resistance after dialysis, however, indicates that CcO molecules were bound mainly to the surface layer rather than the meshes of the gel layer. Only protein molecules attached to the surface can form a closed protein-lipid layer as requested for a ptBLM. The CcO is anyhow to large (9x8 nm) to penetrate the gel, particularly at the high degree of cross-linking.

3.3.3 Characterization by waveguide measurements

EIS is not designed to follow the binding of the CcO to the NTA functionalized polymer layer. The formation of the lipid bilayer can be deduced from these measurements, but only indirectly. More information can be expected from SPR/OWS measurements, which were performed on a thick (680 nm) ITO layer as the wave guiding

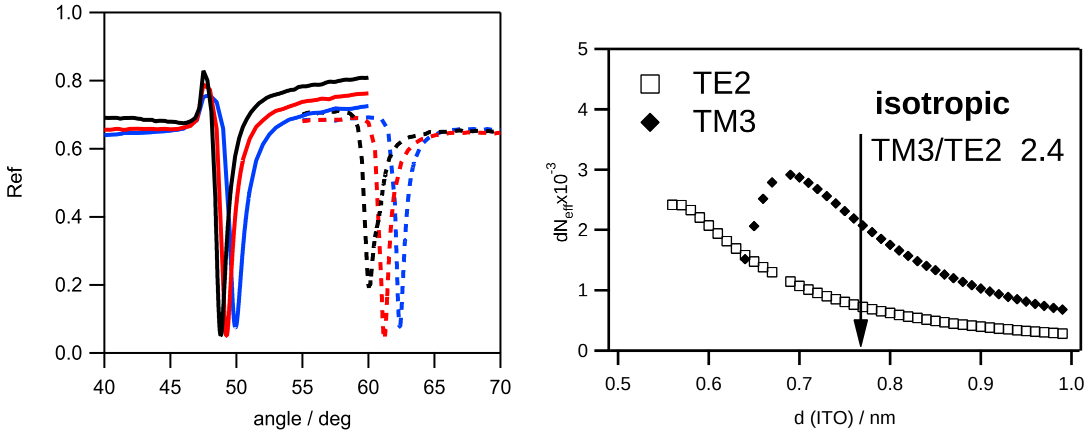

Figure 3.20: (a) SPR/OWS angle spectra of (solid line) p-polarized and (dashed line) s-polarized light (632nm) of (black) Ni^{2+}-NTA modified P(HEAAm-co-NTAAAm-co-MABP) on ITO before and (red) after binding of CcO; (blue) after *in situ* dialysis to form the lipid bilayer around the protein. (b) Simulated shifts of the effective refractive dN_{eff} caused by an isotropic ad-layer (n=1.47, d=10nm) calculated for TE and TM modes as a function of the thickness of the ITO layer (n=1.9065): (◆) TM_3, (□) TE_2. The arrow indicates the thickness of the ITO layer used on a routine basis.

media. SPR/OWS is a multi-mode technique with TM and TE modes, i.e. angle scans obtained from p-polarized and s-polarized light, respectively. Binding as well as lipid reconstitution could be clearly seen as a shift of the TM_3 (p-polarized) and the TE_2 mode (s-polarized) in the angle spectra in Fig. 3.20a. The effective refractive indices N_{eff} of the propagating TM_3 and TE_2 (Tab. 3.8) are calculated from the angle spectra using (2.42)

Changes of dN_{eff} from one layer to the next give information about the anisotropy of the layers. From the angle scans it is already obvious that the two modes shift differently for each layer formation. In order to obtain a more quantitative information dN_{eff} values of the two modes were simulated for the isotropic case as a function of the thickness of the ITO layer. The thickness of the gel-support was set 60 nm. From this so-called sensitivity curve (Fig. 3.20b) the expected absolute shift dN_{eff} of both modes, TM_3 and TE_2 at a particular thickness d of the ITO layer, can be derived. In the experiments performed here the two modes should shift at a ratio TM_3:TE_2 of 2.4:1 provided the layers are isotropic.

The actual dN_{eff} values derived from the N_{eff} in Tab. 3.8 show different behavior,

Preparation steps	N_{eff} TM3	N_{eff} TE2
Ni2+-NTA modified P(HEAm-co-TAAm-co-MABP)	0	0
...after CcO adsorption	$2.971 \cdot 10^{-3}$	$6.432 \cdot 10^{-3}$
...after in-situ dialysis for formation of the BLM	$5.875 \cdot 10^{-3}$	$8.243 \cdot 10^{-3}$

Table 3.8: The change of the effective refractive index N_{eff} of the TE_2 and TM_3 modes after each preparation step calculated using (2.42).

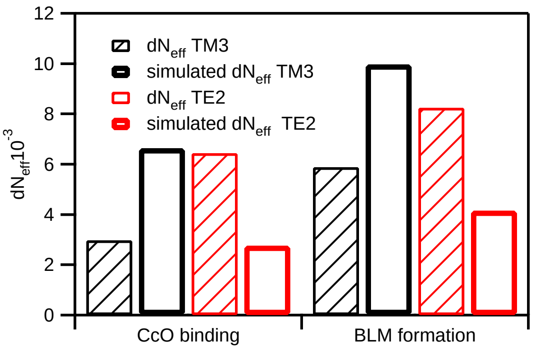

Figure 3.21: Change of the effective refractive index, dN_{eff} for the TM and TE optical waveguide modes after each preparation step of the ptBLM on P(HEAAm-co-NTAAAm-co-MABP). The dN_{eff} values were derived from the N_{eff} in Tab. 3.8. Results from simulations using an isotropic adlayer and the software described in experimental part are also presented.

Fig. 3.21 presents actual and simulated dN_{eff} of the protein and the protein/lipid layer. In both cases the two modes, TE_2 and TM_3, shift at a ratio different from the theoretical one. The TE_2 mode shifts even stronger than the TM_3 mode in contrast to what is expected from simulation data. This result can only be explained by an anisotropy of both the CcO and the lipid/CcO layer. However, with the dipole moment directed along the x-axis of the CcO a shift of the TE mode indicates the CcO molecules being arranged more parallel to the surface rather than perpendicular. They seem to rearrange into a more upright position as deduced from the difference between TE and TM modes decreasing after insertion of the lipids as required for a well-ordered planar lipid bilayer.

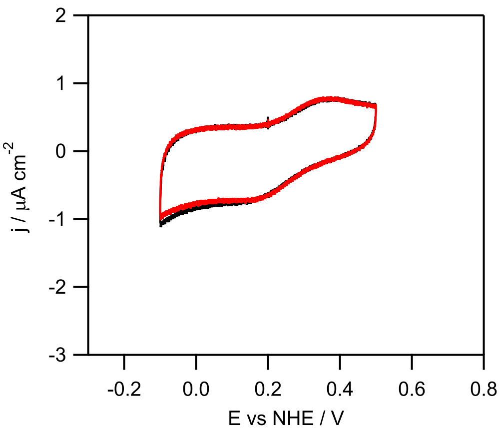

Figure 3.22: Cyclo voltamogram of cytochrome c after CcO binding and before ptBLM formation. A 50 µM solution of reduced cytochrome c in PBS was added to the system. The scan-rate was 50 mV/s. Two scans are presented, one taken immediately after cytochrome c was added (black) and one 30 min later (red).

3.3.4 Penetration of cyt c through the gel layer

Cyt c is known to be adsorbed to NTA functionalities. Hence it was interesting to test whether or not cyt c would be able to penetrate the NTA-OH functionalized hydrogel. For this purpose, CVs were measured of the ptBLM in PBS buffer before and after adding cyt c to the buffer solution (Fig. 3.22). The CVs recorded immediately after the addition of cyt c showed oxidation/reduction peaks with a peak separation of 160 mV. The detergent solubilized protein layer did not pose a barrier to cyt c. The CV recorded immediately after cyt c insertion and 30 min later do not differ. When the ptBLM was formed, the slowly increasing peaks in the CV showed that the lipid membrane effectively hindered the cyt c penetrating the gel (Fig. 3.23).

3.3.5 Enzyme activity of the CcO residing in the gel-supported ptBLM

Finally he Enzyme Activity of the CcO was probed by EIS after adding reduced cyt c to the ptBLM assembly. The resistance decreased at least by an order of magnitude and could be restored by flushing the cyt c away with fresh buffer. A typical example is shown in Fig. 3.23. These data are very well comparable to previous measurements

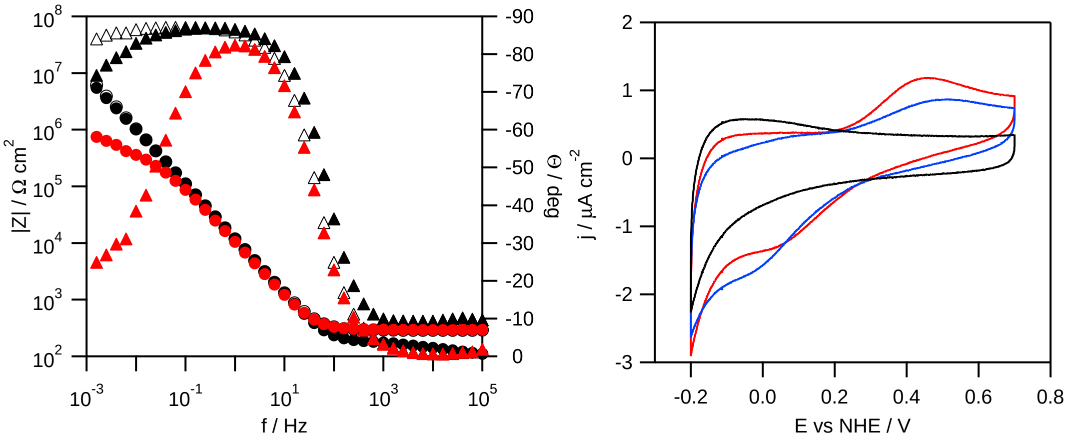

(a)

(b)

Figure 3.23: Bode plot of the impedance spectra (a) and cyclo voltamogram (b) of cyt c activated CcO after ptBLM formation. A 50 µM solution of reduced cyt c in PBS was added to activate CcO. Bode plot (b) shows the spectra after ptBLM formation (empty symbols), after activation using cytochrome c (red) and after flushing the cell using PBS (black). The scan rate was 50 mV/s. The cyclo voltamogram (b) shows scans immediately after adding reduced cytochrome c (red), 30 min after adding cyt c (blue) and after flushing the cell using PBS (black).

with the ptBLM on smooth Au surfaces. Proton pumping activity was held responsible for the decrease of the resistance. This can be concluded from the complete restoration of the resistivity after removal of cyt c. A repeated electron exchange of cyt c with the electrode due to enzyme activity does not appear to take place. This was deduced from CVs in the absence and presence of oxygen. An amplification of the current was observed on the ptBLM on Au surfaces[35] contrary to the gel-supported ptBLM. In this case the CV showed not only an increase of the cathodic current, but also an increase in the peak separation to 364 mV between cathodic and anodic peaks. This can be explained in terms of the shuttle mechanism of electron transfer of cyt c between the enzyme and the electrode. In the case of the polymer cyt c has to overcome a much larger distance to carry the electron to the enzyme. Moreover the barrier properties of the lipids further limit the mobility of cyt c. Hence cyt c is expected to bind to its binding site on subunit II of the CcO, which is directed to the outside of the ptBLM where it elicits proton transport through the enzyme.

3.4 Summary

The ptBLM on NHS-silane modified silicon was presented. The modification of the silicon dioxide surface was shown to be dependent on incubation time and silane concentration. The best coverage measured by ellipsometry and contact angle was achieved at 1 % NHS-silane in THF and incubation overnight. The formation of a ptBLM on silicon oxide was also observed. Though the membrane resistance was significantly lower compared to the ptBLM on gold. The results derived from the measurements on silicon indicate that a ptBLM can be formed also on oxidic surfaces.

Thus the parameters for NHS-silane functionalization of the ITO surface were adopted from procedures developed previously. Formation of a ptBLM was measured by impedance spectroscopy. The activity of the CcO could be detected by cyclic voltammetry using its substrate cytochrome c in the reduced form. A weak catalytic current, verified by measurements under anaerobic and aerobic conditions, was observed. The reason for the weak activity is the imperfect lipid bilayer formation on ITO. From the characterization of the sputtered ITO it could be seen that the surface had a high roughness with spikes covering the entire surface. This characteristics of the ITO surface hinders the formation of a closed lipid bilayer. The ptBLM support on ITO had to be further modified in order to achieve CcO tethered BLM with good electrical sealing properties.

Therefore a gel-supported ptBLM was formed by copolymerization of PFPA and MABP. The very hydrophobic PFP-groups were converted into hydrophilic NTA and OH functionalities. The first ones were shown to bind the protein via the His-tag technology whereas the second ones provide hydrophilic end groups to form a hydrogel. This concept was shown to work in the direction of very robust polymer-supported protein-lipid layers. The polymer had to be highly cross-linked in order not to allow for a protein the size of the CcO to penetrate the polymer network. However, a smaller protein such as cyt c was shown to diffuse inside the gel layer so as to reach the ITO electrode. The presence of a well-ordered lipid bilayer could be demonstrated by EIS together with wave guide measurements. EIS spectra and CV scans of the cyt c activated CcO verified that the protein was reconstituted in a functional manner. EIS spectra are also compatible with a water-filled reservoir for ions.

Chapter 4

Measurement of the Membrane Potential by Fluorescence Spectroscopy

Optical recording of the transmembrane potential change generated by reconstituted ion translocating proteins had been described previously[21, 22, 94, 99, 104]. For example, membrane proteins like the H^+-ATPase[49] had been reconstituted into Proteolipsomes and the change of the transmembrane potential due to the formation of an electrochemical proton gradient was monitored using a fluorescent voltage probe. However, such investigations have not been conducted on planar membrane systems bound to electrodes.

Membrane potentials induced in a planar BLM, such as the ptBLM and tBLM on ITO, can be measured by fluorescence spectroscopy. In the first instance, the suitability of the ptBLM system on ITO for fluorescence measurements was verified using LHCII as the tethering protein. An attempt was made to use LHCII as a probe for the measurement of membrane potentials.

An alternative approach is a custom made voltage probe such as the chromophore aminonaphthylethenylpyridinium (Di-8-ANEPPS). These molecules are engineered to bind to and orient within a lipid bilayer in order to exhibit a direct electronic response to alterations in the membrane potential. The chromophore undergoes changes in its electronic configuration, in response to changes in the surrounding electric field. Emission ratio measurements allow membrane potentials to be quantified via a potential-dependent shift in the emission spectra.

4.1 The LHCII Complex in the ptBLM Measured by Fluorescence Spectroscopy

Light-harvesting complexes play a crucial role in photosynthesis. The major peripheral antenna complex LHCII (or LHCIIb) is one of the two existing types of chlorophyll a/b containing antenna complexes. This complexes are ordered in an arrangement surrounding the reaction centers in the photosystems I and II (PSI and PSII). All oxygen-evolving photosynthetic cells (e.g. those of higher plants and cyanobacteria) contain both photosystems I and II, whereas all other species of photosynthetic bacteria, which do not evolve oxygen only contain photosystem I. The function of the antenna complexes is to absorb light energy and transfer it to the reaction center, where it is used to drive chemical reactions within the cell. The PSII is so far the only complex known in nature that oxidizes water to oxygen (Fig. 4.1). Beside this remarkable characteristic, the fast (10-15 fs) and efficient energy transfer makes the LHCII also a potential candidate for light-harvesting applications in photo-electronic devices like photovoltaic cells. For those reasons, it belongs to one of the most extensively studied transmembrane proteins.

4.1.1 Structure and spectroscopic properties of the LHCIIb from pea

The LHCIIBb exist in monomeric and trimeric forms. It is believed that most LHCII complexes are arranged in a trimeric form, some minor antenna complexes might also occur in the monomeric form [73, 137].

The recombinant LHCIIb (Lhcb1) complex used in this work is a derivative of LHCb1*2 (AB80) from pea (*Pisum sativum*) with Cys79 replaced by serine. The protein was expressed in *Escherichia coli* with a His-tag added to the C-terminus. Monomeric and trimeric LHCIIb, bearing the pigments chlorophyl a/b and the carotenoid lutein, were provided by Prof. Paulsen. The detailed procedure of expression and reconstitution of LHCIIb and its pigments was described already elsewhere[48, 51, 102].

It is essential to exhibit a model of the detailed structure of LHCIIb in order to understand the reactions that are involved in oxidizing water to oxygen. The LHCIIb used in this study is a trimeric complex consisting of three symmetrically arranged

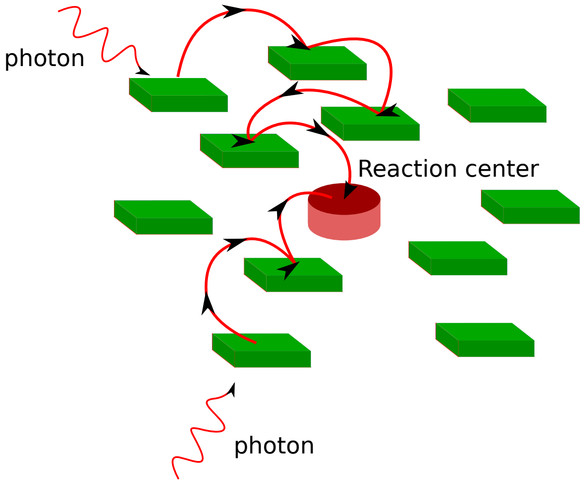

Figure 4.1: Chlorophyll molecules in the LHCII complex transfer energy from excited states of the electron to the reaction center

monomers[125]. Each monomer consists of three membrane spanning α-helices, 12 chlorophylls at minimum (7 Chl a and 5 Chl b) and 2 carotenoids. The chlorophyll molecules are arranged in two levels, one close to the upper and one close to the outer leaflet of the thylkaloid membrane. The maximum thickness of the complex, as defined by the highest residues on the stromal (outer membrane) side and the lowest one on the lumenal (inner membrane) side, 48 Å. The longest and the shortest lateral dimensions of the monomer are 48 Å and 32 Å, respectively. The chlorophylls are attached to the polypeptide by coordination of the central magnesium atom to polar amino-acid side chains or to main-chain carbonyls in the hydrophobic interior of the complex.

The absorption characteristics of the LHCIIb complex is mainly defined by the absorption spectra of the chlorophyll molecules Fig. 4.3. This chlorophyll molecules vary in their absorption characteristics, caused by varying substitutes around the porphyrin ring. Such variation in the chemical structure of the chlorophylls do considerably alter their absorption characteristics. However, there are two distinct bands in the absorption spectra of the LHCIIb Fig. **??**. One is in the blue region between 400-500 nm also called the Soret band, which can be assigned to the singlet transition $S_0 \rightarrow S_3$ of Chl a and Chl b. A second band in the red region between 550-700 nm is assigned to the singlet transitions $S_0 \rightarrow S_1$ (Q_y) and $S_0 \rightarrow S_2$ (Q_x) of the same molecules. The two absorption bands can be split further into sub-bands. Recent investigations at cryogenic temperatures[144] show that this sub-bands can be assigned to different Chl states, so

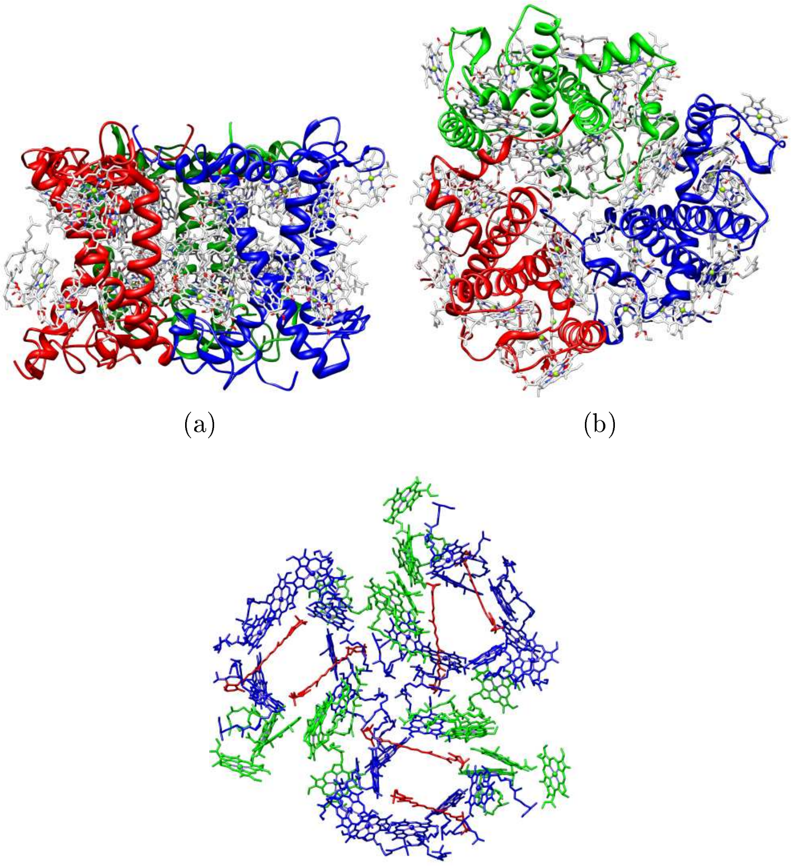

(a) (b)

(c)

Figure 4.2: The LHCIIb complex from pea in the trimeric form. The complex is presented in the BLM form (a) and from the top view (b) where the arrangement of the three monomers can be clearly seen. The chromophores (c) are presented: (green) chlorophyll a, (blue) chlorophyll b and (red) carotenoid.

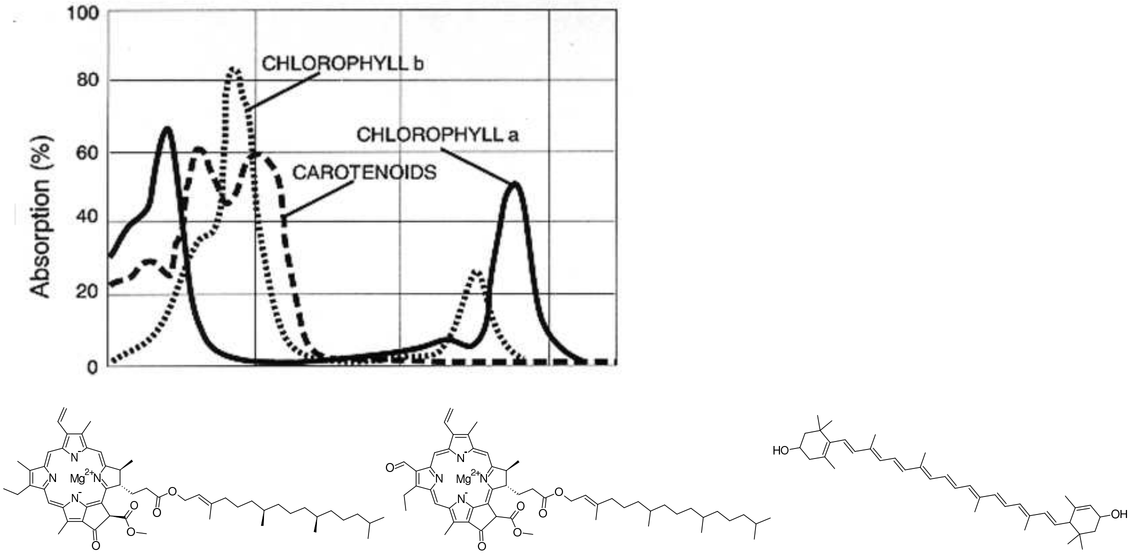

(a) (b) (c)

Figure 4.3: Absorption spectra and the corresponding molecular structures of the pigments in LHCIIb[73]. Chlorophyll a (a), chlorophyll b (b) and lutein (c).

called 'pigment-pools'. The position of the band of each Chl state is defined by the location of the individual Chl within the complex. The details of this sub-bands are out of the scope of this work and will not be discussed further. The carotenoids also contribute to the light absorption in LHCIIb in the blue band (400-500 nm). Carotenoids efficiently transfer energy to the chlorophylls, though their main functions are the stabilization of the structure of LHCIIb and, more importantly, protection of the LHCIIb complex against toxic singlet oxygen.

A simplified example of the energy transfer cascade in LHCIIb is presented in Fig. 4.4. Through absorption of photon enery $h\nu$ the Chl a/b and the carotenoids are excited into the singlet states S_n, where $n \geq 1$. The Chl a reach the excited state S_1 through internal conversion from higher excited states or through direct absorption of red photons. An electron transfer (ET) occurs from the S_1 states of Chl b or the carotenoids. It is assumed that fluorescence light emitted from LHCIIb originates solely from Chl a.

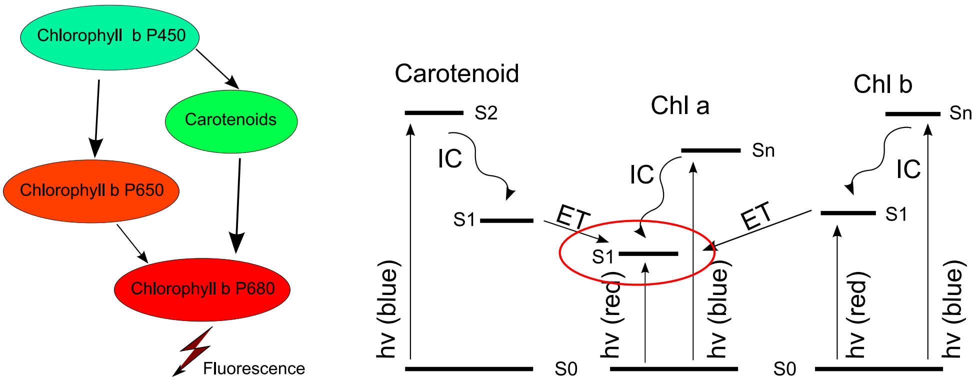

(a) (b)

Figure 4.4: A simplified schematic dipiction (a) and a level diagram (b) of the energy transfer mechanism in LHCIIb.

4.1.2 Fluorescence spectra of the LHCIIb complex

The LHCIIb trimer complexes were made by binding reconstituted monomeric LHCIIb via its His tag on a nickel-chelating fast-flow Sepharose column by sucrose gradient ultracentrifugation. For this reason the stock solutions used for preparing a ptBLM on hydrogel with LHCIIb contained a high amount of sucrose. To remove sucrose the solution was filtrated again through an appropriate membrane using PBS buffer solution having 0.05 % w/v dodecylmaltoside (DM).

Polymer coated ITO samples were prepared as described in chapter 3. P(PFPA-co-MABP) was spin-coated on DC sputtered ITO on glass. After cross-linking by UV treatment and annealing in a vacuum oven. The PFP acvtive ester in the network were than converted into NTA and OH groups. The NTA functionality were than further converted to the Ni-NTA chelate by immersion of the gel layer into a buffered $NiSO_4$ solution. The excess Ni was removed by rinsing with an acetate buffer solution (pH=4). After that a solution in detergent (DM) of LHCIIb from pea (*Pisum sativum*) with a his-tag attached to sthe C-terminus was added to the bathing solution. Unspecific adsorbed LHCIIb was removed by rinsing using PBS/DM solution. The phopholipid (DiPhyPC) solubilized in DM was added together with bio-beads. After formation of the lipid bilayer the cell was flushed using pure PBS.

Laser scanning images of the reconstituted LHCIIb were recorded. The LSM image of the LHCIIb layer in a BLM is shown in Fig. 4.5. To test whether the fluorescence does originate from immobilized LHCIIb complexes the laser focus was placed on sin-

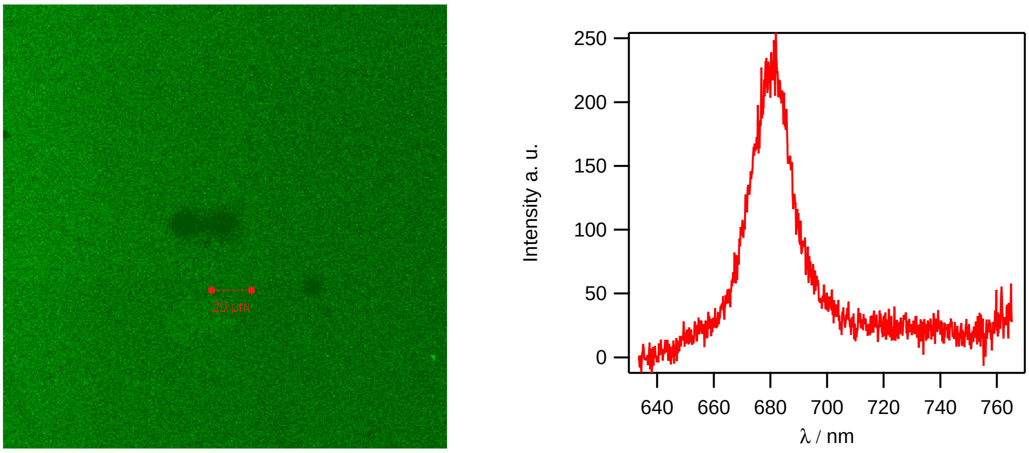

(a) (b)

Figure 4.5: Laser scanning image (LSM) (a) and example of a fluorescence spectra (b) of the reconstituted LHCIIb in a polymer supported ptBLM system on ITO. The image and the spectra were recorded using a confocal microscope. The LHCIIb complex was excited using the argon line 488 nm and emission was collected after a LP650 long pass emission filter. The bleaching spots in (a) indicate the location where the spectra (b) were recorded. The intensity in the bleached area did not change with time supporting the assumption that the LHCIIb had been immobilized on the surface.

gle spots of the scanning area and the spot was bleached using maximum power. This bleached areas are clearly seen as dark spots in Fig. 4.5b. The time dependent fluorescence intensity within the bleached areas was measured. The fluorecence intensity did not recover indicating that the LHCIIb complex was immobilized on the surface. The fluorescence spectra of the surface bound LHCIIb was also measured (Fig. 4.5b). The spectra agrees very well with fluorescence spectra of LHCIIb in bulk solutions recorded with a fluorometer. As expected the emission had a maximum at 682 nm and therefore can be assigned to the chlorophyll Chl a in the complex.

4.1.3 Potential dependent fluorescence spectra of LHCIIb

LHCIIb was immobilized as described. The square wave potential shown in Fig. 4.6a was applied to the ptBLM system (bias potential -50 mV) and the fluorescence intensity change induced by the potential step was recorded. The fluorescence spectra at each potential step was also measured.

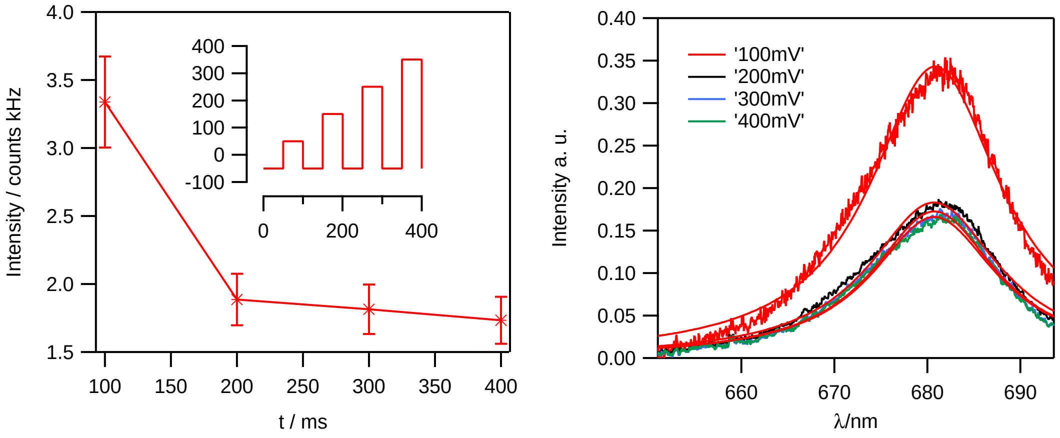

(a)

(b)

Figure 4.6: Fluorescence intensity change of the LHCIIb in a ptBLM induced by square wave potential (inset) of varying amplitude. The measurement was triggered by the rising edge of the periodic square wave pulses. The time period was 100 ms. (b) The corresponding fluorescence spectra are also shown.

As can be seen in Fig. 4.6, the intensity drops drastically with each potential step. The characteristics of the curve in Fig. 4.6a is similiar to the exponential decay of a bleaching process. The measurement was also performed after allowing a pre-bleaching time to elapse while full laser power was hold at the recording site. In any case, the intensity dropped to a very low level where the bad S/R ratio did not allow detection of change of fluorescence from LHCIIb induced by the applied potential in the ptBLM.

4.2 Potential-dependent Emission Spectra of a Potentiometric Dye in a Planar BLM

In the previous section the suitability of the fluorescating complex LHCII as a membrane potential probe was investigated. The inherent fast bleaching of the LHCIIb hinders the measurement of the fluorescence intensity change as a response to an external voltage applied to the ptBLM. Any background noise, which is considerably reducing the S/R of our measurement, can be compensated by employing a ratiometric approach. Moreover, potentiometric dyes used to stain the membrane surface can also serve as a probe for the electric field around the membrane. There have already been numerous reports of specifically designed dyes for the direct measurement of membrane potentials, particularly in the field of neuroscience[27, 30, 94, 97, 98]. Here, the dye di-8-butyl-amino-naphthyl-ethylene-pyridinium-propyl-sulfonate (di-8-ANEPPS) was chosen. The membrane potential of a tBLM and a ptBLM induced by a defined external voltage was measured by ratiometric fluorescence spectroscopy.

4.2.1 The styrle dye Di-8-ANEPPS

Di-8-ANEPP is an amphiphilic, fast-responsive staining dye for cell membranes and belongs to the group of voltage sensitive, or rather potentiometric dyes. Because of its sensitivity to the spatial and temporal variations of the membrane potential $\Delta\phi_m$ respectively electric field $\vec{E}$ along the surface of a cell membrane, it has been frequently used in neuroscience to monitor neuronal electrical activity. To understand the mechanism that underlies the sensitivity of the dye to changes of the electric field, one has to consider the design of the molecule[76].

According to its molecular structure depicted in Fig. **??** the dye is attributed to the styryl or naphthylstyryl class of molecules. The hydrocarbon chain acts as an anchor to the lipid membrane whereas the chromophore has a highly localized, well exposed

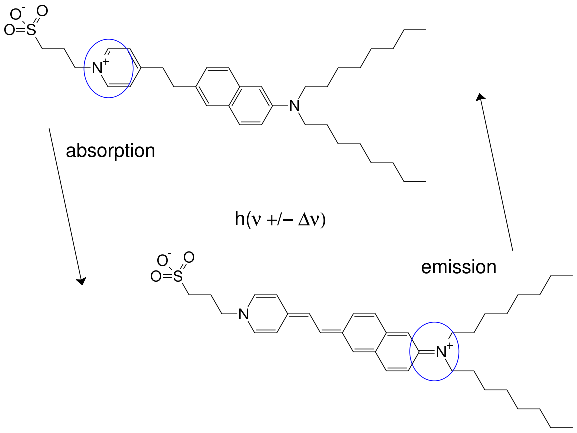

Figure 4.7: Molecular structure of the potentiometric dye di-8-ANEPPS and excited state intra-molecular redistribution of the positive charge.

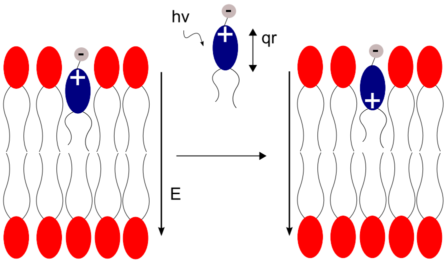

Figure 4.8: Location of di-8-ANEPPS in a lipid membrane shown schematically. The excited state dipole moment $q\vec{r}$ of di-8-ANEPPS in the membrane is parallel to the intramembrane electric field $\vec{E}$.

ground-state charge at the pyridium nitrogen and a compensating negative charge in the sulfate group. The favored orientation of the chromophore in the lipid membrane is close to the aqueous phase so that the molecule is aligned perpendicular to the membrane surface. Excitation induced charge redistribution $q\vec{r}$ from the pyridium nitrogen to the aminophenyl end of the chromophore will occur parallel to the electric field $\vec{E}$ of the membrane (Fig. 4.8).

According to

$$h\Delta\nu = -q\vec{r} \cdot \vec{E} \tag{4.1}$$

where h is the Planck constant, the interaction of the electric dipole moment of the excited state with the electric field of the membrane will cause a direct electrochromic shift $\Delta\nu$ of the absorption and fluorescence spectra of di-8-ANEPPS. As Eqn. 4.1 also shows, the maximum shift will occur if the charge redistribution is parallel to $\vec{E}$ which is exactly the case here.

In general, it is difficult to devise a figure of merit for the optical detection of $\Delta\nu$. The signal strength depends very much on the staining conditions. For fluorescence, this can be overcome by detection of relative changes of the emitted light spectra, whereby background fluorescence from stained, non-responsive parts of the membrane have to be limited. If precautions have been taken accordingly, one can find that the relative change $\Delta F/F$ of the emitted intensity, for example in voltage-clamped cell membranes stained using DI-8-ANEPPS is within 5-10 % for a 100 mV potential step[19, 56, 75, 142].

4.2.2 Fluorescence emission and excitation spectra of Di-8-ANEPPS

The absorption and fluorescence spectra of di-8-ANEPP had been investigated extensively before. It had been found that di-8-ANEPPS had an absorption band at 450-550 nm with an extinction coefficient of $4 \cdot 10^4$ when membrane bound. The Stokes shift of the emission maxima is within 100-150 nm [36, 43], which makes di-8-ANEPP suitable for applications in highly scattering preparations. The fluorescence quantum yields are about 0.3 for the membrane bound dyes and a factor of 100-1,000 times less in water. For this reason, given that the binding of the dye to the membrane is strong enough, background fluorescence from unbound dye can be neglected under most experimental conditions.

To confirm the reported spectral characteristics of di-8-ANEPPS, fluorescence excitation and emission spectra were measured in two different environments; first the dye was dissolved by dilution of a di-8-ANEPPS/methanol stock solution in PBS. Second, di-8-ANEPPS was incorporated into lipid vesicles of 100 nm diameter. The vesicles were produced by extrusion using a suspension of DiPhytPC and di-8-ANEPPS in PBS.

After preparation of each solution fluorescence excitation spectra with the emission monochromator set to 630 nm and emission spectra with the excitation set to 488 nm were recorded (Fig. 4.9). The excitation wavelength was chosen according to the Ar laser line used in later experiments. For the di-8-ANEPPS stained vesicles in PBS the maximum of excitation is at 467 nm and that of the emission spectra within 583-589 nm. Whereas in the case of freely diffusing di-8-ANEPPS solubilized in PBS the

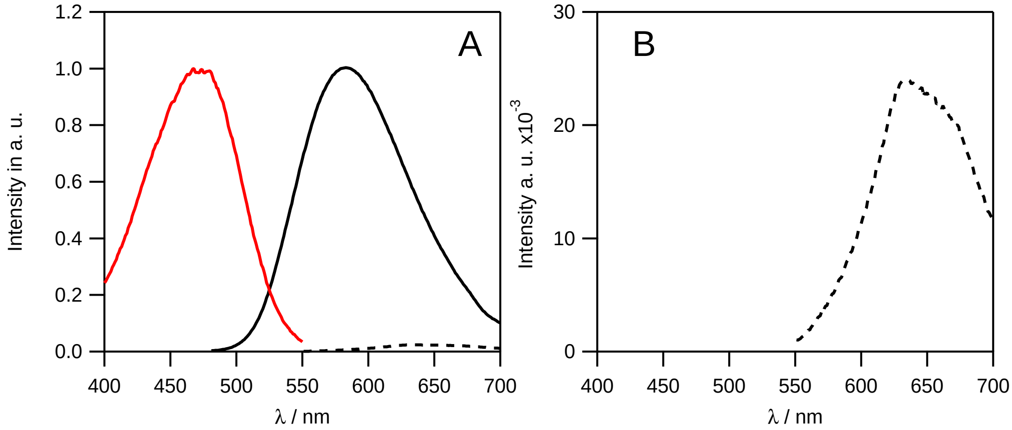

Figure 4.9: (A) Fluorescence excitation spectra (red) and emission spectra (black) of di-8-ANEPPS in PBS (dashed line) and DiPhytPC vesicles (solid line). The intensities are normed to the maximum of the spectra recorded in vesicles. (B) Zoom of the dashed curve in (A). Configuration of measurement; excitation spectra with the emission monochromator set to 630 nm and emission spectra with excitation set to 488 nm. Fluorescence intensity of di-8-ANEPPS in bulk solution is two orders of magnitude less than in lipid vesicles.

emission maximum was within 636-651 nm.

The spectra show that the fluorescence intensity of the probe bound to the membrane was by two orders of magnitude higher than in the unbound state. The maximum shifted to the blue wavelength range by 50 nm in accordance with the findings reported before for an analog membrane probe[40, 74, 77]. The shift originates from the preferred orientation of the dye within the membrane and can be explained by the differential solvation which is absent in a homogeneous solution. In the ground state the positive charge (Fig. 4.7) is centered in the pyridium ring and is surrounded by the polar head groups of the lipids. Thus, the ground state stabilization is comparable to the situation in a polar solvent. Upon excitation the charge is pushed into the hydrophobic region of the membrane where the vertical excited state is raised above its initial energy state in a polar solvent environment, thereby causing a blue shift of absorption and emission spectra.

Correspondingly the Stoke shift in an anisotropic medium like a membrane is lower than in the bulk solvent. In bulk solution the solvent molecules surround the dye. If di-8-ANEPPS is excited the solvent molecules undergo fast reorientation (20x shorter time scale than fluorescence lifetime) upon alteration of the electronic configuration of the dye. This lowers the energy level of the excited state significantly and is the underlying reason for a higher Stokes shift in a polar solvent. If the effective degree of freedom is reduced, e. g. a confined environment like a lipid membrane, reorientation is limited and, thus, a lower Stokes shift is expected as seen in Fig. 4.9

4.2.3 Ratiometric fluorescence spectroscopy

Various techniques have been implemented to date to measure membrane potentials[6, 41, 42]. Very often, the relative fluorescence intensity $\Delta F/F$ following the potential change is used as the quantity of measurement, that is the fluorescence intensity variation ΔF as normalized to the average fluorescence F at a reference potential. Yet, $\Delta F/F$ is not suitable for the determination of absolute potential value in mV. The reason is, that the relative change $\Delta F/F$ is not comparable for different preparations, or even at different points within the same preparation. Variations in staining condition, bleaching or signal strength do not allow the direct calculation of $\Delta\phi_m$ out of $\Delta F/F$ values

One way around is the ratiometric approach. Instead of using absolute values from integrated fluorescence intensities over one band, the ratio R of two distinct wavelength regions of the same band can be used as a measurement parameter. The advantage of this technique is that all interfering sources of noise that affect the whole spectra are thereby canceled out. This means that the ratio R is insensitive to bleaching, staining or laser fluctuations. Thus, the signal to noise ratio S/R is considerably enhanced, which is necessary as most of the potential sensitive dyes, including di-8-ANEPPS, commonly have a very low signal response in all experimental setups, $\Delta F/F$ (usually 5-10 % maximum). Sometimes the signal strength is not far from the fluctuation of the excitation light source.

An analog method[18] was applied here to measure the response of di-8-ANEPPS to membrane potential changes (Fig. 4.10). The spectral regions selected to form a intensity ratio are found on the blue and the red side of the $\Delta F/F = 0$ point at λ_0, which is the potential insensitive point in the spectra (Fig. 4.12). The ratio R is then formed by

$$R = \frac{\Delta F/F_{<\lambda_0}}{\Delta F/F_{>\lambda_0}} \tag{4.2}$$

where $\Delta F/F_{<\lambda_0}$ is the relative intensity change in the spectral region below λ_0. $\Delta F/F_{>\lambda_0}$ is the relative intensity change above λ_0. Depending on the sign of the field the fluorescence spectra of the dye is shifted to the blue or to the red side. The intensity in either side of the spectra changes in opposite directions. That is why R is not only corrected for noise, but also the strength of the signal is increased and consequently the sensitivity.

For that purpose a modified confocal microscope setup was established (Fig. 4.11). The excitation light was directed towards a primary dichroic mirror, separating the excitation and emitted light. The emitted light was further divided into two spectral parts using the second dichroic mirror. In each beam path the light passes an emission filter of appropriate choice and a pinhole before it is finally detected by APDs. A combination of various emission filters were tested in terms of S/R and signal strength before a final choice was made. If the fluorescence intensity was too low, the pinhole diameter was increased appropriately in order to increase the detection volume within the sample, in those cases, the microscope was not operated in the confocal mode anymore. The details of the chosen combination of dichroic mirror and emission filters are explicated in Fig. 4.11. The relative intensities I_1 and I_2 of the emitted light in each path were further processed offline by formation of the ratio R, digital filtering and normalization to the reference potential $\Delta\phi_0$.

The region of interest of the emission spectrum of di-8-ANEPPS defined by the selected combination of emission filter/dichroic mirror is presented in Fig. 4.12 using the difference spectrum calculated from the examplified spectral shifts in Fig. 4.11.

An external voltage $u(t)$ was applied to the planar electrode support through a waveform generator and connected to a potentiometer using a three electrode configuration described before (**??**). The time dependent fluorescence response of the dye to $u(t)$ was measured. However, before analyzing the results preliminary considerations have to be taken regarding the response of $\Delta\phi_m(t)$ to u(t).

The aim of this work (see section 1.3) is to relate quantitatively the membrane potential induced by u(t) in a ptBLM to the fluorescence intensity change. The self-generated $\Delta\phi_m(t)$ is a potential difference across the membrane. In the ptBLM geometry, where a sub-membrane space below the lipid/protein layer adjacent to the working electrode exists, this potential difference is not necessarily equal to the applied voltage u(t). However, calculations based on a electrical network model and using the electrical parameters derived from EIS measurements in chapter 3 provide

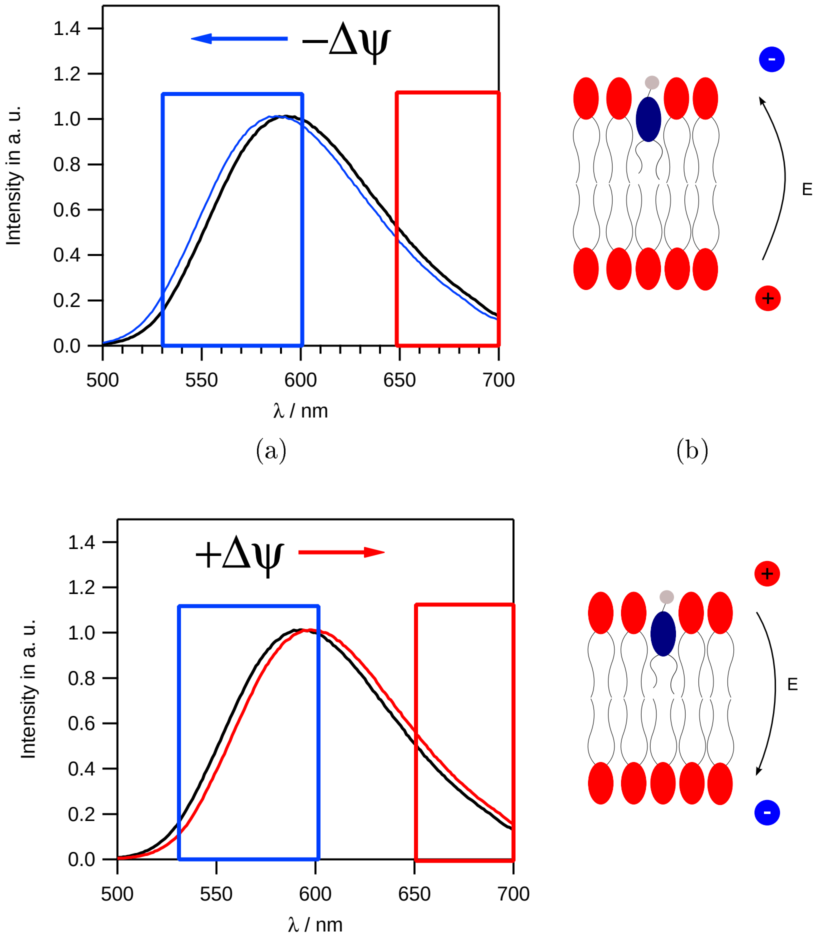

(a) (b)

(c) (d)

Figure 4.10: Spectral shifts of the emission of di-8-ANEPPS presented schematically for a random membrane potential $\Delta\psi$. The graphs (a) and (c) show the shift upon (b) depolarization and (d) hyperpolarization. E is the field gradient of the transmembrane potential $\Delta\psi$.

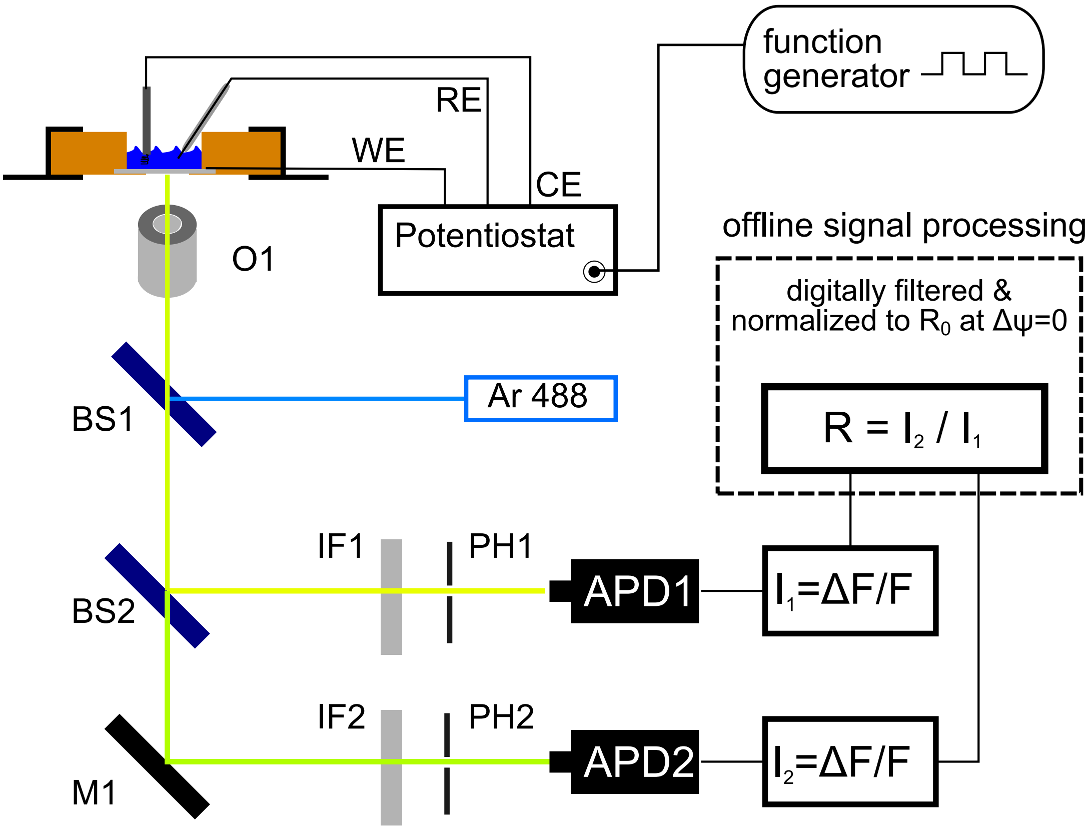

Figure 4.11: Depiction of the ratiometric fluorescence spectroscopy setup; excitation light used was the 488 nm line of an Ar Laser, BS1 primary dichroic mirror HFT488, O1 water immersion objective 40x/1.2NA, BS2 secondary beam splitter NFT 635, M1 mirror, IF1 interference filter BP 530-600, IF2 interference filter LP 650, PH1/PH2 pinhole, APD1/APD2 avalanche photodiode; the electrochemical cell, WE transparent working electrode, CE counter electrode, RE reference electrode; the resting potential $\Delta\phi_0 = 0$.

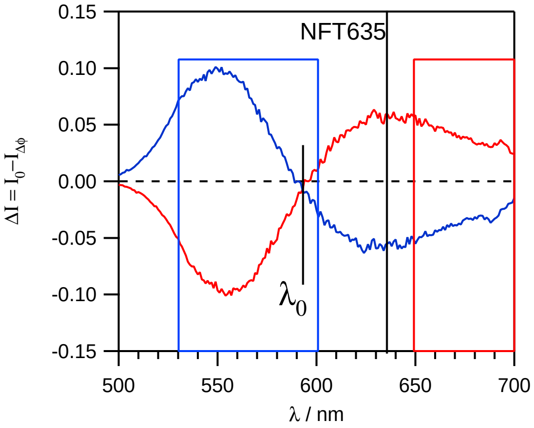

Figure 4.12: Difference spectrum of the spectral shift in Fig. 4.10. The color code for the shift direction is analog to Fig. 4.10 The transmission band of the emission filters IF1/IF2 in Fig. 4.11 are presented as blue and red boxes, also indicated is the the secondary dichroic mirror from the setup in Fig. 4.11 (solid line at 635 nm).

$\Delta\phi_m(t)$ values for a defined u(t). This model calculations are now described in detail.

4.2.4 The response of the transmembrane potential in a planar BLM to an external voltage

The rise time for the membrane potential following a voltage waveform, e. g. a square wave applied directly across the membrane employing a voltage clamp or planar electrode configuration, is determined by the product of the membrane resistance and capacitance and is therefore usually in the ms time domain and independent of geometry. If the waveform of the external signal u(t) has a frequency far enough above the time constant of the RC equivalent of the membrane, the membrane potential $\Delta\phi_m(t)$ follows instantaneously the voltage signal. The phase shift between u(t) and $\Delta\phi_m(t)$ is negligible.

This simplified view is true for many cases, though the charge transfer processes in a real lipid bilayer and its effect on $\Delta\phi_m$ can not be modeled using simple passive circuit elements like resistors and capacitors. Even in the simplest configuration like the tethered BLM, where potential dependent passive ion transport through the membrane not mediated by any protein occurs, a different model accounting for the kinetics of ion transport is required. An attempt had been made in this regard to use potential dependent rate equations, however, this model was not able to incorporate the electric field and the concentration gradients throughout the system. Hence, a model that also includes mathematical formulation of the transport process across the membrane beside the passive circuit elements has been developed. This model adopts a more general approach utilizing the integrated Nernst-Planck equation instead of focusing on particular mechanisms. In

$$\Phi_i = P_i \Psi \frac{c_{i,1} \exp \Psi - c_{i,2}}{\exp \Psi - 1}; \quad \Psi = \frac{z_i F \Delta\phi_m}{RT} \tag{4.3}$$

the flux Φ_i of the ith ion is related to the permeability coefficient P_i, the ion concentrations $c_{i,1}$ and $c_{i,2}$ on either side of the membrane and the membrane potential $\Delta\phi_m$. Moreover, z_i is the charge number and R, T, F the usual constants. The current density j_i is then described by

$$j_i = z_i F \Phi_i \tag{4.4}$$

and the time dependence of the membrane potential can be calculated from

$$\frac{d}{dt}\Delta\phi_m = (J - \sum_i j_i)/C_m \tag{4.5}$$

where J denotes the electrical current density running through the system and detected by the measurement device, C_m is the membrane capacitance.

The model was expressed in a electrical network presentation, where the parameter values described are assigned to the network elements. An electrical simulation program written in SPICE (Simulation Program with Integrated Circuit Emphasis) was used to investigate the time trace of $\Delta\phi_m$ following a voltage waveform. The detailed description of the SPICE model and simulation procedure, which was developed in our group is presented in[113].

The time dependent change of $\Delta\phi_m$ in a tBLM on ITO (section 3.2.3) was analyzed using the SPICE simulation program. A voltage square wave

$$u(t) = u_{bias} + \frac{u_0}{2}\{1 + \mathrm{sgn}(\sin t)\} \tag{4.6}$$

using a bias potential u_{bias} and amplitude u_0 was implemented. For the network elements averaged values of the fitted parameters in chapter 3 were used. The values from 3.2.3 were assigned in first place; membrane capacitance C_m=12 $\mu F/cm^2$, elec-

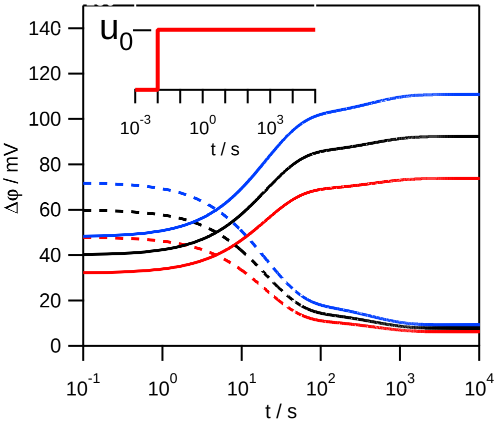

Figure 4.13: Example of the simulated potential differences $\Delta\phi_m$ (dashed line) and $\Delta\psi_{sr}$ (solid line) during re-equilibration of ions at different potential steps u_0 (inset); u_0 is (red) 80 mV, (black) 100 mV and (blue) 120 mV.

trolyte resistance R_{el}=100 Ω·cm^2. C_{sc} was set to 15 µF. The geometrical parameter V_{sr}, volume of the spacer region, was estimated to be 0.22 $^{\mathrm{nL}}/_{\mathrm{cm}^2}$. KCl was used to prepare a phosphate buffer solution (PBS), thus, the charge numbers of the ions K$^+$ and Cl$^-$ were

$$z_K = 1 \qquad z_{Cl} = -1$$

and the bulk concentration

$$c_K = c_{Cl} = 0.1\,\mathrm{M}.$$

The temperature was set to 25 ℃, further parameter settings are described in the appendix[113].

The distribution of potential differences across the layered structure following the application of single step potentials using different u_0 at u_{bias}=0 was analyzed (Fig. 4.13). Only in a short initial phase, before any appreciable ion transport does occur, the applied potential drops mainly across the lipid membrane, $\Delta\phi_m$, as intuitively expected from the lower capacitance of the membrane compared to that associated with the spacer region, and the high resistance of the lipid bilayer. The potential differences

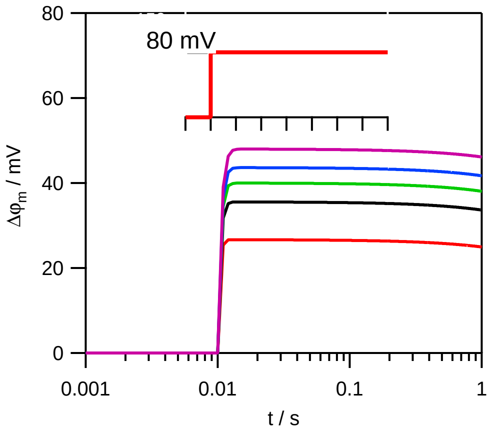

Figure 4.14: Simulation of the fast initial phase of the $\Delta\phi_m$ built up at varying spacer region capacitance C_{sr}; (red) 5 µF, (black) 8 µF, (green) 10 µF, (blue) 12 µF and (purple) 15 µF. The membrane capacitance was 12 µF. The peak value of the potential difference is determined by eq. 4.7.

formed in the fast initial phase $\Delta\phi_m$ and $\Delta\phi_{sc}$ are determined by

$$\Delta\phi_m = u_0 \frac{C_{sr}}{C_m + C_{sr}} \tag{4.7}$$

$$\Delta\psi_{sr} = u_0 \frac{C_m}{C_m + C_{sr}} \tag{4.8}$$

In the course of the repartitioning of ions the distribution of potential differences is shifted towards the spacer region and, after equilibration of the ions, almost all of the applied potential drops across the capacitance C_{sr} which accounts for the balance of charges at the electrode surface. The overall process of repartitioning is biphasic and takes course within time ranges of up to 12 h.

In a second step, the initial phase in the time trace of Fig. 4.13 was further analyzed. In Fig. 4.14 the response of the membrane and spacer region potential difference, $\Delta\phi_m$ and $\Delta\phi_{sr}$ to a voltage step u_0 of 80 mV, is presented. After a fast built up to the maximum value determined by eq. 4.7, no significant change in $\Delta\phi_m$ and $\Delta\phi_{sr}$ could be observed.

Therefore, in order to allow the membrane potential to instantaneously follow a periodic voltage signal, the frequency of the applied signal has to be chosen appropriately, i. e. the time period of the signal has to be short enough, so that repartitioning

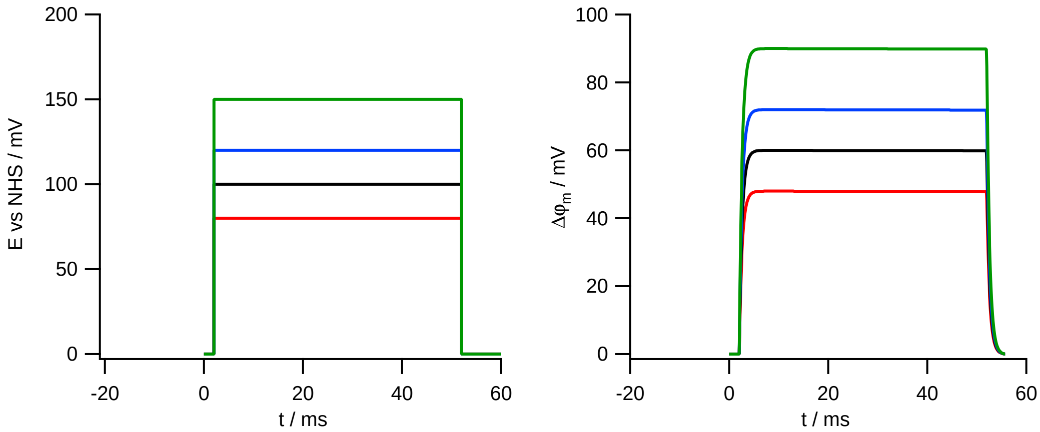

Figure 4.15: Example of the simulated response of potential differences $\Delta\phi_m$ to a square wave voltage with varying amplitude u_0. The amplitude of the external voltage; (red) 80 mV, (black) 100 mV, (blue) 120 mV and (green) 150 mV. The membrane capacitance was set to 12 µF and that of the spacer region 15 µF

of ions can be neglected. On the other side, the time length of a series of voltage pulses needs to be long enough compared to

$$\tau = R_{ex}(C_m + Csc) \tag{4.9}$$

since the membrane potential $\Delta\phi_m$ must built up to its maximum value and the pulse to pulse variation should be kept low.

In Fig. 4.15 the applied square wave voltage u(t) and the response $\Delta\phi_m$ of the SPICE model circuit to u(t) are shown as an example. The frequency and bias potential of the applied external voltage are 10 Hz and 0 mV respectively. The amplitude u_0 was varied between 80 mV, 100 mV, 120 mV and 150 mV. The membrane potential $\Delta\phi_m$ rises with a single exponential and the time constant is determined by the conductivity of the buffer solution and the overall capacitance consisting of C_{sr} and C_m. The membrane potential builds up to reach 42 mV at u_0=80 mV, 52 mV at u_0=100 mV and 62 mV at u_0=120 mV. At the trailing edge of the applied square wave the process reverses and $\Delta\phi_m$ drops down to zero.

The simulations show that passive ion transport through the membrane has to be considered, if the time period of the applied periodic voltage signal is within the time range where repartitioning of ions has an effect on $\Delta\phi_m$. For the experiments described now 10 Hz square wave signals of the form eq. 4.6 were applied to the tBLM and gel supported ptBLM on ITO. Hence, the repartitioning of ions causing a decrease of $\Delta\phi_m$ could be neglected. $\Delta\phi_m$ and accordingly the fluorescence signal should follow the time trace of the external command voltage as derived from the simulations in (Fig. 4.15).

4.2.5 Fluorescence spectra of the di-8-ANEPP dye in a tBLM

The potentiometric probe di-8-ANEPPS was used to measure the potential induced by a square wave voltage applied to the tBLM on ITO. The model membrane was presented in section 3.2.3. In the experiments described now, modulation of dye fluorescence was recorded utilizing the ratiometric technique.

Stock solutions of di-8-ANEPPS were prepared in a MeOH/DMSO (9:1) solution containing Pluronic-F127 (0.05 % v/v) and stored at 4°. The tBLM was stained 30 min by introduction of 20 mM di-8-ANEPPS. Excess dye was removed by several washes using PBS. The excitation wavelength was 488 nm. The resting potential, the bias of the voltage signal, was kept constant at u_{bias}=-80 mV throughout the whole experiments.

The amplitude u_0 of the square wave signal was set to 120 mV. From the discussion in section 4.2.4 it was concluded that the actual potential difference over the membrane in planar BLMs strongly depends on the parameters of the system such as the spacer region capacitance. For that reason, SPICE simulations were conducted to calculate the actual membrane potential $\Delta\phi_m$ in our system for each amplitude using the resistance and capacitance values derived from EIS measurements (section 3.2.3). According to this data the 120 mV potential step of the external voltage from -80 mV bias would correspond to a $\Delta\phi_m$ step from -50 mV to +70 mV. However, from now on potentials stated in this section refer to $\Delta\phi_m$ calculated from the applied voltage, i.e. the setting at the waveform generator (u_{bias} and u_{bias}), as described in the previous section.

The fluorescence intensities in the blue and the red region of the spectra were recorded. A multistage signal processing scheme was performed afterwards for ratio formation and noise reduction (section 4.2.3). Briefly, the emitted light was separated into two 'channels' using a beam splitter (635 nm). The light guided to a band

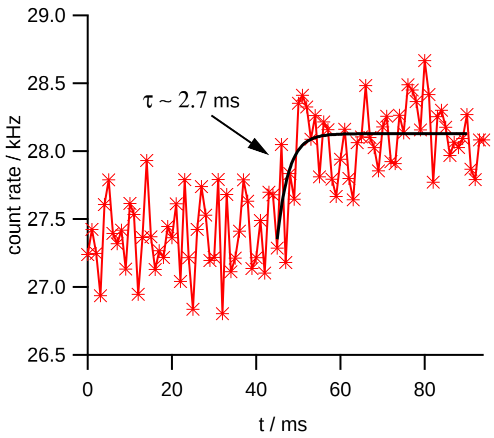

Figure 4.16: The rising edge of a single membrane potential pulse. The edge was fitted using a single exponential function (red line).

pass filter (530-600 nm) is denoted as the 'blue channel', whereas in the 'red channel' light is guide through a long-pass filter (650 nm). The two fluorescence signals were captured by a pair of equivalent APDs. Each of these detectors was simultaneously sampled during the time the laser beam dwells at a particular recording site. These measurements were then digitized and a ratio was formed between these corresponding observations. Each of the two fluorescence signals contains all fluctuations originating from background sources and were conveniently removed during the ratio formation process.

In Fig. **??** an example of the modulated fluorescence intensity $\Delta F/F$ of di-8-ANEPPS is presented. The response to an oscillating electric field could be detected by signal averaging. The time trace was derived by averaging of 300 independent recordings, each having a length of 1 s. The sign of the response depends on whether the dye is located in the outer or inner leaflet of the membrane. In our case, where di-8-ANEPPS is located in the outer leaflet, the fluorescence intensity change in the red channel and the square wave signal are expected to be of the same sign, which is also reflected by the data in (Fig. 4.17b). The trace of the optical signal follows a single exponential function. In many cases, the system is adequately described by a RC equivalent circuit, the time constant is 3 ms for the tBLM in Fig. 4.16. The kinetics are independent of dye concentration but do depend on KCl concentration since this controls R_e in (4.9). The slope of the membrane hyperpolarization and depolarization (Fig. 4.16) was fitted using single exponential $exp(-t/\tau)$. The value obtained, 2.7 ms,

u_0 / mV	R_n
30	0.022 ± 0.03
50	0.03 ± 0.032
80	0.048 ± 0.036
120	0.067 ± 0.034

Table 4.1: The change of the ratio R_n in a tBLM at different amplitudes u_0 of the square wave voltage. The bias potential was at -50 mV.

is within the range calculated for the tBLM on ITO.

The size of the response $\Delta F/F$ was typically 5 % of the total transmitted light signal at 488 nm excitation for a +120 mV potential step (Fig. 4.17). But this relation between membrane potential and $\Delta F/F$ was inconsistent if compared for different samples, or different recording sites of the same sample. This trial-to-trial variation was reduced when the ratio R was formed between the red channel and the blue channel (Fig. **??**). However, in similar studies on cell membranes it was found that, there was a considerable variability in the absolute magnitude of R. The results became much more consistent in this regard, if a normalized parameter R_n was introduced. It is formed by subtraction of a reference value R_0 at 0 mV membrane potential from the measured signal R. Under our experimental conditions, R_n can be used to infer absolute potential changes.

$$R_n = R - R_0 \tag{4.10}$$

R_n was formed in the experiments described here for varying amplitudes u_0 of the external square wave voltage and a bias potential of -50 mV (Fig. 4.18b). The results show a linear relation between R_n and the membrane potential $\Delta\phi_m$. Using this values the conversion factor of R_n to mV could than be determined from the linear fit. Under our experimental conditions the factor was 0.03-0.05 per 100 mV potential change and considerably lower than the values reported for similar experiments on lipid bilayer of different geometry[59]. The limit of detection (LOD) was reached at 30-50 mV, where the R_n value was close to the background noise level.

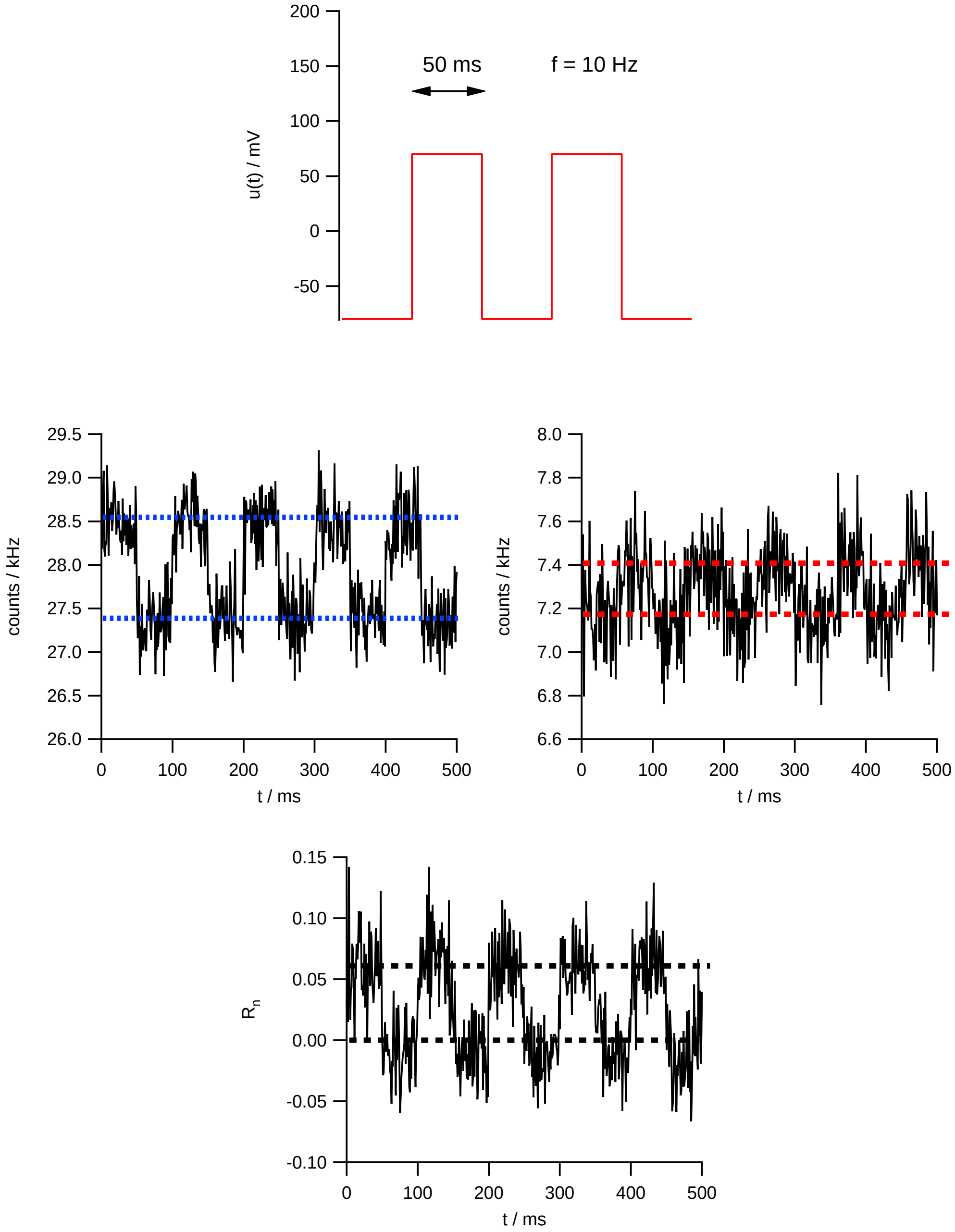

Figure 4.17: The ratiometric membrane potential signals according to the signal processing scheme described in the text. (a) The membrane potential is induced by external square wave voltage with an amplitude of 120 mV and a bias potential of -80 mV (see eq. (4.6)). (b) The fluorescence change of the red (>635 nm) and (c) blue channel (<635 nm) was recorded (see section 4.2.3). (d) A ratio R was formed from these signals and the normalized value R_n was calculated.

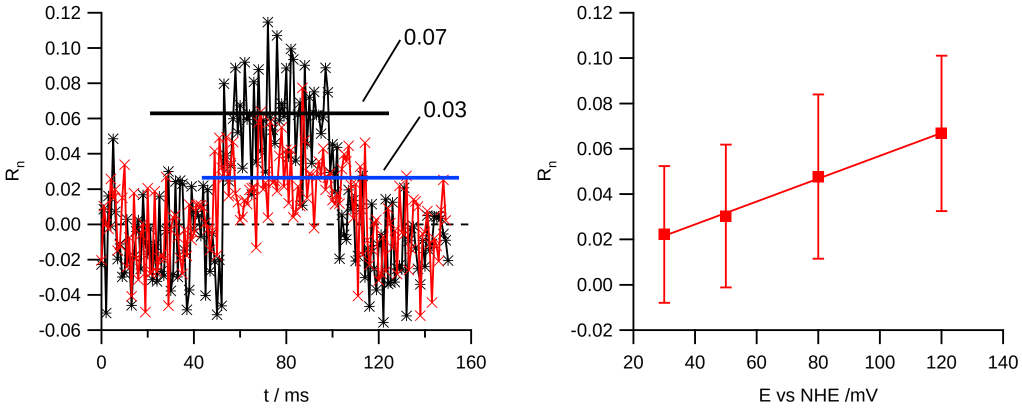

Figure 4.18: The change of the ratio R_n in a tBLM on ITO at different amplitudes u_0 of the applied square wave voltage. (a) An example showing the square wave pulse for u_0 120 mV (black) and 30 mV (red). Resting potential was -50 mV. (b) The values are averages of ten square wave pulses and the error bars indicate the resulting standard deviation of R_n at each voltage, which was always around ±0.03 (Tab. 4.1).

4.2.6 Membrane potential in a ptBLM measured by ratiometric fluorescence spectroscopy

The feasibility of the ratiometric emission spectroscopy for the measurement of the membrane potential in planar membrane systems was shown by means of a tBLM on ITO. Using the same experimental conditions the membrane potential in a ptBLM was measured.

The dye Di-8-ANEPPS is incorporated only into the lipid bilayer patches formed between the proteins. For that reason, it was expected that the total emitted intensity in a ptBLM will be considerably lower compared to the measurements in a tBLM, where 100 % of the layer consists of lipids and, hence, the bilayer is stained to a higher degree. Even though R_n should be independent of staining condition, in general, this would somehow result in a decreased S/R and a lower sensitivity of our ratiometric measurement to potential changes in a hydrogel-supported ptBLM compared to those in the tBLM.

The samples were prepared according to the procedure described in the previous section. An identical setup for the ratiometric approach was used and the voltage signal had a frequency of 10 Hz. The capacitance of the spacer region, which is formed

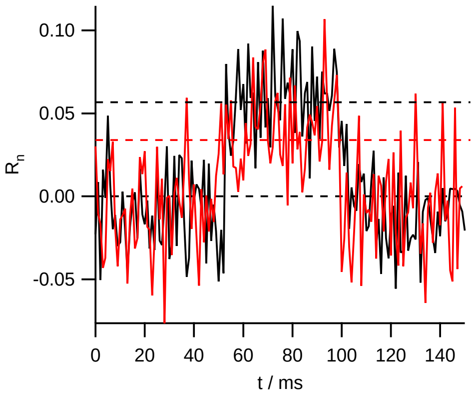

Figure 4.19: Time traces of R_n for a ptBLM (red) and tBLM (black). The square wave voltage applied had an amplitude of 120 mV and a bias of -50 mV. The dashed line indicate the zero level and the magnitude of each signal.

by the hydrogel support increases drastically compared to the short linker monolayer in the tBLM, due to the uptake of water. This was taken into account when the external voltage bias was applied to the system. In order to be able to compare the results from the tBLM with those from the ptBLM system, the effective membrane potential applied should have equal magnitudes. Because of the high water amount in the gel, it was assumed that the potential applied will almost completely drop over the membrane, contrary to the tBLM case, where a low capacitance of the spacer region causes a lower potential difference over the membrane. Consequently, the bias u_{bias} in eq. (4.6) was hold at -50 mV during this experiment.

The magnitude of R_n at 120 mV was 0.05. The time constant of the membrane depolarization and hyperpolarization, i.e. the edges of the square wave voltage pulse, was derived from the time trace of R_n by least squares fit using a single exponential function. The result 2.3 ms is close to the calculated value eq. (4.9). The potential step u_0 was also varied from 80 mV to 120 mV. However, because of the low S/R of the measurements in a ptBLM the sensitivity was also low. In order to determine the absolute voltage resolution in our system, the smallest resolvable voltage step was recorded. The criterion was that the resulting step in R_n could be clearly separated from a baseline at -50 mV. The smallest potential change detectable was 80 mV.

u_0 / mV	R_n
80	0.005 ± 0.044
120	0.029 ± 0.049
150	0.05 ± 0.044

Table 4.2: The values of R_n in a ptBLM at different amplitudes of the square wave potential. The bias potential u_{bias} was set to -50 mV

4.3 Summary

In summary, fluorescence spectroscopy was performed on hydrogel-supported ptBLMs. The fluorescent LHCII was used in a first place to form the ptBLM. Emission spectra of LHCII were measured and it was shown that the spectra was comparable to those recorded in bulk phase. The data showed that fluorescence spectroscopy could be applied on the hydrogel-supported ptBLM on ITO with high sensitivity. The LHCII was then tested as a probe for the membrane potential. However, strong bleaching effects did not allow detection of changes in membrane potential differences. Hence the potential sensitive dye Di-8-ANEPPS was used. Di-8-ANEPPS was incorporated into the lipid bilayer patches formed between CcO. Membrane potential changes were measured by ratiometric emission spectroscopy. Potential changes with down to 80 mV, i.e. the smallest resolvable potential change, could be detected. The absolute voltage resolution was lower compared to the reference measurements in tBLM. This could be explained by the smaller lipid amount in the ptBLM. A conversion factor of 0.05 in R_n per 100 mV was derived from the tBLMs on ITO as a reference system. The results prove that the important parameter $\Delta\phi_m$, not accessible by electrophysiological approaches on planar membrane systems like the ptBLM, can be measured by fluorescence spectroscopy.

Chapter 5

Conclusion and Outlook

The ratiometric fluorescence technique was shown to be a general approach for the measurement of the potential difference $\Delta\phi_m$ across the lipid membrane in a protein-tethered BLM induced by externally applied voltage. The results derived from these measurements can be used as a basis for future investigation of the self-generated $\Delta\phi_m$ of CcO in a ptBLM.

In order to be able to apply the ratiometric fluorescence spectroscopy simultaneously with electrochemical measurements a new functionalization strategy for the ptBLM on ITO had to be developed, which is different from the previous one for novel metal substrates. The ITO layers commercially available proved to be inappropriate for this purpose. The electrical properties and the surface morphology were not reproducible. Consequently, the work started with the optimization of the ITO layer properties using different sputtering parameters. The surface pattern of these layers showed small spikes with a height of 10-15 nm and a sheet resistance of 15-20 Ω/sq. EIS and CV measurement on bare ITO using a redox species proved that such a low sheet resistance is an important feature for the application of electrochemical techniques on ITO. Further, the optimized sputtering parameters provide reproducible results regarding the layer properties. Thus prepared ITO layers can be functionalized for protein immobilization, for example to form the ptBLM on the electrode surface.

However, the ptBLM system had not been established yet on oxidic surfaces like ITO. Therefore, silicon wafer were used as a well defined test substrate. The first functionalization method employed silanization of the electrode surface. A custom made NHS-silane was used. The ptBLM on NHS-silane modified silicon was prepared.

EIS data showed that a ptBLM could be formed on the naturally grown silicon dioxide layer on the wafer. The same conditions for silanization using NHS-silane were used for the ITO substrate. A ptBLM was than formed on ITO. The activity of the *cytochrome c oxidase* from *P. denitrificans* could be detected by cyclic voltametry using its substrate *cytochrom c* in the reduced form, though the catalytic current proved to be small compared to a similar system on gold. The reason for the weak activity is an imperfect lipid bilayer formation on ITO, which can be explained by the high surface roughness of the ITO with spikes covering the entire surface. The short linker molecule to the solid support had no 'smoothing' effect. This drawback can be overcome by a soft macromolecular support instead of the short linker molecules.

A new approach in the direction of polymer-supported BLM is the hydrogel- supported ptBLM. A thin hydrogel P(HEAAm-co-NTAAAm-co-MABP) layer is used as a soft 'cushion' on indium tin-oxide (ITO), providing a smooth, functional surface to form the ptBLM. The gel-support with mesh sizes smaller than the size of the protein was shown to result in very robust planar lipid bilayers, exhibiting good electrical sealing properties (1-5 MΩ·cm^2). Cytochrome c oxidase could be easily incorporated in a functionally active form. Furthermore, the use of ITO as a conducting and wave guiding substrate allowed us to address the question of the anisotropy of the surface layers. A well-ordered lipid bilayer should exhibit different optical properties in different spacial directions. The same argument holds to a lesser extent for an ordered and oriented protein monolayer. The experimental proof of this anisotropy is hard to achieve and hence information about the proper arrangement of a protein/lipid layer is scarce.

Owing to their multi-mode approach wave guide measurements have the potential to access these properties. The advantage of ITO layers is that they can be used as a wave guide as well as a substrate for electrochemical measurements. However, preparation conditions need to be optimized carefully. The thickness needs to be compromised vs. stability and surface roughness of the ITO. Surface roughness that was deteriorated by grain protrusions could successfully be overcome by coverage with the hydrogel. The polymer layer in turn had to be kept at a thickness of around 60 nm in order to ensure a smooth surface for the protein/lipid layer. About 60 nm layer thickness is sufficient to mimic the submembrane space. Small molecules such as cyt c penetrate easily.

The P(HEAAm-co-NTAAAm-co-MABP) proved to be a good approach towards gel-supported ptBLM with mesh sizes below the size of the protein. This ensures that the protein preferentially binds to the top layer so that a lipid layer exclusively forms at the interphase between polymer and water. The lipid bilayers seem to preserve a certain flexibility as shown by cyt c, which was able to penetrate the lipid layer, despite its high electrical sealing properties.

Ratiometric emisson spectroscopy was performed on hydrogel-supported ptBLMs. The fluorescent LHCIIb was used in a first place as a test protein to form the ptBLM. Hereby the effect of ITO on the emission properties of fluorescing species could be investigated. The LHCIIb complex is incorporated into the ptBLM, hence, the chromophores are located within the hydrophobic interior of the lipid bilayer and the emission property of LHCIIb becomes sensitive to the surrounding electric field. An attempt was made, to utilize LHCIIb as a probe for the membrane potential. However, strong bleaching effects and low sensitivity did not allow detection of changes in membrane potential differences.

The potential sensitive di-8-ANEPPS was used as an alternative probe. Prior to incorporation of di-8-ANEPPS into the ptBLM together with *cytochrome c oxidase*, the efficiency of the dye was tested in a tBLM system. Membrane potentials induced by defined square waveform voltage pulses were successfully measured. These data provided a conversion factor in terms of the ratiometric parameter $\mathrm{R_n}$ (0.05/100 mV) for the quantitative measurement of the membrane potential in tBLMs. Potential changes down to 30-50 mV were resolved in this system, which was also defined as the the limit of detection (LOD), i.e. the smallest resolvable potential change.

The most significant result of this work was the measurement of the membrane potential induced in a gel-supported ptBLM by an external voltage waveform. The primary aim of this work was accomplished with it. The data provide a basis for the measurement of the self-generated $\Delta\phi_m$ of CcO in a ptBLM. Though, the absolute voltage resolution was lower compared to the reference measurements in tBLM (50 mV). However, this can be explained by the smaller lipid amount in the ptBLM. The dye is incorporated only into the small bilayer patches between the proteins. The sensitivity can be further increased by future developments in the design of voltage sensitive dyes.

In conclusion, the membrane potential plays a crucial role in many cell membrane process. The catalytic activity of CcO is closely linked to $\Delta\phi_m$. On the other side, model membrane systems like the ptBLM offer a general approach for the investigation of membrane proteins. However, the parameter $\Delta\phi_m$ is hard to access in this configuration, where the BLM is in close proximity to the electrode surface. To the present, there have been no direct measurements of $\Delta\phi_m$ in planar, solid-supported BLMs like the one presented here. The gel-supported ptBLM system on transparent conducting substrates like ITO offers a great platform in order to measure membrane potentials such as the $\Delta\phi_m$ induced by applied electrical potentials. Furthermore, the ptBLM technology allows the incorporation of a large variety of His-tagged membrane proteins, thus making the techniques presented here an interesting tool for the investigation of the correlation between protein activity and membrane potential.

Appendix A

Materials and Methods

A.1 Chemicals

Chemicals used during this work and the companies they were purchased from:

- Ammonia (NH3): 32 % [WTL Laborbedarf GmbH]
- ANTA: Nα' ,Nα" -bis(carboxymethyl)-L-lysine ($C_{10}H_{18}N_2O_6$) [Fluka]
- DDM: n-Dodecyl-β-D-maltoside [Sigma]
- DiPhyPC: 1,2 Diphytanoyl-sn-Glycero-3-Phosphocholine [Avanti Polar Lipids, Inc]
- Acetic acid ($C_2H_4O_2$) [Fluka]
- Gold: 99,99 % [ESG Edelmetall Service GmbH& Co. K]
- Potassium chloride (KCl) [Sigma]
- Potassium carbonate (K_2CO_3) [Sigma]
- Potassium hydroxide (KOH) 85 % [WTL Laborbedarf]
- Potassium phosphate (K_2HPO_4)
- Nickel(II)-chloride Hexahydrate ($NiCl_2 \cdot 6\,H_2O$) [Fluka]
- Platin wire: diameter 0,1 mm, 99 % [Chempur]
- Hydrochloric acid (HCl) 37 % [WTL Laborbedarf]
- Sulfuric acid (H_2SO_4) [Acros Organics]

- Silver wire: diameter 1,0 mm, 99 % [Chempur]
- Nitrogen gas, purity 4 [Westfalen AG, Münster]
- Hydrogen peroxide (H_2O_2) 35 % [Sigma]
- Sodium dithionite [Fluka]
- Cyt c: *Cytochrome c*, bovine heart [Sigma]
- CcO: *Cytochrom c Oxidase* (*Paracoccus denitrificans*, histidine-anchor at subunit I) Prof. Bernd Ludwig, University of Frankfurt
- Biobeads SM-2 adsorbent 20-50 mesh [Bio-Rad Laboratories, Inc.]
- LHCIIb: light harvesting complex, LHCb1*2 (AB80) from pea (*Pisum sativum*) with Cys79 replaced by serine (His-tag at C-terminus), Prof. Paulsen, University of Mainz

PBS buffer was prepared on a routine basis using 0.1 M KCl, 0.05 M K_2HPO_4. The buffer solution was titrated to pH 8 using HCl.

A.2 Fluorescence Measurements

The FCS module Confocor 2 (Fig. A.1) in a confocal microscope (Carl Zeiss Jena, Germany) was employed for the ratiometric fluorescence measurements presented in chapter 4. During FCS recording a raw data file containing all photon counting events was produced. The file was processed offline for averaging and ratio formation using Matlab (Mathworks, Inc., MA, USA). For fluorescence imaging the laser scanning image module (LSM 510) of the same microscope was used (Fig. A.2).

A.3 Preparation of the ITO Layer

The ITO layer was deposited on float glass (Menzel, Braunschweig, Germany). Glass slides were cleaned in piranha solution (H2O:H2SO4:H2O2; 5:1:1 v/v) and rinsed using DI water. ITO was deposited by DC magnetron using the parameters described in chapter 3. Sputtering was performed using a Balzers sputtering system (Oerlikon Balzers Lichtenstein). The target used was a 3 inch In2O3:SnO2 (90:10) (MaTeck, Juelich, Germany). Series of slides were always prepared on the same day. After

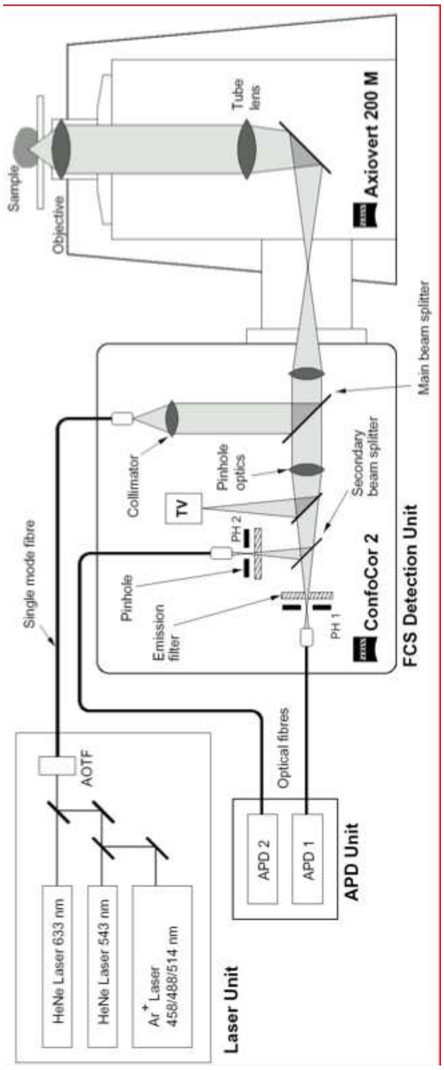

Figure A.1: FCS module of the Zeiss confocal microscope.

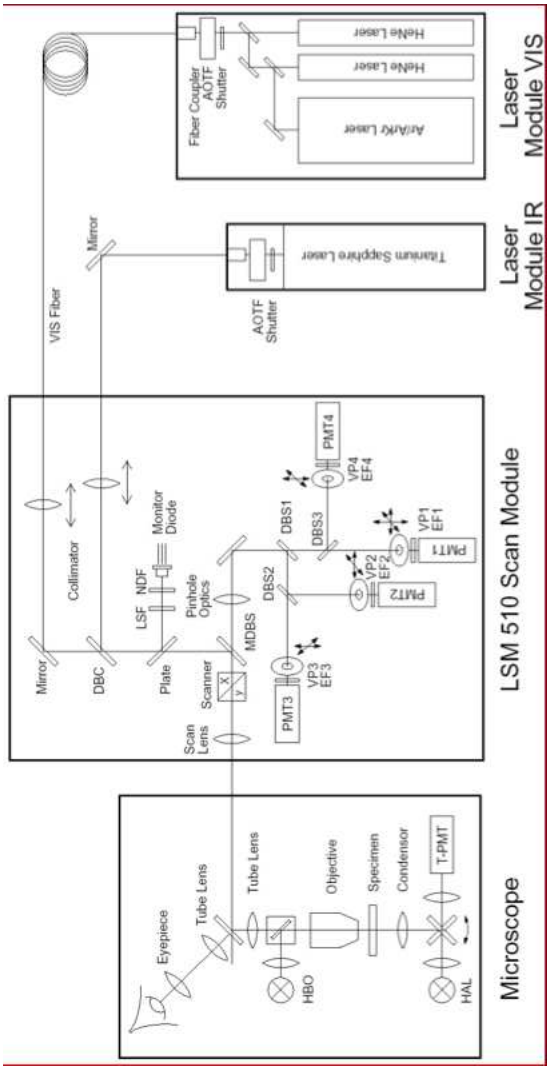

Figure A.2: LSM module of the Zeiss confocal microscope for fluorescence imaging.

deposition under each parameter set used the sheet resistance R_s was measured by a four-point probe method according to Van-der-Paw.

A.4 Preparation of P(PFPA-co-MAPB) Coated ITO

he ITO coated glass slides were functionalized with the BP-silane as described earlier[37]. On top of the silane layer the reactive copolymer P(PFPA-co-MAPB) was spin-coated from chloroform (1 % w), dried over night at 50° in a vacuum and cross linked by photopolymerization with a wavelength of 254 nm and a total energy of 60 J/ cm^2.

A.5 Functionalization with NTA

The polymer-coated ITO samples were incubated for 2 h in an aqueous 0.15 M (ANTA) solution (pH 9.8, 0.5 M K_2CO_3 buffer) and after 2 h ethanolamine (5 mM) was added to the same solution. The samples were left for a further 30 min in the solution and subsequently rinsed using MilliQ water.

A.6 Electrochemical Measurements

Electrochemical measurements were taken in a three-electrode configuration where the ITO slide was used as the working, a home-made Ag/AgCl (sat. KCL) as the reference, and a platinum wire as the counter electrode. Electrochemical impedance spectra and cyclovoltammetry measurements were performed using Autolab instrument PGSTAT302 (Eco Chemie, Utrecht, Netherlands) equipped with a FRA2 module for frequency response analysis, an ECD-module amplifier for low currents and a SCAN-GEN module for analog potential scanning. Spectra were recorded in the frequency range from 100 kHz to 0.003 Hz using an amplitude of 10 mV. Resulting spectra were analyzed by Zview (Version 2.6, Scribner Associates, Southern Pines, NC) by complex nonlinear fitting of the data to a model circuit

A.7 Surface Plasmon Resonance Optical Waveguide spectroscopy (SPR/OWS)

SPR/OWS was performed in a custom made setup described previously using the Kretschmann-configuration. The glass slide (LaSFN9 glass from Hellma Optik, Jena, refractive index n=1.8385 at 632.8 nm) was optically matched to the base of a 45° glass prism (LaSFN9). Monochromatic light from a He/NeLaser, (Uniphase, San Jose, CA) was directed through the prism and collected by a custom made photodiode detector. The glass slide was provided with a multilayer system starting with a 41 nm thick gold layer electrothermally evaporated on top of 2 nm thick Cr adhesion layer. A 680 nm thick ITO layer was then sputtered onto the gold layer under the conditions described above and the surface was spin-coated with P(HEAAm-co-NTAAAm-co-MABP). ITO served as the guiding media as well as the working electrode. Change of N_{eff} (dN_{eff}) for varying ITO thickness was simulated using n=1.9065 for ITO taken from ellipsometry measurements. The simulation software package used was CAMFR (CAvity Modelling Framework, INTEC, Universiteit Gent).

A.8 Atomic Force Microscopy (AFM)

Atomic force microscopy was performed using the AFM Dimension 3100CL Olympus (Veeco Instruments Inc, NY) in tapping mode with a silicon cantilever. The height profile images were analyzed in terms of root mean square (RMS) and peak-valley height also denoted as Z-range (Nanscope software v2.5r, Veeco).

A.9 Preparation of Reduced Cyt c

The stock solution of reduced bovine heart cyt c (Sigma Aldrich, St. Louis, MO) was prepared by adding 5 mg of sodium dithionite to an aqueous solution of 40 mg cyt c in 1 mL PBS. The reducing agent was removed subsequently by gel filtration utilizing a Sephadex column (G-25 M, GE Healthcare Bio-Science AB, Uppsala, Sweden).

Appendix B

Design of Measurement Cell

A flow cell for fluorescence spectroscopy and electrochemical measurements was developed. The flow cell consists of a 1.6 mL compartment for the buffer solution. Ag/AgCl reference and a silver wire counter electrode are connected to the cell. The ITO coated coverslip is the working electrode. A gold plate is pressed against the ITO surface outside the cell compartment during cell assembling. The gold plate is than connected to the potentiostat using a clamp.

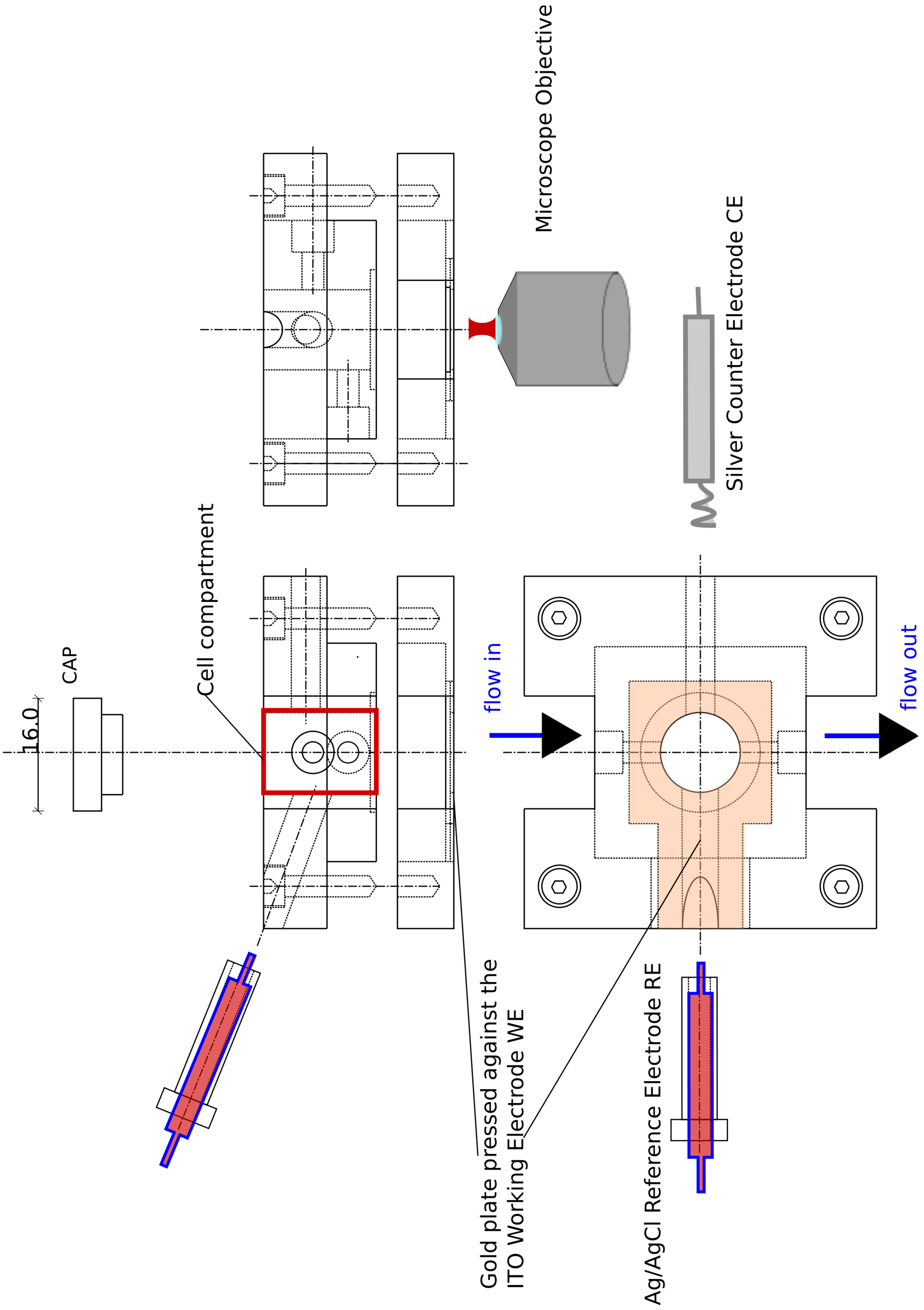

Figure B.1: Blueprint of the flow cell employed for fluorescence spectroscopy measurements. The cell is designed for simultaneous application of electrochemical methods and fluorescence spectroscopy. The body of the cell is made of polyether ether ketone (PEEK). The location of the electrodes and the objective of the inverse confocal microscope are also shown.

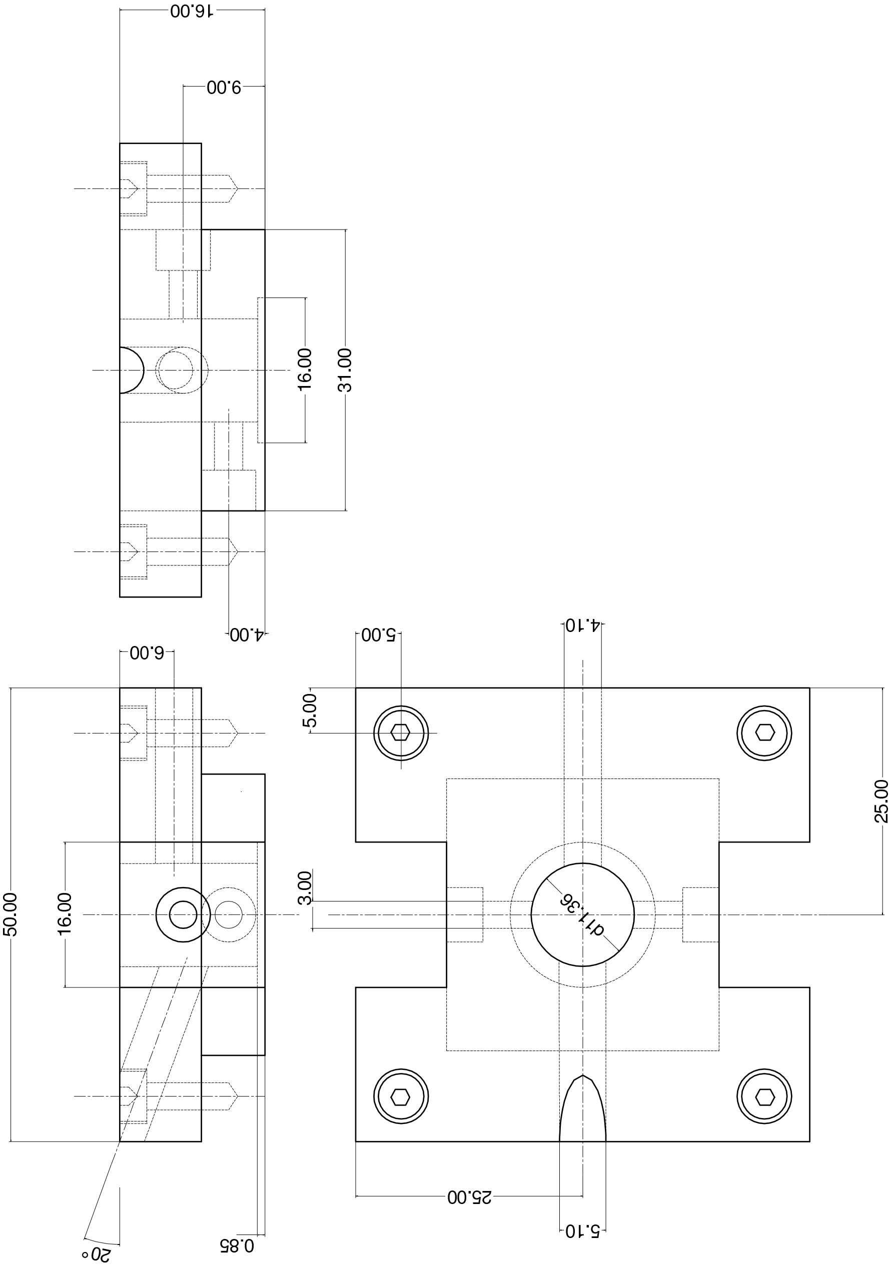

Figure B.2: Blueprint of the main part of Fig. B.1.

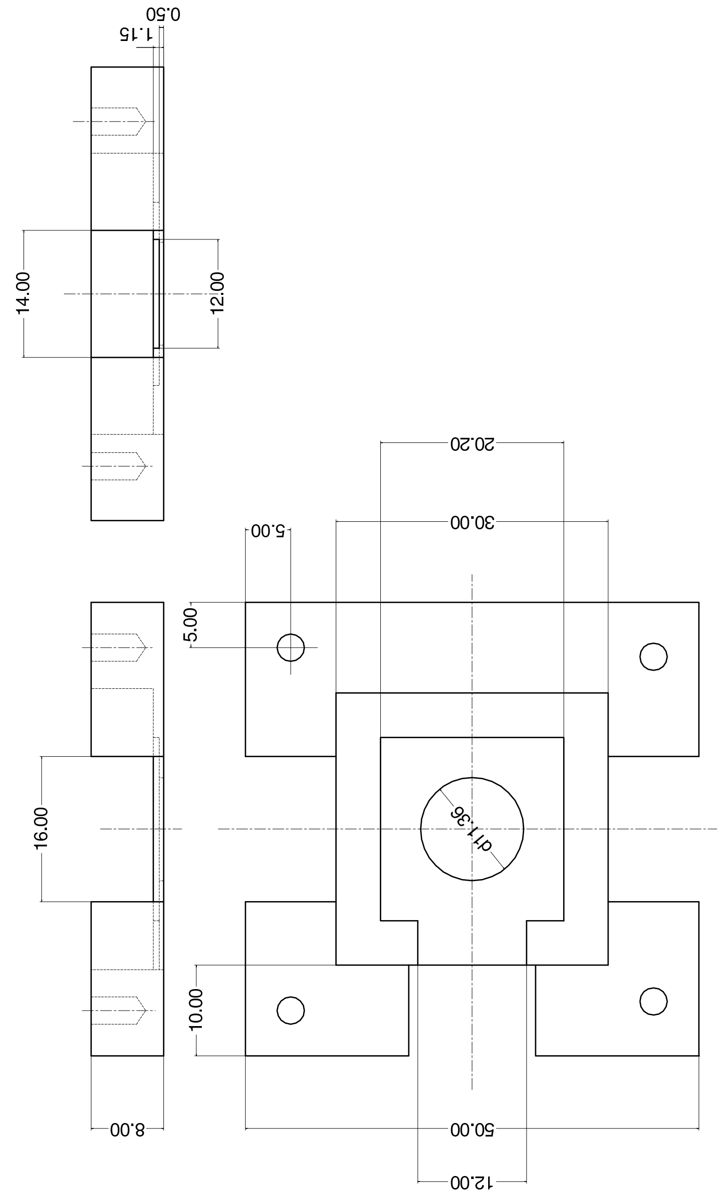

Figure B.3: Blueprint of the bottom part of Fig. B.1.

List of Figures

List of Tables

Bibliography

[1] A. An, H. Arwin, C. Chen, R. W. Collins, A. S. Ferlauto, J. N. Hilfiker, J. Humlicek, E. A. Irene, G. E. J. Jellison, J. Lee, F. A. Modine, A. RÃűseler, M. Schubert, H. G. Tompkins, and J. A. Zapien. *Handbook of Ellispometry.* William Andrew Publishing, 2005.

[2] K. Ataka, F. Giess, W. Knoll, R. Naumann, S. Haber-Pohlmeier, B. Richter, and J. Heberle. Oriented attachment and membrane reconstitution of his-tagged cytochrome c oxidase to a gold electrode: In situ monitoring by surface-enhanced infrared absorption spectroscopy. *J. Am. Chem. Soc.*, 126(49):16199–16206, 2004.

[3] V. Atanasov, N. Knorr, R. S. Duran, S. Ingebrandt, A. Offenhausser, W. Knoll, and I. Koper. Membrane on a chip: A functional tethered lipid bilayer membrane on silicon oxide surfaces. *Biophys. J.*, 89(3):1780–1788, Sept. 2005.

[4] V. Atanasov, P. P. Atanasova, I. K. Vockenroth, N. Knorr, and I. Koper. A molecular toolkit for highly insulating tethered bilayer lipid membranes on various substrates. *Bioconjugate Chem.*, 17(3):631–637, May 2006.

[5] T. Balgar, R. Bautista, N. Hartmann, and E. Hasselbrink. An afm study of the growth kinetics of the self-assembled octadecylsiloxane monolayer on oxidized silicon. *Surface Science*, 532:963–969, 2003.

[6] J. M. Beach, E. D. McGahren, J. Xia, and B. R. Duling. Ratiometric measurement of endothelial depolarization in arterioles with a potential-sensitive dye. *Am J Physiol Heart Circ Physiol*, 270(6):H2216–2227, 1996. URL `http://ajpheart.physiology.org/cgi/content/abstract/270/6/H2216`.

[7] L. Becucci, M. R. Moncelli, and R. Guidelli. Ion carriers and channels in metal-supported lipid bilayers as probes of transmembrane and dipole potentials. *Langmuir*, 19(8):3386–3392, Apr. 2003.

[8] I. Belevich, D. A. Bloch, N. Belevich, M. WikstrâĹŽâĹĆm, and M. I. Verkhovsky. Exploring the proton pump mechanism of cytochrome c oxidase in real time. *Proceedings of the National Academy of Sciences*, 104(8):2685–2690, 2007. doi: 10.1073/pnas.0608794104. URL `http://www.pnas.org/content/104/8/2685.abstract`.

[9] G. Belmonte, L. Cescatti, B. Ferrari, T. Nicolussi, M. Ropele, and G. Menestrina. Pore formation by staphylococcus aureus alpha-toxin in lipid bilayers. *European Biophysics Journal*, 14(6):349–358, May 1987. URL `http://dx.doi.org/10.1007/BF00262320`.

[10] D. A. Bloch, A. Jasaitis, and M. I. Verkhovsky. Elevated proton leak of the intermediate o-h in cytochrome c oxidase. *Biophysical Journal*, 96(11):4733–4742, 2009.

[11] K. B. Blodgett. Films built by depositing successive monomolecular layers on a solid surface. *Journal of the American Chemical Society*, 57(6):1007–1022, June 1935. ISSN 0002-7863. URL `http://dx.doi.org/10.1021/ja01309a011`.

[12] R. A. Bockmann, B. L. de Groot, S. Kakorin, E. Neumann, and H. Grubmuller. Kinetics, statistics, and energetics of lipid membrane electroporation studied by molecular dynamics simulations. *Biophysical Journal*, 95(4):1837–1850, 2008.

[13] P. A. Boucher, B. Joos, M. J. Zuckermann, and L. Fournier. Pore formation in a lipid bilayer under a tension ramp: Modeling the distribution of rupture tensions. *Biophysical Journal*, 92(12):4344–4355, 2007.

[14] G. Branden, R. B. Gennis, and P. Brzezinski. Transmembrane proton translocation by cytochrome c oxidase. *Biochimica et Biophysica Acta*, 1757(8):1052–1063, 2006.

[15] D. W. Britt and V. Hlady. An afm study of the effects of silanization temperature, hydration, and annealing on the nucleation and aggregation of condensed

ots domains on mica. *Journal of Colloid and Interface Science*, 178(2):775–784, 1996.

[16] K. A. Brogden. Antimicrobial peptides: Pore formers or metabolic inhibitors in bacteria? *Nature Reviews Microbiology*, 3:238–250, 2005.

[17] J. B. BRZOSKA, I. BENAZOUZ, and F. RONDELEZ. Silanization of solid substrates - a step toward reproducibility. *Langmuir*, 10(11):4367–4373, Nov. 1994.

[18] A. Bullen and P. Saggau. High-speed, random-access fluorescence microscopy: Ii. fast quantitative measurements with voltage-sensitive dyes, Apr. 1999. ISSN 0006-3495. URL `http://linkinghub.elsevier.com/retrieve/pii/S0006349599773832`.

[19] A. Bullen, S. S. Patel, and P. Saggau. High-speed, random-access fluorescence microscopy .1. high-resolution optical recording with voltage-sensitive dyes and ion indicators. *Biophysical Journal*, 73(1):477–491, July 1997.

[20] R. C. Carroll and E. Racker. Preparation and characterization of cytochrome c oxidase vesicles with high respiratory control. *Journal of Biological Chemistry*, 252(20):6981–6990, 1977. URL `http://www.jbc.org/content/252/20/6981.short`.

[21] W. Chen and R. Dando. Electrical activation of na/k pumps can increase ionic concentration gradient and membrane resting potential. *Journal of Membrane Biology*, 214(3):147–155, 2006.

[22] W. Chen and R. Dando. Membrane potential hyperpolarization in mammalian cardiac cells by synchronization modulation of na/k pumps. *Journal of Membrane Biology*, 221(3):165–173, 2008.

[23] B. A. Cornell, G. Krishna, P. D. Osman, R. D. Pace, and L. Wieczorek. Tethered-bilayer lipid membranes as a support for membrane-active peptides. *Biochemical Society Transactions*, 29:613–617, 2001.

[24] J. K. Cullison, F. M. Hawkridge, N. Nakashima, and S. Yoshikawa. A study of cytochrome c oxidase in lipid bilayer membranes on electrode

surfaces. *Langmuir*, 10(3):877–882, Mar. 1994. ISSN 0743-7463. URL `http://dx.doi.org/10.1021/la00015a044`.

[25] W. K. den Otter. Free energies of stable and metastable pores in lipid membranes under tension. *J Chem Phys*, 131(20):205101, 2009.

[26] M. Eberhardt, R. Mruk, R. Zentel, and P. Theato. Synthesis of pentafluorophenyl(meth)acrylate polymers: New precursor polymers for the synthesis of multifunctional materials. *European Polymer Journal*, 41(7):1569–1575, 2005.

[27] J. S. Erlichman, A. C. Boyer, P. Reagan, R. W. Putnam, N. A. Ritucci, and J. C. Leiter. Chemosensory responses to co2 in multiple brain stem nuclei determined using a voltage-sensitive dye in brain slices from rats. *Journal of Neurophysiology*, 102(3):1577–1590, Sept. 2009.

[28] A. Y. Fadeev and T. J. McCarthy. Trialkylsilane monolayers covalently attached to silicon surfaces: Wettability studies indicating that molecular topography contributes to contact angle hysteresis. *Langmuir*, 15(11):3759–3766, 1999.

[29] A. FINKELSTEIN. Water and nonelectrolyte permeability of lipid bilayer membranes. *Journal of General Physiology*, 68(2):127–135, 1976.

[30] J. A. N. Fisher, B. M. Salzberg, and A. G. Yodh. Near infrared two-photon excitation cross-sections of voltage-sensitive dyes. *Journal of Neuroscience Methods*, 148(1):94–102, Oct. 2005.

[31] R. Flewelling and W. Hubbell. The membrane dipole potential in a total membrane potential model. applications to hydrophobic ion interactions with membranes, Feb. 1986. ISSN 0006-3495. URL `http://linkinghub.elsevier.com/retrieve/pii/S0006349586836645`.

[32] J. Franklin and D. Cafiso. Internal electrostatic potentials in bilayers: measuring and controlling dipole potentials in lipid vesicles, July 1993. ISSN 0006-3495. URL `http://linkinghub.elsevier.com/retrieve/pii/S0006349593810518`.

[33] M. G. Friedrich, F. Giess, R. Naumann, W. Knoll, K. Ataka, J. Heberle, J. Hrabakova, D. H. Murgida, and P. Hildebrandt. Active site structure and

redox processes of cytochrome c oxidase immobilised in a novel biomimetic lipid membrane on an electrode. *Chemical Communications*, (21):2376–2377, 2004.

[34] M. G. Friedrich, V. U. Kirste, J. P. Zhu, R. B. Gennis, W. Knoll, and R. L. C. Naumann. Activity of membrane proteins immobilized on surfaces as a function of packing density. *J. Phys. Chem. B*, 112(10):3193–3201, Mar. 2008.

[35] M. G. Friedrich, M. A. Plum, M. G. Santonicola, V. U. Kirste, W. Knoll, B. Ludwig, and R. L. C. Naumann. In situ monitoring of the catalytic activity of cytochrome c oxidase in a biomimetic architecture. *Biophys. J.*, 95(3):1500–1510, Aug. 2008.

[36] F. Gambinossi, M. Mannini, P. Baglioni, and G. Caminati. Spectroscopic properties of langmuir-blodgett films containing a potential-sensitive dye. *Materials Science & Engineering C-biomimetic and Supramolecular Systems*, 23(6-8):897–902, Dec. 2003.

[37] M. Gianneli, R. F. Roskamp, U. Jonas, B. Loppinet, G. Fytas, and W. Knoll. Dynamics of swollen gel layers anchored to solid surfaces. *Soft Matter*, 4(7): 1443–1447, 2008.

[38] F. Giess, M. G. Friedrich, J. Heberle, R. L. Naumann, and W. Knoll. The protein-tethered lipid bilayer: A novel mimic of the biological membrane. *Biophys. J.*, 87(5):3213–3220, 2004.

[39] S. A. Glazier, D. J. Vanderah, A. L. Plant, H. Bayley, G. Valincius, and J. J. Kasianowicz. Reconstitution of the pore-forming toxin alpha-hemolysin in phospholipid/18-octadecyl-1-thiahexa(ethylene oxide) and phospholipid/n-octadecanethiol supported bilayer membranes. *Langmuir*, 16(26):10428–10435, 2000.

[40] G. L. Goff, M. F. Vitha, and R. J. Clarke. Orientational polarisability of lipid membrane surfaces. *Biochimica et Biophysica Acta (BBA) - Biomembranes*, 1768(3):562 – 570, 2007. ISSN 0005-2736. doi: DOI: 10.1016/j.bbamem.2006.10.019. URL `http://www.sciencedirect.com/science/article/B6T1T-4M93KRB-1/2/a98434dac106d1b`

[41] J. E. Gonzalez and R. Y. Tsien. Improved indicators of cell membrane potential that use fluorescence resonance energy transfer. *Chemistry & Biology*, 4(4): 269–277, 1997. ISI:A1997XB73200004.

[42] J. GonzÂůlez and R. Tsien. Voltage sensing by fluorescence resonance energy transfer in single cells, Oct. 1995. ISSN 0006-3495. URL `http://linkinghub.elsevier.com/retrieve/pii/S0006349595800299`.

[43] E. GROSS, R. S. BEDLACK, and L. M. LOEW. Dual-wavelength ratiometric fluorescence measurement of the membrane dipole potential. *Biophysical Journal*, 67(1):208–216, July 1994.

[44] W. I. Gruszecki, A. Wardak, and W. Maksymiec. The effect of blue light o electron transport in photosystem ii reconstituted in planar bilayer lipid membrane. *Journal of Photochemistry and Photobiology B: Biology*, 39(3):265–268, July 1997. ISSN 1011-1344. URL `http://www.sciencedirect.com/science/article/B6TH0-3SHJ51Y-V/2/4b7b90ad52b0a32`

[45] A. Haas, D. Pilloud, K. Reddy, G. Babcock, C. Moser, J. Blasie, and P. Dutton. Cytochrome c and cytochrome c oxidase: monolayer assemblies and catalysis. *Journal of Physical Chemistry B*, 105:11351âĂŞ11362, 2001.

[46] L. H. He, J. W. F. Robertson, J. Li, I. Karcher, S. M. Schiller, W. Knoll, and R. Naumann. Tethered bilayer lipid membranes based on monolayers of thiolipids mixed with a complementary dilution molecule. 1. incorporation of channel peptides. *Langmuir*, 21(25):11666–11672, Dec. 2005.

[47] H. Hillebrandt, G. Wiegand, M. Tanaka, and E. Sackmann. High electric resistance polymer/lipid composite films on indium-tin-oxide electrodes. *Langmuir*, 15(24):8451–8459, Nov. 1999.

[48] S. Hobe, I. Trostmann, S. Raunser, and H. Paulsen. Assembly of the major light-harvesting chlorophyll-a/b complex - thermodynamics and kinetics of neoxanthin binding. *Journal of Biological Chemistry*, 281(35):25156–25166, Sept. 2006.

[49] A. Holoubek, J. Vecer, and K. Sigler. Monitoring of the proton electrochemical gradient in reconstituted vesicles: Quantitative measurements of both trans-

membrane potential and intravesicular ph by ratiometric fluorescent probes. *Journal of Fluorescence*, 17(2):201–213, Mar. 2007.

[50] A. T. A. Jenkins, R. J. Bushby, N. Boden, S. D. Evans, P. F. Knowles, Q. Y. Liu, R. E. Miles, and S. D. Ogier. Ion-selective lipid bilayers tethered to microcontact printed self-assembled monolayers containing cholesterol derivatives. *Langmuir*, 14(17):4675–4678, 1998.

[51] G. Jeschke, A. Bender, T. Schweikardt, G. Panek, H. Decker, and H. Paulsen. Localization of the n-terminal domain in light-harvesting chlorophyll a/b protein by epr measurements. *Journal of Biological Chemistry*, 280(19):18623–18630, May 2005.

[52] L. J. C. Jeuken, S. D. Connell, M. Nurnabi, J. O'Reilly, P. J. F. Henderson, S. D. Evans, and R. J. Bushby. Direct electrochemical interaction between a modified gold electrode and a bacterial membrane extract. *Langmuir*, 21(4):1481–1488, Feb. 2005. ISSN 0743-7463. URL `http://dx.doi.org/10.1021/la047732f`.

[53] M. Jung. *Patterning of Tethered Bilayer Lipid Membranes*. PhD thesis, Johannes Gutenberg âĂŞ UniversitÃďt Mainz, 2008.

[54] Y. S. Jung, D. W. Lee, and D. Y. Jeon. Influence of dc magnetron sputtering parameters on surface morphology of indium tin oxide thin films. *Appl. Surf. Sci.*, 221(1-4):136–142, 2004.

[55] S. Kakorin and E. Neumann. Ionic conductivity of electroporated lipid bilayer membranes. *Bioelectrochemistry*, 56(1-2):163–166, 2002.

[56] W. Y. Kao, C. E. Davis, Y. I. Kim, and J. M. Beach. Fluorescence emission spectral shift measurements of membrane potential in single cells. *Biophysical Journal*, 81(2):1163–1170, Aug. 2001.

[57] V. Kirste. *Elektrochemisch gesteuerte zeitaufgelÃűste Infrarotspektroskopie an Redox-Membranproteinen in einer biomimetischen Membran-Architektur*. PhD thesis, Johannes-Gutenberg-UniversitÃďt Mainz, 2007.

[58] V. U. Kirste, F. Giess, R. Naumann, and W. Knoll. Seiras as a method for the analysis of transport-mechanisms through membrane-proteins. *European Biophysics Journal*, 34(6):802, 2005.

[59] A. S. Klymchenko, H. Stoeckel, K. Takeda, and Y. Mely. Fluorescent probe based on intramolecular proton transfer for fast ratiometric measurement of cellular transmembrane potential. *J. Phys. Chem. B*, 110(27):13624–13632, 2006. Klymchenko, Andrey S. Stoeckel, Herrade Takeda, Kenneth Mely, Yves.

[60] W. Knoll, C. W. Frank, C. Heibel, R. Naumann, A. Offenhausser, J. Ruhe, E. K. Schmidt, W. W. Shen, and A. Sinner. Functional tethered lipid bilayers. *J Biotechnol*, 74(3):137–58, 2000.

[61] J. Koepke, E. Olkhova, H. Angerer, H. Muller, G. Peng, and H. Michel. High resolution crystal structure of paracoccus denitrificans cytochrome c oxidase: New insights into the active site and the proton transfer pathways. *Biochim. Biophys. Acta*, 1787:635–645, 2009.

[62] A. A. Konstantinov, S. Siletsky, D. Mitchell, A. Kaulen, and R. B. Gennis. The roles of the two proton input channels in cytochrome c oxidase from rhodobacter sphaeroides probed by the effects of site-directed mutations on time-resolved electrogenic intraprotein protonâĂŽÃĎÃćtransfer. *Proceedings of the National Academy of Sciences of the United States of America*, 94(17):9085–9090, 1997. URL `http://www.pnas.org/content/94/17/9085.abstract`.

[63] G. Krishna, J. Schulte, B. A. Cornell, R. Pace, L. Wieczorek, and P. D. Osman. Tethered bilayer membranes containing ionic reservoirs: The interfacial capacitance. *Langmuir*, 17(16):4858–4866, 2001.

[64] G. Krishna, J. Schulte, B. A. Cornell, R. J. Pace, and P. D. Osman. Tethered bilayer membranes containing ionic reservoirs: Selectivity and conductance. *Langmuir*, 19(6):2294–2305, 2003.

[65] P. Krysinski, A. Zebrowska, A. Michota, J. Bukowska, L. Becucci, and M. R. Moncelli. Tethered mono- and bilayer lipid membranes on au and hg. *Langmuir*, 17(13):3852–3857, 2001.

[66] M. KUHNER, R. TAMPE, and E. SACKMANN. Lipid monolayer and bilayer supported on polymer-films - composite polymer-lipid films on solid substrates. *Biophys. J.*, 67(1):217–226, July 1994.

[67] F. Kurdesau, G. Khripunov, A. F. da Cunha, M. Kaelin, and A. N. Tiwari. Comparative study of ito layers deposited by dc and rf magnetron sputtering at room temperature. *J. Non-Cryst. Solids*, 352(9-20):1466–1470, 2006.

[68] H. LANG, C. DUSCHL, and H. VOGEL. A new class of thiolipids for the attachment of lipid bilayers on gold surfaces. *Langmuir*, 10(1):197–210, Jan. 1994.

[69] I. Langmuir and V. J. Schaefer. Activities of urease and pepsin monolayers. *Journal of the American Chemical Society*, 60(6):1351–1360, June 1938. ISSN 0002-7863. URL `http://dx.doi.org/10.1021/ja01273a023`.

[70] H.-m. Lee, T. K. Das, D. L. Rousseau, D. Mills, S. Ferguson-Miller, and R. B. Gennis. Mutations in the putative h-channel in the cytochrome c oxidase from rhodobacter sphaeroides show that this channel is not important for proton conduction but reveal modulation of the properties of heme aâĂŽÃĎâĂă. *Biochemistry*, 39(11):2989–2996, Mar. 2000. ISSN 0006-2960. URL `http://dx.doi.org/10.1021/bi9924821`.

[71] K. H. Leung and P. C. Hinkle. Reconstitution of ion transport and respiratory control in vesicles formed from reduced coenzyme q-cytochrome c reductase and phospholipids. *Journal of Biological Chemistry*, 250(21):8467–8471, 1975. URL `http://www.jbc.org/content/250/21/8467.abstract`.

[72] H. Lin, J. Yu, S. Lou, J. Wang, and Y. Jiang. Properties of dc magnetron sputtered indium-tin oxide films with the assistance of tiny h_2o vapor at low temperature. *Proceedings of the SPIE - The International Society for Optical Engineering*, pages 672243–1–5, 2007.

[73] J. Liu. *Systematic Studies of Protein Immobilization by Surface Plasmon Field-Enhanced Fluorescence Spectroscopy.* PhD thesis, Johannes Gutenberg-UniversitÃďt in Mainz, 2005.

[74] L. Loew and L. Simpson. Charge-shift probes of membrane potential: a probable electrochromic mechanism for p-aminostyrylpyridinium probes on a hemispherical lipid bilayer. *Biophys. J.*, 34(3):353–365, June 1981. ISSN 0006-3495. URL `http://linkinghub.elsevier.com/retrieve/pii/S0006349581848540`.

[75] L. M. Loew. Characterization of potentiometric membrane dyes. In *Biomembrane Electrochemistry*, volume 235, pages 151–173. An American Chemical Society Publication, 1994. ISI:A1994BA42T00009.

[76] L. M. Loew, G. W. Bonneville, and J. Surow. Charge shift optical probes of membrane potential. theory. *Biochemistry*, 17(19):4065–4071, Sept. 1978. ISSN 0006-2960. URL `http://dx.doi.org/10.1021/bi00612a030`.

[77] L. M. Loew, L. Simpson, A. Hassner, and V. Alexanian. An unexpected blue shift caused by differential solvation of a chromophore oriented in a lipid bilayer. *Journal of the American Chemical Society*, 101(18):5439–5440, Aug. 1979. ISSN 0002-7863. URL `http://dx.doi.org/10.1021/ja00512a068`.

[78] S. Lucioli, K. Hoffmeier, R. Carrozzo, A. Tessa, B. Ludwig, and F. M. Santorelli. Introducing a novel human mtdna mutation into the paracoccus denitrificans cox i gene explains functional deficits in a patient. *Neurogenetics*, 7(1):51–57, Mar. 2006.

[79] B. LUDWIG and G. SCHATZ. A 2-subunit cytochrome-c oxidase (cytochrome-aa3) from paracoccus-dentrificans. *Proceedings of the National Academy of Sciences of the United States of America-biological Sciences*, 77(1):196–200, 1980.

[80] I. Markovich and D. Mandler. The effect of an alkylsilane monolayer on an indium-tin-oxide on the electrochemistry of hexacyanoferrat. *Journal of Electroanalytical Chemistry*, 484:194–202, 2000.

[81] S. J. MARRINK and H. J. C. BERENDSEN. Simulation of water transport through a lipid-membrane. *Journal of Physical Chemistry*, 98(15):4155–4168, 1994.

[82] D. J. McGillivray, G. Valincius, D. J. Vanderah, W. Febo-Ayala, J. T. Woodward, F. Heinrich, J. J. Kasianowicz, and M. Losche. Molecular-scale structural and functional characterization of sparsely tethered bilayer lipid membranes. *Biointerphases*, 2(1):21–33, Mar. 2007.

[83] H. Michel. The mechanism of proton pumping by cytochrome c oxidase. *Proc. Natl. Acad. Sci. U. S. A.*, 95(22):12819–12824, Oct. 1998.

[84] P. Mitchell. Chemiosmotic coupling in oxidative and photosynthetic phosphorylation. *Biol. Rev. Cambridge Phil Soc.*, 41:445–502, 1966.

[85] L. Movileanu, D. Popescu, S. Ion, and A. I. Popescu. Transbilayer pores induced by thickness fluctuations. *Bulletin of Mathematical Biology*, 68(6):1231–1255, Aug. 2006.

[86] P. MUELLER and D. O. RUDIN. Action potentials induced in biomolecular lipid membranes. *Nature*, 217(5130):713–719, Feb. 1968. URL `http://dx.doi.org/10.1038/217713a0`.

[87] K. Muramoto, K. Hirata, K. Shinzawa-Itoh, S. Yoko-o, E. Yamashita, H. Aoyama, T. Tsukihara, and S. Yoshikawa. A histidine residue acting as a controlling site for dioxygen reduction and proton pumping by cytochrome c oxidase. *Proceedings of the National Academy of Sciences*, 104(19):7881–7886, 2007. doi: 10.1073/pnas.0610031104. URL `http://www.pnas.org/content/104/19/7881.abstract`.

[88] J. F. Nagle and S. Tristram-Nagle. Hydrogen bonded chain mechanisms for proton conduction and proton pumping. *Journal of Membrane Biology*, 74(1): 1–14, Feb. 1983. URL `http://dx.doi.org/10.1007/BF01870590`.

[89] C. A. Naumann, O. Prucker, T. Lehmann, J. Ruhe, W. Knoll, and C. W. Frank. The polymer-supported phospholipid bilayer: Tethering as a new approach to substrate-membrane stabilization. *Biomacromolecules*, 3(1):27–35, Jan. 2002.

[90] R. Naumann, A. Jonczyk, C. Hampel, H. Ringsdorf, W. Knoll, N. Bunjes, and P. Graber. Coupling of proton translocation through atpase incorporated into supported lipid bilayers to an electrochemical process. *Bioelectrochemistry and Bioenergetics*, 42(2):241–247, 1997.

[91] R. Naumann, E. K. Schmidt, A. Jonczyk, K. Fendler, B. Kadenbach, T. Liebermann, A. Offenhausser, and W. Knoll. The peptide-tethered lipid membrane as a biomimetic system to incorporate cytochrome c oxidase in a functionally active form. *Biosensors & Bioelectronics*, 14(7):651–662, Oct. 1999.

[92] R. Naumann, D. Walz, S. M. Schiller, and W. Knoll. Kinetics of valinomycin-mediated k1 ion transport through tethered bilayer lipid membranes. *Journal of Electroanalytical Chemistry*, 550:241–252, 2003.

[93] B. Neumcke, D. Walz, and P. LâĂřuger. Nonlinear electrical effects in lipid bilayer membranes: Iii. the dissociation field effect. *Biophysical Journal*, 10(2):172–182, Feb. 1970. ISSN 0006-3495. URL `http://www.sciencedirect.com/science/article/B94RW-4V8RX4P-5/2/4e7a2ac2c93b01e`

[94] M. Neunlist, S. Peters, and M. Schemann. Multisite optical recording of excitability in the enteric nervous system. *Neurogastroenterology and Motility*, 11 (5):393–402, Oct. 1999.

[95] V. Nikolov, J. Lin, M. Merzlyakov, K. Hristova, and P. C. Searson. Electrical measurements of bilayer membranes formed by langmuir-blodgett deposition on single-crystal silicon. *Langmuir*, 23(26):13040–13045, Dec. 2007.

[96] C. Nowak, C. Luening, D. Schach, D. Baurecht, W. Knoll, and R. L. C. Naumann. Electron transfer kinetics of cytochrome c in the submillisecond time regime using time-resolved surface-enhanced infrared absorption spectroscopy. *Journal of Physical Chemistry C*, 113(6):2256–2262, 2009.

[97] A. L. Obaid, T. Koyano, J. Lindstrom, T. Sakai, and B. M. Salzberg. Spatiotemporal patterns of activity in an intact mammalian network with single-cell resolution: Optical studies of nicotinic activity in an enteric plexus. *Journal of Neuroscience*, 19(8):3073–3093, Apr. 1999.

[98] A. L. Obaid, L. M. Loew, J. P. Wuskell, and B. M. Salzberg. Novel naphthylstyryl-pyridinium potentiometric dyes offer advantages for neural network analysis. *Journal of Neuroscience Methods*, 134(2):179–190, Apr. 2004.

[99] H. Okamoto, N. Sone, H. Hirata, M. Yoshida, and Y. Kagawa. Purified proton conductor in proton translocating adenosine triphosphatase of a thermophilic bacterium. *Journal of Biological Chemistry*, 252(17):6125–6131, 1977. URL `http://www.jbc.org/content/252/17/6125.abstract`.

[100] A. PARSEGIAN. Energy of an ion crossing a low dielectric membrane: Solutions to four relevant electrostatic problems. *Nature*, 221(5183):844–846, Mar. 1969. URL `http://dx.doi.org/10.1038/221844a0`.

[101] S. Paula, A. G. Volkov, and D. W. Deamer. Permeation of halide anions through phospholipid bilayers occurs by the solubility-diffusion mechanism. *Biophysical Journal*, 74(1):319–327, 1998.

[102] H. PAULSEN, U. RUMLER, and W. RUDIGER. Reconstitution of pigment-containing complexes from light-harvesting chlorophyll-a/b-binding protein over-expressed in escherichia-coli. *Planta*, 181(2):204–211, May 1990.

[103] C. Peggion, F. Formaggio, C. Toniolo, L. Becucci, M. R. Moncelli, and R. Guidelli. A peptide-tethered lipid bilayer on mercury as a biomimetic system. *Langmuir*, 17(21):6585–6592, 2001.

[104] P. Piguet and R. A. North. The inward rectifier potassium conductance in rat basophilic leukemia cells. *J. Cell Phys.*, 151:269âĂŞ275, 1992.

[105] B. K. Pillai, R. Jasuja, J. R. Simard, and J. A. Hamilton. Fast diffusion of very long chain saturated fatty acids across a bilayer membrane and their rapid extraction by cyclodextrins implications for adrenoleukodystrophy. *Journal of Biological Chemistry*, 284(48):33296–33304, 2009.

[106] O. Purrucker, A. Fortig, R. Jordan, and M. Tanaka. Supported membranes with well-defined polymer tethers-incorporation of cell receptors. *ChemPhysChem*, 5 (3):327–335, Mar. 2004.

[107] S. Qian, W. C. Wang, L. Yang, and H. W. Huang. Structure of transmembrane pore induced by bax-derived peptide: Evidence for lipidic pores. *Proceedings of the National Academy of Sciences of the United States of America*, 105(45): 17379–17383, 2008.

[108] C. I. Ragan and E. Racker. Partial resolution of the enzymes catalyzing oxidative phosphorylation. *Journal of Biological Chemistry*, 248(7):2563–2569, 1973. URL `http://www.jbc.org/content/248/7/2563.abstract`.

[109] B. Raguse, V. Braach-Maksvytis, B. A. Cornell, L. G. King, P. D. J. Osman, R. J. Pace, and L. Wieczorek. Tethered lipid bilayer membranes: Formation and ionic reservoir characterization. *Langmuir*, 14(3):648–659, Feb. 1998.

[110] E. Reimhult, F. HâĹŽâĹĆâĹŽâĹĆk, and B. Kasemo. Intact vesicle adsorption and supported biomembrane formation from vesicles in solution:âĂŽÃĎÃć influence of surface chemistry, vesicle size, temperature, and osmotic pressureâĂŽÃĎâĂă. *Langmuir*, 19(5):1681–1691, Mar. 2003. ISSN 0743-7463. URL `http://dx.doi.org/10.1021/la0263920`.

[111] R. P. Richter, R. BâĹŽÂľrat, and A. R. Brisson. Formation of solid-supported lipid bilayers:âĂŽÃĎÃć an integrated view. *Langmuir*, 22(8):3497–3505, Apr. 2006. ISSN 0743-7463. URL `http://dx.doi.org/10.1021/la052687c`.

[112] S. Riistama, G. Hummer, A. Puustinen, R. B. Dyer, W. H. Woodruff, and M. WikstrâĹŽâĹĆm. Bound water in the proton translocation mechanism of the haem-copper oxidases, Sept. 1997. ISSN 0014-5793. URL `http://linkinghub.elsevier.com/retrieve/pii/S001457939701003X`.

[113] J. W. F. Robertson, M. G. Friedrich, A. Kibrom, W. Knoll, R. L. C. Naumann, and D. Walz. Modeling ion transport in tethered bilayer lipid membranes. 1. passive ion permeation. *The Journal of Physical Chemistry B*, 112(34):10475–10482, Aug. 2008. ISSN 1520-6106. URL `http://dx.doi.org/10.1021/jp800162d`.

[114] R. F. Roskamp, I. K. Vockenroth, N. Eisenmenger, J. Braunagel, and I. Koper. Functional tethered bilayer lipid membranes on aluminum oxide. *ChemPhysChem*, 9(13):1920–1924, Sept. 2008.

[115] E. Sackmann and M. Tanaka. Supported membranes on soft polymer cushions: fabrication, characterization and applications. *Trends in Biotechnology*, 18(2):58–64, Feb. 2000. ISSN 0167-7799. URL `http://www.sciencedirect.com/science/article/B6TCW-3YGT770-8/2/4326220634da704`

[116] S. M. Schiller, R. Naumann, K. Lovejoy, H. Kunz, and W. Knoll. Archaea analogue thiolipids for tethered bilayer lipid membranes on ultrasmooth gold surfaces. *Angewandte Chemie-international Edition*, 42(2):208–+, 2003.

[117] E. K. Schmidt, T. Liebermann, M. Kreiter, A. Jonczyk, R. Naumann, A. Offenhausser, E. Neumann, A. Kukol, A. Maelicke, and W. Knoll. Incorporation of the acetylcholine receptor dimer from torpedo californica in a peptide supported lipid membrane investigated by surface plasmon and fluorescence spectroscopy. *Biosensors & Bioelectronics*, 13(6):585–591, 1998.

[118] Y. Shai. Mechanism of the binding, insertion and destabilization of phospholipid bilayer membranes by alpha-helical antimicrobial and cell non-selective membrane-lytic peptides. *Biochimica Et Biophysica Acta-biomembranes*, 1462 (1-2):55–70, 1999.

[119] K. Shimokata, Y. Katayama, H. Murayama, M. Suematsu, T. Tsukihara, K. Muramoto, H. Aoyama, S. Yoshikawa, and H. Shimada. The proton pumping pathway of bovine heart cytochrome c oxidase. *Proceedings of the National Academy of Sciences*, 104(10):4200–4205, 2007. doi: 10.1073/pnas.0611627104. URL `http://www.pnas.org/content/104/10/4200.abstract`.

[120] J. SIMON, M. KUHNER, H. RINGSDORF, and E. SACKMANN. Polymer-induced shape changes and capping in giant liposomes. *Chem. Phys. Lipids*, 76 (2):241–258, June 1995.

[121] E. K. Sinner and W. Knoll. Functional tethered membranes. *Curr. Opin. Chem. Biol.*, 5(6):705–711, Dec. 2001.

[122] R. E. Smith and S. N. Houde-Walter. Leaky guiding in nontransparent waveguides. *J. Opt. Soc. Am. A*, 12(4):715–724, Apr. 1995. URL `http://josaa.osa.org/abstract.cfm?URI=josaa-12-4-715`.

[123] F. M. Smits. Measurements of sheet resistivity with the four-point probe. *BST J*, 37:711, 1958.

[124] M. SOLIOZ, I. PUTTNER, E. CARAFOLI, and B. LUDWIG. The cytochrome-c oxidase of paracoccus-denitrificans, pumps protons in a reconstituted system. *Experientia*, 38(6):732–732, 1982.

[125] J. Standfuss, A. C. Terwisscha van Scheltinga, M. Lamborghini, and W. Kuhlbrandt. Mechanisms of photoprotection and nonphotochem-

ical quenching in pea light-harvesting complex at 2.5 [angst] resolution. *EMBO J*, 24(5):919–928, Mar. 2005. ISSN 0261-4189. URL `http://dx.doi.org/10.1038/sj.emboj.7600585`.

[126] T. Stora, J. H. Lakey, and H. Vogel. Ion-channel gating in transmembrane receptor proteins: Functional activity in tethered lipid membranes. *Angewandte Chemie-international Edition*, 38(3):389–392, 1999.

[127] M. Tanaka and E. Sackmann. Polymer-supported membranes as models of the cell surface. *Nature*, 437(7059):656–663, Sept. 2005.

[128] S. Terrettaz, M. Mayer, and H. Vogel. Highly electrically insulating tethered lipid bilayers for probing the function of ion channel proteins. *Langmuir*, 19(14): 5567–5569, July 2003.

[129] P. K. TIEN. Integrated-optics and new wave phenomena in optical-waveguides. *Reviews of Modern Physics*, 49(2):361–420, 1977.

[130] R. Toomey, D. Freidank, and J. Ruhe. Swelling behavior of thin, surface-attached polymer networks. *Macromolecules*, 37(3):882–887, 2004.

[131] T. Y. TSONG. Electroporation of cell-membranes. *Biophysical Journal*, 60(2): 297–306, 1991.

[132] T. Tsukihara, K. Shimokata, Y. Katayama, H. Shimada, K. Muramoto, H. Aoyama, M. Mochizuki, K. Shinzawa-Itoh, E. Yamashita, M. Yao, Y. Ishimura, and S. Yoshikawa. The low-spin heme of cytochrome c oxidase as the driving element of the proton-pumping process. *Proceedings of the National Academy of Sciences of the United States of America*, 100(26):15304–15309, 2003. doi: 10.1073/pnas.2635097100. URL `http://www.pnas.org/content/100/26/15304.abstract`.

[133] M. I. Verkhovsky, A. Jasaitis, M. L. Verkhovskaya, J. E. Morgan, and M. Wikstrom. Proton translocation by cytochrome c oxidase. *Nature*, 400(6743):480–483, July 1999. ISSN 0028-0836. URL `http://dx.doi.org/10.1038/22813`.

[134] I. K. Vockenroth, P. P. Atanasova, A. T. A. Jenkins, and I. Koper. Incorporation of alpha-hemolysin in different tethered bilayer lipid membrane architectures. *Langmuir*, 24(2):496–502, 2008.

[135] D. Walz, J. TeissiÃĺ, and E. Milazzo, G. *Bioelectrochemistry: Principles and Practice Vol. 6*. BirkhÃďuser, 2004.

[136] J. C. Weaver and Y. A. Chizmadzhev. Theory of electroporation: A review. *Bioelectrochemistry and Bioenergetics*, 41(2):135–160, 1996.

[137] M. Wentworth, A. V. Ruban, and P. Horton. The functional significance of the monomeric and trimeric states of the photosystem ii light harvesting complexesâĂŽÃĎâĂă. *Biochemistry*, 43(2):501–509, Jan. 2004. ISSN 0006-2960. URL `http://dx.doi.org/10.1021/bi034975i`.

[138] G. Wiegand, N. Arribas-Layton, H. Hillebrandt, E. Sackmann, and P. Wagner. Electrical properties of supported lipid bilayer membranes. *J. Phys. Chem. B*, 106(16):4245–4254, Apr. 2002.

[139] M. WIKSTROM. Identification of the electron transfers in cytochrome-oxidase that are coupled to proton-pumping. *Nature*, 338(6218):776–778, 1989.

[140] M. WikstrËĘm, M. I. Verkhovsky, and G. Hummer. Water-gated mechanism of proton translocation by cytochrome c oxidase. *Biochimica et Biophysica Acta (BBA) - Bioenergetics*, 1604(2):61–65, June 2003. ISSN 0005-2728. URL `http://www.sciencedirect.com/science/article/B6T1S-4899PXW-1/2/0a95fbfbe0f766c`

[141] W. H. WOODRUFF, O. EINARSDOTTIR, R. B. DYER, K. A. BAGLEY, G. PALMER, S. J. ATHERTON, R. A. GOLDBECK, T. D. DAWES, and D. S. KLIGER. Nature and functional implications of the cytochrome-a3 transients after photodissociation of co-cytochrome oxidase. *Proceedings of the National Academy of Sciences of the United States of America*, 88(6):2588–2592, 1991.

[142] C. Xu and L. M. Loew. The effect of asymmetric surface potentials on the intramembrane electric field measured with voltage-sensitive dyes. *Biophysical Journal*, 84(4):2768–2780, Apr. 2003.

[143] X. Zheng, D. M. Medvedev, J. Swanson, and A. A. Stuchebrukhov. Computer simulation of water in cytochrome c oxidase. *Biochimica et Biophysica Acta (BBA) - Bioenergetics*, 1557:99–107, Mar. 2003. ISSN 0005-2728. URL `http://www.sciencedirect.com/science/article/B6T1S-47SV3TD-1/2/df4b9494e073442`

[144] G. Zucchelli, F. M. Garlaschi, and R. C. Jennings. Thermal broadening analysis of the light harvesting complex ii absorption spectrum. *Biochemistry*, 35(50): 16247–16254, Dec. 1996.